Aspects and probes of strongly correlated quantum phases in two dimensions

Clemens Kuhlenkamp

Technische Universität München
TUM School of Natural Sciences

Aspects and probes of strongly correlated quantum phases in two dimensions

Clemens Kuhlenkamp

Vollständiger Abdruck der von der TUM School of Natural Sciences der Technischen

Universität München zur Erlangung eines

Doktors der Naturwissenschaften (Dr. rer. nat.)

genehmigten Dissertation.

Vorsitz:

Prof. Dr. Christian Pfleiderer

Prüfende der Dissertation:

1. Prof. Dr. Michael Knap
2. Prof. Dr. Johannes Knolle
3. Prof. Dr. Ataç İmamoğlu

Die Dissertation wurde am 26.01.2024 bei der Technischen Universität München eingereicht

und durch die TUM School of Natural Sciences am 19.02.2024 angenommen.

Aspects and probes of strongly correlated quantum phases in two dimensions

Abstract

In this thesis, we study new probes, platforms and phases of two-dimensional quantum many-body systems. We demonstrate how the spatial structure of electronic wavefunctions can be probed by optically induced quantum impurities. We use this method to observe correlated Mott-Wigner states and the two dimensional Wigner crystallization transition. We then demonstrate how interactions between quasi-particles can be tuned via solid-state Feshbach resonances, which establishes connections between two dimensional materials and the physics of ultra-cold atomic gases. Last, we study spin-liquid phases in the Fermi-Hubbard model on a triangular lattice, which emerge robustly in the presence of large external fluxes. Possible critical theories describing the phase transitions of the spin liquid and experimental platforms are also proposed.

Aspects and probes of strongly correlated quantum phases in two dimensions

Kurzfassung

In dieser Arbeit untersuchen wir neue Sonden, Plattformen und Phasen zweidimensionaler quantenmechanischer Vielteilchensysteme. Wir zeigen, wie die räumliche Struktur von elektronischen Wellenfunktionen durch optisch induzierte Quantenstörstellen untersucht werden kann. Wir verwenden diese Methode, um korrelierte Mott-Wigner-Zustände und den Übergang zu einem zweidimensionalen Wigner-Kristall zu beobachten. Anschließend zeigen wir, wie Wechselwirkungen zwischen Quasiteilchen über Festkörper-Feshbach-Resonanzen gesteuert werden können, was Verbindungen zwischen zweidimensionalen Materialien und der Physik ultrakalter atomarer Gase etabliert. Abschließend untersuchen wir, wie robuste Spin-Flüssigkeiten im Fermi-Hubbard-Modell auf einem dreiecks Gitter in Anwesenheit großer externer magnetischer Flüsse entstehen. Mögliche kritische Theorien zur Beschreibung der Phasenübergänge der Spin-Flüssigkeit sowie experimentelle Plattformen werden ebenfalls vorgeschlagen.

Contents

For my parents.

Acknowledgments

I am incredibly grateful to have met so many nice and talented people over the last couple of years, who contributed to my PhD in numerous ways. I want to thank all of you for your support.

First and foremost, I would like to thank my two supervisors Michael Knap and Atac Imamoglu for taking me on as a PhD student, all the fun physics projects, and their continuous support throughout space, time and a global pandemic! I really appreciate your advice, that you always took time for me, and that you agreed to our slightly unconventional supervisory constellation.

I have had the pleasure to have known Michael for a long time now. Thank you for five fun years of working together! Thank you also for sticking your head out for me, welcoming me in your group, always responding to my messages in record time, your patience, helping me with my writing, and teaching me a lot of physics. Your efforts did not go unnoticed.

I want to thank Atac for being open to all sorts of ideas, starting from the moment I first arrived in Zurich. Numerous great discussions followed, during which you taught me to take physical intuition seriously. I am still amazed, how many seemingly obscure theoretical calculations have a simple, elegant and intuitive picture. Thank you also for providing us with free coffee in Zurich, it was much appreciated!

I am also grateful to Ashvin Vishwanath for hosting me in Harvard over the winter. I also want to thank the condensed matter theory group for being so welcoming and many enlightening discussions with Rahul, Patrick, Junkai, Ruben and Francisco.

Publications

The content of this thesis is based on works, which are published in peer-reviewed journals or are available on the arXiv.

Works contained in this thesis:

1. "Optical signatures of charge order in a Mott-Wigner state", Yuya Shimazaki*, **Clemens Kuhlenkamp***, Ido Schwartz*, Tomasz Smolenski*, Kenji Watanabe, Takashi Taniguchi, Martin Kroner, Richard Schmidt, Michael Knap and Atac Imamoglu, Physical Review X 11, 021027 (2021)

2. "Observation of Wigner crystal of electrons in a monolayer semiconductor", Tomasz Smoleński, Pavel E. Dolgirev, **Clemens Kuhlenkamp**, Alexander Popert, Yuya Shimazaki, Patrick Back, Martin Kroner, K. Watanabe, T. Taniguchi, I. Esterlis, Eugene Demler and Atac Imamoğlu, Nature 595, 53-57 (2021)

3. "Tunable Feshbach resonances and their spectral signatures in bilayer semiconductors", **Clemens Kuhlenkamp**, Michael Knap, Marcel Wagner, Richard Schmidt and Atac Imamoglu, Physical Review Letters, 129, 037041, (2022)

4. "Observation of electrically tunable Feshbach resonances in twisted bilayer semiconductors", Ido Schwartz, Yuya Shimazaki, **Clemens Kuhlenkamp**, Kenji Watanabe, Takashi Taniguchi, Martin Kroner and Ataç Imamoğlu, Science 374, 6565, pp. 336-340, (2021)

5. "Optical signatures of periodic magnetization: the moiré Zeeman effect", Alex Gómez Salvador, **Clemens Kuhlenkamp**, Livio Ciorciaro, Michael Knap and Ataç İmamoğlu, Physical Review Letters 128, 237401, (2022)

6. "Tunable topological order of pseudo spins in semiconductor heterostructures", **Clemens Kuhlenkamp**, Wilhelm Kadow, Atac Imamoglu, Michael Knap, arXiv:2209.05506 (2022)

7. Caterina Zerba, **Clemens Kuhlenkamp**, Atac Imamoglu and Michael Knap: "Realizing Topological Superconductivity in Tunable Bose-Fermi Mixtures with Transition Metal Dichalcogenide Heterostructures", arXiv:2310.10720, (2023)

Works not contained in this thesis:

1. "Periodically Driven Sachdev-Ye-Kitaev Models", **Clemens Kuhlenkamp** and Michael Knap, Physical Review Letters, 124, 106401 (2020)

2. "Universal transport in periodically driven systems without long-lived quasiparticles", Iliya Esin, **Clemens Kuhlenkamp**, Gil Refael, Erez Berg, Mark S. Rudner and Netanel H. Lindner, arXiv:2203.01313

3. "Thermal and dissipative effects on the heating transition in a driven critical system", Kenny Choo, Bastien Lapierre, **Clemens Kuhlenkamp**, Apoorv Tiwari, Titus Neupert and Ramasubramanian Chitra, SciPost Phys. 13, 104 (2022)

4. "Feshbach resonances of composite charge carrier states in atomically thin semiconductor heterostructures", Marcel Wagner, Rafał Ołdziejewski, Félix Rose, Verena Köder, **Clemens Kuhlenkamp**, Ataç İmamoğlu, Richard Schmidt, arXiv:2203.01313

1

Introduction

Collective effects emerge in nature when large groups of objects starts to interact with each other. Everyday examples range from swarm formation in birds to traffic jams. Why does such behaviour emerge, and what are the rules which govern it? This is the main question that drives condensed matter physics.

Indeed, almost all many-body systems form some type of collective order at low enough temperatures: atoms tend to form crystalline structures, certain materials spontaneously give rise to magnetic fields and some metals turn superconducting. Phases of matter which develop such "classical order" are analyzed in terms of Landau theory [1]. At its core one analyzes the interplay between the spontaneous breakdown of symmetries, long-wavelength fluctuations; and thermodynamics. This theory has been immensely successful in classifying phases of matter and their dynamics [2] and has taught us many universal properties of their phase transitions [3]. However, this exploration is not of purely academic interest. Much of modern day technology, such as gas liquefaction via the Linde cycle, magnetic memory and

liquid crystal displays, rests on our understanding of broken symmetries and phase transitions.

Ever since the discovery of the fractional quantum Hall effect in 1982 [4], we know that many-body systems can exhibit order beyond the Landau paradigm. Interactions may stabilize an exotic *intrinsic topological order*, which is not directly tied to any obvious global symmetry. Instead, topologically ordered phases are best thought of as deconfined gauge theories, which reveals deep connections to high energy physics [5]. At least when their fundamental constituents are bosonic, these phases are referred to as *spin liquids*. Assuming that all excitations cost a finite amount of energy, spin liquids differ from conventional phases in several ways. They host fractional excitations, and feature a ground state degeneracy, which depends on the genus of the surface they are defined on [6]. This can be connected to the fact that topologically ordered states are hard to deform into trivial product states, i.e. their ground state wavefunctions posess long-range quantum entanglement [7, 8, 9]. If one could realize and manipulate spin-liquid phases in the lab, the presence of anyons in two dimensions would enable topological quantum computation [10]. While spin liquids can be constructed on paper in solvable fixed-point models, this last part turns out to be a formidable experimental challenge [11, 12]. Classical ordering at low temperatures is hard to suppress, while parameters are hard to control. This adds to the fragility of these phases. Furthermore, fractionalization of excitations generically lead to broad spectral features, which are hard to uniquely tie to the existence of a spin liquid. Therefore, the unequivocal observation of a spin liquid phase and its transitions in a solid remains a critical open problem.

Similar issues appear when studying classical order in low dimensions. The presence of strong (quantum) fluctuations and interactions makes it hard to theoretically model correlated regimes. As a result, the phase diagram of high-Tc superconductors and the two dimensional electron gas are still debated [13, 14, 15]. Experimental progress is hindered as solids often lack sufficient tunability as well as access to direct probing schemes, which obscures the identification of order [13].

History has taught us, that much of our theoretical understanding advances hand in hand with experimental discoveries and capabilities. Indeed, we live in exciting times as novel platforms such as neutral atoms in optical lattices and tweezers [16, 17], quantum computing platforms [18, 19], and designer materials [20] have made remarkable advances over the last

4

couple of years. On the one hand, controllable platforms to study strongly correlated insulators were discovered in solids [21, 22], while first signatures of a spin-liquid phase were probed in Rydberg atom arrays [23] and superconducting qubits [24]. This illustrates the possibility to utilize these new platforms, along with the opportunities and probes they provide, to revisit long-standing problems in condensed-matter physics. Besides closing gaps in our understanding, these platforms will enable the realization of entirely new phases of matter.

The goal of this thesis is to address some of the open problems outlined above. We focus on engineering, understanding and probing exotic phases of matter with both symmetry-breaking and topological order. The structure of the following chapters is summarized below:

- In Chapter 2, we review the strongly correlated electron models relevant to this thesis. We also provide a brief introduction to the physics of two-dimensional materials, which have recently emerged as rich, tunable experimental platforms to study the phases of such models as well as their transitions.

- In Chapter 3, we introduce a new class of optical probes which are directly sensitive to spatial correlations of electrons. We provide a simple theoretical model, which demonstrates that crystallization transitions, as well as their precursors can be reliably detected in two dimensional semiconductors. We conclude this chapter by applying our theory to recent experimental data, which provides a first observation of Wigner crystallization in a two dimensional material and the detection of a magneto-roton mode in an integer quantum Hall state.

- In Chapter 4 we propose how interactions between electronic and excitonic quasi-particles can be tuned via an analogue of an atomic Feshbach resonance, simply by changing external electric fields. This establishes connections between two seemingly unrelated areas of physics and provides the opportunity to study the rich phase diagram of Bose Fermi mixtures in solid state systems. We then present a recent experimental observation of such a resonance. Using the Feshbach mechanism, the strong coupling regime between a dilute concentration of optical excitations and a Fermi sea could be reached.

- Chapter 5 starts with a brief introduction to spin liquids. We then show that applying large magnetic fields can stabilize a remarkably robust chiral (pseudo-) spin liquid in the triangular lattice Hubbard model. We propose moiré systems as natural experimental platforms to realize these systems and discuss suitable signatures. To finalize this chapter we comment on potential critical theories which set the phase boundaries of the chiral spin liquid.

- In Appendix A we review the contact approximation for two dimensional scattering and provide a theory for more general Feshbach resonances. We also discuss a non-equilibrium field theory approach to the impurity problem in the presence of a Feshbach resonance.

- Appendix B discusses a derivation of the effective Hubbard model and includes a detailed stability analysis of the spin-liquid phases in our model.

- Chapter 6 concludes this thesis by summarizing our results and highlighting future directions.

2

Preliminaries

We introduce important concepts for models and experimental platforms relevant to this thesis.

2.1 Modelling many-body systems

Even if one was handed a many-body wavefunction of an exotic state, the difficult task of identifying the basic principles which govern its stability would remain. This, however, is crucial for both our understanding of condensed matter physics and our ability to prepare exotic quantum phases in experiments. The goal of a condensed matter theorist is therefore to develop and understand simple models, which can serve as a bridge between theoretical ideas and experimental observations. The hope is that these models capture universal behaviour which remains applicable to more complicated systems found in the real world. An

additonal advantage of such systems is that they are often computationally more tractable, which is important as the cost to simulate a quantum system generally scales exponentially with system size. In certain cases, they allow for the construction of exact or approximate solutions, which helps to gain a deeper understanding of a systems' behaviour.

For the purpose of this thesis, there are two major models which guide the physical thinking in the field strongly correlated electron systems: the Jellium model and the Hubbard model, which we introduce below. We concentrate on two-dimensional variants of these models, where quantum fluctuations and interactions are particularly strong. In this context, exotic phase transitions and quasi-particles emerge. We conclude this chapter by highlighting that two-dimensional materials provide natural experimental platforms, well described by these models.

2.2 JELLIUM MODEL

The simplest possible starting point for studying electronic quantum matter, are spinful electrons moving on a two dimensional plane. In a realistic system, electromagnetism tells us that charges repel, which means that we should really study electrons in the presence of Coulomb repulsion $V(\mathbf{x}) = e^2/4\pi\varepsilon\varepsilon_0|\mathbf{x}|$. A good starting point is then provided by the following Hamiltonian

$$\hat{H} = \sum_{\sigma\in\{\uparrow,\downarrow\}} \int d^2\mathbf{x}\, \psi_\sigma^\dagger(\mathbf{x})(\frac{\nabla^2}{2m^*}-\mu)\psi_\sigma(\mathbf{x}) + \int d^2\mathbf{x} \int d^2\mathbf{y}\,(\hat{n}(\mathbf{x})-n_0)V(\mathbf{x}-\mathbf{y})(\hat{n}(\mathbf{y})-n_0),$$

$$(2.1)$$

where $\psi_\sigma^\dagger(\mathbf{x})$ creates an electron in spin state σ at position $\mathbf{x}$, $\hat{n}(\mathbf{x})$ is electronic charge density, μ is the chemical potential, and we have subtraced the background density n_0 we have implicitly added a neutralizing charge background. The Jellium model described by Eq. 2.1 has a long history and some of its properties are already well understood [25, 13].

Fermi liquid— If the system does not undergo a phase transition, i.e. does not form for example a magnet or a superconductor, metallic states prevail. In this case, Fermi liquid theory states that quasi-particle excitations close to the Fermi surface are still connected to free electronic state even in the presence of repulsive interactions. Specifically this means

that the inverse lifetime of electronic excitations scale as $\tau^{-1} \sim \text{Max}\left(T^2/E_F^2, \; \hbar^2\omega^2/E_F^2\right)$, where T is temperature and $\hbar\omega$ is the energy of the excitation measured from the Fermi surface. In some sense this implies that a metal can still be thought of as a free Fermi gas, albeit with renormalized parameters [25]. This result is remarkable, because metals are gapless and thereby particularly susceptible to perturbations.

Wigner crystal— In the limit where interactions dominate over the kinetic energy, one may imagine that the electrons will form a minimal packing configuration given by a triangular lattice. This indeed happens for Eq. 2.1 in the strongly interacting limit when electrons spontaneously break translational symmetry to form a Wigner, named after Eugene Wigner, who first predicted the phase in 1934 [26]. The strength of interactions is quantified by the dimensionless r_s parameter which relates kinetic and interaction energies as follows:

$$r_s = \frac{E_{\text{int.}}}{E_{\text{kin.}}} = m^*e^2/\left(4\pi\varepsilon_0\varepsilon\hbar^2\sqrt{\pi n_e}\right) \sim 1/\sqrt{n_e} \tag{2.2}$$

Interactions are strongest in the dilute limit. While both Coulomb-interactions and kinetic energy grow with decreasing particle separation, the interaction energy term dominates at low densities. Quantum Monte Carlo calculations suggest that a Wigner crystal is formed for $r_s \gtrsim 30$ [27].

Transition and intermediate phases— The transition is best analyzed by constructing the free energy of the system, F, in a phenomenological Landau Ginzburg approach. In general, the free energy is a function of only a few variables, including temperature, pressure and a set of *order parameters* η, which are non-zero only in the spontaneously symmetry breaking phase: $F = F(T, p, \eta)$. In the crystalline phase the density is modulated in a triangular lattice, described by reciprocal lattice vectors

$$\mathbf{G}_1 = \frac{1}{2\pi a}(1, 1/\sqrt{3})^T \quad \text{and} \quad \mathbf{G}_2 = \frac{1}{2\pi a}(-1, 1/\sqrt{3})^T, \tag{2.3}$$

with a the lattice constant. We parameterize the density modulation via

$$\langle n(\mathbf{x})\rangle - n_0 = \sum_{\mathbf{G}\neq 0}\langle\tilde{n}(\mathbf{G})\rangle e^{i\mathbf{G}\cdot\mathbf{x}}, \tag{2.4}$$

where n_0 is the average density and $\eta_{\mathbf{G}} = \langle\tilde{n}(\mathbf{G})\rangle \neq 0$ signal broken translational symmetry.

Since under translations $\mathbf{x} \to \mathbf{x} + \mathbf{a}$ we find

$$\eta_{\mathbf{G}} \to e^{i\mathbf{G}\cdot\mathbf{a}}\eta_{\mathbf{G}}, \tag{2.5}$$

any non-zero fourier harmonic indicates breaking of translations. Close to the transition it is reasonable to assume that crystal formation is dominated by the 6 lowest harmonics of the triangular lattice $\{\mathbf{G}_i\}_{i=1,\ldots 6}$. Such triangular structures are special, as three reciprocal lattice vectors of equal length can sum to zero:

$$\mathbf{G}_1 + \mathbf{G}_2 + \mathbf{G}_3 = 0, \tag{2.6}$$

see Fig. 2.1 for an illustration. This mathematical fact is related to the fundamental obser-
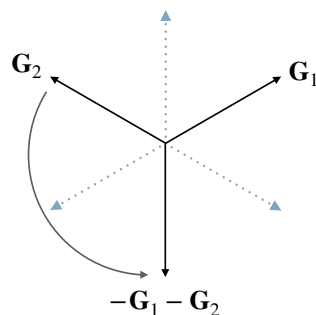
Figure 2.1: Reciprocal lattice vectors of the triangular lattice. Reciprocal lattice vectors of the Wigner crystal related by a $120°$ rotation (grey arrow) sum to zero in groups of three (black and blue arrows). This renders the crystallization transition first order.

vation, namely that crystallization transitions are first order [1, 28, 29]. This can be understood by the phenomenological construction of $F(T, p, \eta)$ based on analyticity and symmetry. Assuming that one can expand in the order parameters close to the transition, this motivates the following form for the free energy

$$F/V = \sum_{i=1}^{6} r\,|\eta_{\mathbf{G}_i}|^2 - w \sum_{ijk=1}^{6} \eta_{\mathbf{G}_i}\eta_{\mathbf{G}_j}\eta_{\mathbf{G}_k}\,\delta_{\mathbf{G}_i+\mathbf{G}_j+\mathbf{G}_k,0}$$
$$+u \sum_{ijkl=1}^{6} \eta_{\mathbf{G}_i}\eta_{\mathbf{G}_j}\eta_{\mathbf{G}_k}\eta_{\mathbf{G}_l}\,\delta_{\mathbf{G}_i+\mathbf{G}_j+\mathbf{G}_k+\mathbf{G}_l,0}, \tag{2.7}$$

where $\eta_{\mathbf{G}} = \eta^*_{-\mathbf{G}}$, r, w and u depend on temperature, pressure, density, etc.. The cubic term is only present due to the triangular lattice structure Eq. 2.6, while the transition is driven by a sign change of r. By minimizing Eq. 2.7 one finds that unless w is fine-tuned to zero, the cubic terms turn the transition (weakly) first order [28]. First order transitions are ac-
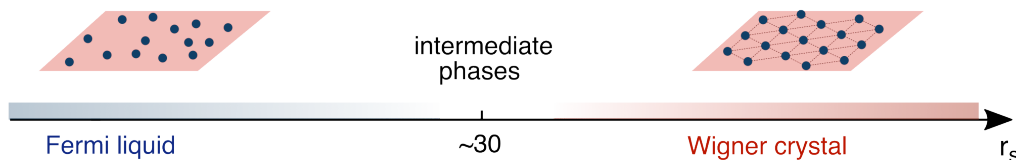
Figure 2.2: Schematic of the phase diagram of the 2d electron gas. For low r_s (high densities), the system forms a Fermi liquid, while for high r_s (low densities) the system forms a triangular crystal. Since direct first order transitions are forbidden in the electronic system due to long-range interactions, intermediate phases must exist.

companied by phase separation, however, in the case of the Jellium model this is forbidden by long-range repulsion [30]. This prohibits a direct transition between the Fermi liquid and the Wigner crystal phase. Rather the transition must be replaced by potentially several intermediate phases, such as stripes and bubbles [31].

This is where we reach the unexplored regime of the model Eq. 2.1. The nature of the intermediate phases, as well as the spin order in the Wigner crystal phase are still uncertain [32, 13, 33]. These long-standing problems are not just hard to treat theoretically, but also difficult to explore in experiments, partially because it is hard to directly probe spatial correlations in the model [34]. We make progress on the latter problem in Chapter 3, where we introduce novel optical techniques that allow us to probe the crystalline order and its precursors. Furthermore, we demonstrate how to couple bosonic modes to the Fermi-liquid phase in a tunable fashion in Chapter 4. This is interesting as it this allows us to to modify the properties of the Fermi liquid as well as to drive instabilities to ordered phases such as superconductors.

2.3 THE FERMI-HUBBARD MODEL

Restricting fermions to move only on a discrete lattice, is generally a good idea. Given that almost all material systems in condensed-matter physics can be thought of as electrons re-

siding in orbitals of an underlying atomic lattice, this is very close to physical reality. From a theoretical perspective, it allows for a rigorous definition of many-body Hamiltonians since lattice models are mostly free from unphysical divergences. More importantly, however, lattice systems are fundamental to understand correlated insulators and magnets, as they naturally stabilize novel phases of matter. The simplest such lattice model is described by the following Hamiltonian:

$$\hat{H} = -\sum_{ij,\sigma} t_{ij}\, c^\dagger_{i,\sigma} c_{j,\sigma} - \mu \sum_{i,\sigma} n_\sigma(i) + U \sum_i n_\uparrow(i) n_\downarrow(i), \qquad (2.8)$$

where $c^\dagger_{i\sigma}$ creates an electron on site i of the specific lattice we are considering, t_{ij} denotes the tunneling strength between lattice sites i and j, μ is the chemical potential and U is a repulsive interaction which penalizes two electrons sharing a single lattice site. These interactions originate from Coulomb repulsion, but it often suffices to only retain on-site contributions of strength U^*. Eq. 2.8 is the Hubbard model, named after John Hubbard, who introduced it in 1963 [35].

Correlated insulators— For small U/t the system generically behaves similar to the Fermi liquids discussed in the Jellium model. However a correlated *Mott insulator* appears in the limit $U/t \gg 1$ at half filling. In this case hopping is allowed for electrons in opposite spin states, but necessarily generates double-occupancies. These are strongly suppressed by the large energy scale U. Therefore, charges remain frozen and obey an effective *single occupancy constraint*

$$n_\uparrow(i) + n_\downarrow(i) = 1, \qquad (2.9)$$

while the fluctuations of electronic spins are described by anti-ferromagnetic Heisenberg Hamiltonians [36], gives rise to quantum magnetism. The interplay between spin and charge fluctuations enriches Metal-Insulator transitions much beyond to their well-understood bosonic counterparts [3]. In high dimensions Metal-Insulator transitions are often first order, while continuous transitions may exist in two dimensions on special lattice geometries [14, 37]. Interest in the Hubbard model has been growing, every since the discovery of high-Tc superconductivity in 1986 [38], which is believed to be described by a hole doped Fermi-Hubbard model on a square lattice. Soon thereafter, it was realized that innocuous

---

*Longer-range interactions are easily included. We discuss their effects in appendix B.

looking constraints like Eq. 2.9 may play an important role in forming superconducting order [39, 40]. However, despite years of work, the phase diagram of the doped Fermi-Hubbard model on square and triangular lattices, remains debated [15, 37, 41, 42].

Despite this lack of consensus, there are reasons to be hopeful. In an interesting turn of events, the difficulty in analyzing the Fermi-Hubbard model has sparked experimental efforts, aiming to design platforms which closely mimic the Hubbard model [43, 16, 44]. In contrast to the cuprates, some of these platforms are highly tunable, which provides an ideal test bed for theorists [45, 46]. By leveraging the properties of these platforms, we explore the phase diagram of the Hubbard model on a triangular lattice in Chapter 5. We demonstrate that in the presence of strong magnetic fields the single-occupancy constraint rise to a robust spin-liquid phase. This is a concrete example, how a gauge theory, such as electromagnetism, can emerge in a realistic model. We also discuss candidate critical theories, which govern the appearance and disappearance of this spin liquid phase.

Searching for exotic phases of matter in solid-state systems is a difficult task, as properties of solids are generically hard to control experimentally which limits progress in understanding their underlying physics. Furthermore, experimental platforms in which idealized theoretical models can be controllably engineered and tested are rare and were so far limited to small parameter regimes. This leaves exotic states, such as high-Tc superconductivity and spin liquids, as well as their underlying mechanisms, poorly understood. Remarkably a recent surge of experimental advances in the field of two-dimensional materials, atomic quantum gases, and quantum computing platforms has made it possible to systematically explore exotic phases of matter due to the unusually high tunability of these systems [16, 44, 47, 22, 48, 23, 24].

TWO DIMENSIONAL MATERIALS AS EMERGING EXPERIMENTAL PLATFORMS

The experimental realization of atomically thin materials had a large impact on solid state physics as they allow for tunable electron densities and can naturally host strong Coulomb interactions as screening is suppressed compared to bulk three dimensional materials. Furthermore, a large class of systems such as Graphene and *transition metal dichalcogenides* (TMDs) have a particularly simple atomic structure, which makes it possible to theoretically model their electronic properties. For both of these materials, atoms are arranged in a triangular lattice with two atoms per unit cell. In the case of Graphene two p_z orbitals form low-energy bands, which host *Dirac cones* at the K and $K' = -K$ points in the Brillouin zone. These points dominate much of the electronic protperties of Graphene and are protected by time reversal $\mathcal{T}$ and inversion symmetry $\mathcal{I}$ (which exchanges the two sublattices). As such, Graphene has an emergent relativistic symmetry, and a vanishing density of states at the Fermi level, which in combination with the steepness of the Dirac cones suppresses interaction effects. In TMDs, on the other hand, the unit-cell is composed of one metal (M) and two out-of-plane separated chalcogen atoms (X), introducing a staggered potential for electrons on the A and B sublattices, thereby breaking $\mathcal{I}$ symmetry and gapping out the Dirac Cones [49]. The lattice and the Brillouin zone is schematically shown in Fig. 2.3a. The points of lowest energy remain at the K and K'. However, the electronic dispersion is
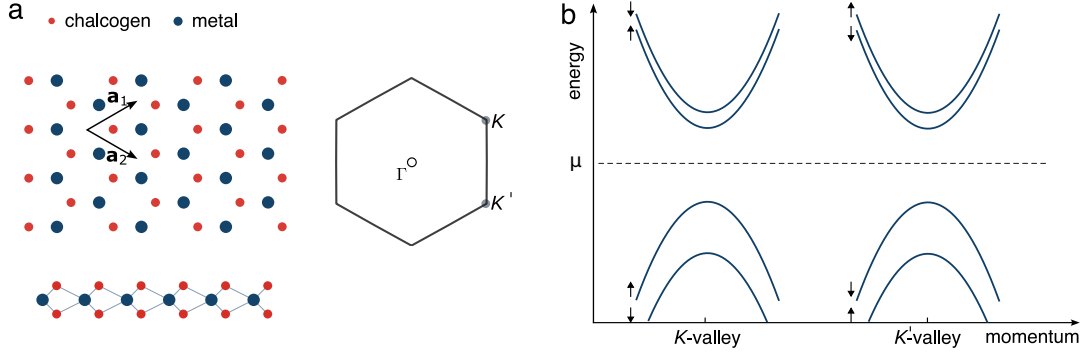
Figure 2.3: Schematic electronic structure of monolayer TMDs. Single layers of group-IVB TMDs have a chemical composition of one metal and two chalcogen atoms (MX_2). **a)** Top-down and side view of the hexagonal atomic lattice, which forms a honeycomb structure with metal atoms sitting at the A-sites (shown in blue) and two chalcogen atoms sitting at the B-sites (shown in red). The corresponding Brillouin zone is shown on the right, which possesses in-equivalent K- and K'-points. The TMDs considered here are direct-band gap semiconductors and the minima (maxima) of their conduction (valence) bands are located at the K (K') valley. **b)** Schematic illustration of the relevant band structure for $MoSe_2$ in the low doping limit. The bands disperse approximately quadratically and electronic spin is locked to the valley by strong spin-orbit coupling close to the K-points, which results in spin-polarized bands indicated in the figure by black arrows. The chemical potential μ can be adjusted and is shown as a dashed grey line.

rendered parabolic with heavy effective electron and hole masses on the order of the bare electron mass $m^* \simeq m_e$. This is captured by an effective $\mathbf{k} \cdot \mathbf{p}$ expansion, and described by the following low-energy Hamiltonian

$$\hat{H}_{\pm K} = at(\pm k_x \sigma^x + k_y \sigma^y) + \frac{\Delta}{2}\sigma^z \mp \lambda \frac{\sigma^z - 1}{2} s^z, \tag{2.10}$$

where a is the lattice constant ($a \simeq 3.3$ for $MoSe_2$ [50]), t is the effective hopping integral and $\Delta \simeq 1.5$eV labels the band direct gap, while λ encodes the leading effects of spin-orbit coupling. The resulting bands are shown in Fig. 2.3b. The large electron mass strongly suppresses kinetic energy and makes Coulomb interactions important even for finite charge-doping. Hence TMDs are ideal test-beds to explore strongly correlated quantum gases of electrons and holes.

In the following we will work mostly in the continuum limit described by Eq. 2.10, which is an excellent approximation since typical energy scales set by temperature T, fermi energies
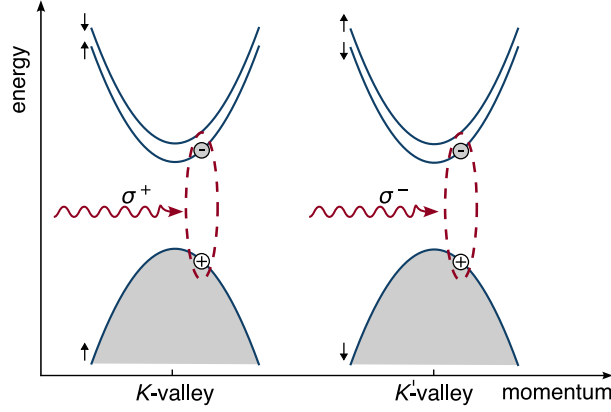
Figure 2.4: Exciton formation in a TMD monolayer. Due to their direct band-gap, it is possible to optically excite electron-hole pairs, which form strongly bound excitons, shown as red dashed lines. Optical selection rules imply that σ^+/σ^- polarized photons generate excitons only in the K/K'-valley. Due to large electron and hole masses $m^*_{e,h}$ and strong Coulomb interactions, their binding energies are on the order of 0.5eV and exceed typical scales in the system. This separation of scales makes it possible to treat them as structureless bosons.

ε_F, etc. are small compared to the band gap Δ.

Excitons as composite bosons

Signatures of strong correlations in TMDs appear already when analyzing the systems optical excitation spectrum. Since the TMDs considered here are direct band-gap semiconductors, it is possible to excite electron-hole pairs optically. Once excited, electron and hole will experience Coulomb interactions and form a bosonic molecule, known as an *exciton*. The excitonic binding energies are close to atomic scales and reach up to $E^0_X \simeq 0.5\text{eV}$. This implies that they are effectively composite bosonic objects with a small Bohr radius of $a_X \simeq 1\text{nm}$. This makes it possible to model them as fundamental bosonic objects with creation operators $x^\dagger(\mathbf{r})$.

Light-matter coupling in semiconductors is constrained by optical selection rules: the quantum numbers of the entire system before and after absorbing a photon, must remain the same. Since σ^+ (σ^-) polarized photons carry intrinsic angular momentum of $\pm\hbar$, they can only be absorbed if they transfer their angular momentum to the material. Eq. 2.10 encodes that promoting an electron from valence to conduction band in the K (K') valley is accom-

panied by an angular momentum change of $+\hbar\,(-\hbar)$. This ensures that $\sigma^+\,(\sigma^-)$ polarized light couples directly to the $K\,(K')$ valley, as shown in Fig. 2.4. More quantitative calculations of the excitation spectrum can be made by minimally coupling the electromagnetic field to Eq. 2.10:

$$\mathbf{k} \to \mathbf{k} + e\mathbf{A}(\mathbf{x}, t), \tag{2.11}$$

where $\mathbf{A}(\mathbf{x}, t)$ is the electromagnetic vector potential. $\mathcal{T}$ symmetry exchanges the K and K' valley and ensures that excitons created in the two valleys have the same energies.

As excitons can be thought of as polarization waves, they directly couple to incident light fields. Conveniently this implies that reflection measurements on TMDs can easily access excitonic correlation functions within linear response, which allows us to probe

$$\mathcal{G}^R(t - t', \mathbf{k} = 0) = -i\Theta(t - t')\langle\left[x_{\mathbf{k}=0}(t), x^\dagger_{\mathbf{k}=0}(t')\right]\rangle. \tag{2.12}$$

This provides us with import information about the system, which contains the spectral function of the exciton

$$A_x(\omega) = -2i\,\mathrm{Im}\{\mathcal{G}^R(\omega, \mathbf{k} = 0)\}. \tag{2.13}$$

Of course, since optically active excitons can be excited, they can decay spontaneously by emitting a photon, with a rate Γ. We treat this process in detail in Chapter 4.

EXCITON-CHARGE INTERACTIONS AND MOLECULES

On a first glance, the presence of Fermi surface in the form of doped charges modifies the properties of the exciton only slightly: as discussed, their binding energies $E_X^0 \gg \varepsilon_F \simeq$ 10meV are larger than typical Fermi energies studied in experiments. Although momenta smaller than the Fermi momentum k_F can no longer efficiently contribute to exciton formation due to the Pauli exclusion principle; the tight binding of the exciton implies that its wave function consists mostly of electron-hole pairs at large momenta $k > k_F$. Thus, we expect only quantitative changes, such as a small reduction in the excitons binding energy. Exciton-electron interactions, on the other hand, can lead to strong and qualitative changes of the excitons properties by correlating with the surrounding electrons, even if the structure of the exciton itself is unmodified. In the following we will discuss exciton-electron
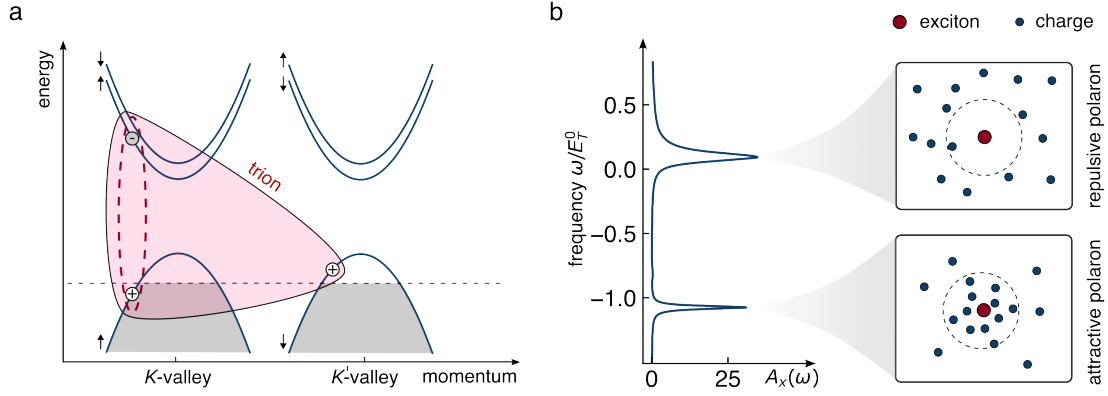
Figure 2.5: Bound state formation in the presence of a Fermi sea and the Fermi polaron. a) Tightly bound excitons can interact with free carries to form charged bound-states, known as *trions*. Due to Pauli-blocking trions primarily form with holes which reside in a valley opposite to that of the exciton. b) The presence of a Fermi surface changes the properties of the exciton. We plot the spectral function of the exciton computed within a T-matrix approximation as a function of frequency for a Fermi energy of $\varepsilon_F/E_T^0 = \frac{1}{6}$ and a radiative broadening of $\Gamma = \frac{1}{30}E_T^0$. The spectrum exhibits collective excitations known as *attractive* and *repulsive polarons*, with spectral weights and energies which depend on the value of the Fermi energy. The attractive polaron can be thought of as a collective molecular excitation, essentially forming an attractive dressing cloud and thereby lowering its energy compared to the bare molecule. The repulsive polaron, is connected to the bare exciton in the $\varepsilon_F/E_T^0 \to 0$ limit, but acquires a short lifetime and is pushed to higher energies by repulsive interactions with the Fermi surface.

interactions and show that an exciton coupled to a Fermi-sea is best thought of as a mobile quantum impurity, which forms a quasi-particle commonly referred as a *Fermi polaron*.

Although excitons are neutral bound-states they are sensitive to nearby charges. On the one-hand there are long-range interactions as the electric field of an elecron can polarize the exciton, thereby inducing a dipole moment $\mathbf{d} = \alpha\mathbf{E}$, where α is the polarizability of the exciton. The energy of the induced dipole scales with the usual electrostatic relation $\mathbf{d} \cdot \mathbf{E}$. Since the electric field of the charge decays as $\mathbf{E} \sim \mathbf{e}_r/r^2$, we find that the interaction between an exciton and a charge separated by a large distance $|\mathbf{r}|$ follows a power-law:

$$V_{X-e}(\mathbf{r}) \sim \frac{1}{r^4}, \qquad (2.14)$$

and is attractive. In addition there are contributions when electron and exciton are nearby. Experiments; as well as microscopic three-body calculations, found that these interactions

can be attractive and lead to the formation of charged "molecular" bound states, known as *trions*, which reach binding energies $E_T^0 \simeq 30\text{meV}$. Interactions between the exciton and charges are repulsive, if the excess charge shares the same quantum numbers as the constituents of the exciton. This effect can be attributed to Pauli blocking, which increases the energy of the configuration such that the state becomes unbound. Consequently, positively charged trions can be thought to consist of an exciton bound to a hole, which resides in the valley opposite to that of the exciton, as depicted in Fig. 2.5a); while acting repulsively in the opposite configuration. In the limit of low carrier-density, exciton-electron interactions can be safely described by short-range pseudo-potentials, without changing the relevant low-energy scattering physics [51], since typical momenta are too small to efficiently resolve the microscopic details of interactions as dictated by the uncertainty principle. For the rest of this thesis, we therefore model electron-exciton interactions by a regularized contact interaction:

$$\hat{V}_{X-e} = U_\Lambda \sum_{\mathbf{k},\mathbf{k}',\mathbf{q}}^{\Lambda} x_{\mathbf{k}}^\dagger x_{\mathbf{k}-\mathbf{q}} \, c_{\mathbf{k}'}^\dagger c_{\mathbf{k}'+\mathbf{q}}, \tag{2.15}$$

where strength U_Λ and momentum cut-off Λ are chosen to reproduce the scattering physics and binding energies of the microscopic potential. This procedure is commonly used in describing the physics of ultra-cold atomic quantum gases [43], which already hints at an analogy between two-dimensional materials and atomic physics. In Chapter 4 we will discuss and extend this connections and utilize it to show how exciton-electron interactions can be tuned in multi-layer systems by changing external electric fields.

Polaron formation

A single quantum particle in contact with a gas of (Bosons) Fermions is known as the *(Bose) Fermi polaron problem*. The Polaron problem was first discussed by Landau and Pekar to provide a theory of electron conduction in ionic crystals. They demonstrated that the electrons mass increases significantly by coupling to vibrations of the underlying lattice. This turns out to be a generic effect of Polaron formation: *the properties of the bare impurity are often strongly altered as it interacts with the bath.* Remarkably, static impurities can modify the properties of the entire system, in what is known as Andersons orthogonality catastrophe [52], which is crucial in understanding X-ray absorption experiments [53]. Fur-

thermore, polarons can be thought of as strongly imbalanced Bose-Fermi mixtures, which makes them well-defined starting points to understand the rich phase diagrams which appears at finite impurity density. Nevertheless, many open questions remain and strongly coupled Polarons are being actively explored in atomic gases and solids [54, 55, 56, 57, 58, 59].

Naively one may expect that an exciton immersed in an electron gas will form a molecule to lower its energy, thereby changing its statistics. This, however, does not happen. Instead the many-body system contains bosonic eigenstates $|\mathrm{Pol}\rangle$, i.e. attractive polarons, which have a lower energy than the molecular state and retain a finite overlap with the bare exciton

$$Z_\alpha = \big| \langle \mathrm{Pol}| \big(x_\alpha^\dagger |\Omega\rangle \big) \big| \neq 0. \tag{2.16}$$

In Eq. 2.16 we have grouped all quantum numbers of the exciton, such as $\mathbf{k}$, valley polarization K/K', etc., into the label α. While a finite value of Z_α implies that the exciton remains a well-defined quasi particle, their properties will be strongly renormalized by forming a dressing cloud. Theoretically attractive polarons can be understood with a simple variational ansatz wavefunction:

$$|\mathrm{Pol}, \alpha\rangle = Z_\alpha\, x_\alpha^\dagger |\mathrm{FS}\rangle + \sum_{\beta, \mathbf{k}, \mathbf{q}} C_\alpha(\beta, \mathbf{k}, \mathbf{q})\, x_\beta^\dagger e_\mathbf{k}^\dagger e_\mathbf{q} |\mathrm{FS}\rangle, \tag{2.17}$$

where $|\mathrm{FS}\rangle$ is the Fermi sea and $C_\alpha(\beta, \mathbf{k}, \mathbf{q})$ are coefficients parameterizing the dressing. In writing down Eq. 2.17 we have assumed that the exciton excites at most one more electron-hole pair from the Fermi sea. This Ansatz turns out to be equivalent to the field theoretic approaches discussed in detail in Chapter 4, if interactions are short-range [60]. The resulting excitonic spectral function and an illustration of the dressing cloud is shown schematically in Fig. 2.5b), which also demonstrates that the attractive polaron has lower energy than the bare molecule. This fact is best visualized by viewing the attractive polaron as a superposition of molecular states involving many electrons. In the limit $E_F \gg E_T^0$, the attractive polaron contains most of the spectral weight and is the relevant excitation in the system. Similar to the Landau and Pekar problem, dragging around a dressing cloud is costly and increases the mass of the attractive polaron. For positive energies the many-body system only supports a very broad resonance, as excitons interact repulsively with the Fermi surface.

This resonance is commonly referred to as the *repulsive polaron*.

Due to the large separation of scales, TMDs constitute an ideal platform to explore polaron physics and Bose-Fermi mixtures in parameter regimes, which are currently inaccessible in other systems. In Chapter 4, we discuss the two-dimensional polaron problem and demonstrate that experiments can reach strongly correlated regimes. As we shall see, this provides an interesting theoretical basis for tunable optical and electronic properties in solids.

Hubbard models in twisted multi-layer TMDs
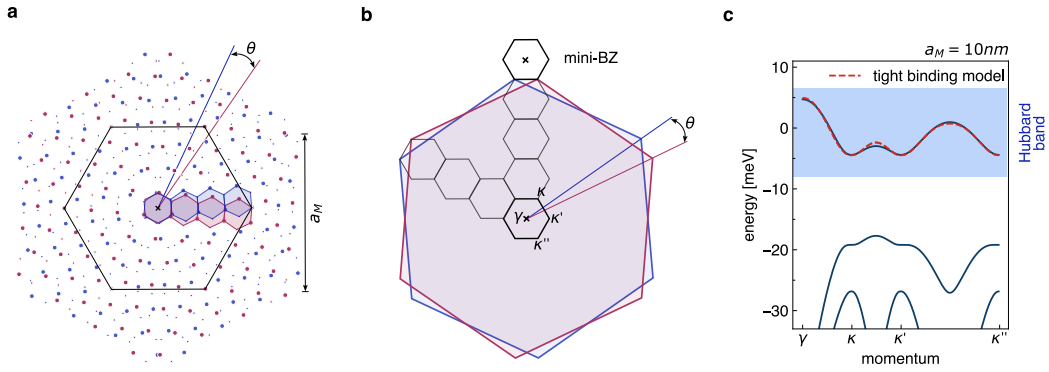
Figure 2.6: Moiré physics in bilayer systems. moiré lattice physics emerging from bilayer TMD structures. **a)** Top-down view of a two TMD layers, where top and bottom layer are twisted by an angle θ. The top (bottom) layer is shown in red (blue). The relative twist angle leads to a moiré pattern with lattice constant $a_M \gg a$. To identify the periodic structure, we have shown how the hexagonal Wigner-Seitz cells of both layers determine the larger moiré Wigner-Seitz cell. **b)** Equivalent momentum space picture. The Brillouin zone of the top and bottom layer are twisted, which leads to a smaller moiré Brillouin zone shown in black. We denote high-symmetry points in the mini Brillouin zone by small Greek letters (γ, κ, κ', κ'''). **c)** Approximate band structure for holes forming in a moiré potential with $a_M = 10$nm. Since the electronic energies strongly depend on the local stacking of the two layers, electrons can be localized in the moiré pattern. We show the band-structure of holes along a cut through the moiré Brillouin zone. There is an isolated hole-band, well described by a tight-binding model, taking into account only nearest and next-nearest neighbor tunneling, as shown by the red dashed line.

When waves with different frequencies ω and ω' are superimposed, the resulting wave is composed of rapid oscillations whose amplitude is modulated with a characteristic *beat* frequency $\omega - \omega'$. If the frequencies of the two waves can be tuned to be sufficiently close, one

can therefore engineer low-frequency modulations. Similarly, superimposed patterns in two dimensions exhibit the same effect: If two patterns differ only slightly in their orientation or lattice spacing, they will give rise to so-called *moiré patterns*, which repeat only on much larger scales.

This holds true even on the atomic scale, when two dimensional materials are stacked to form *heterostructures*. If the different layers are displaced or rotated with respect to each other, or differ in their lattice constants; a moiré pattern is generated, see Fig. 2.6a. In the simplest case, two layers are combined and doped charges feel a variation in their potential energy $V_M(\mathbf{r})$ due to the spatially varying atomic stackings, as illustrated in Fig. 2.6a). For large structures $V_M(\mathbf{r})$ is often well approximated by

$$V_M(\mathbf{r}) = \sum_{j=1}^{6} v_{\mathbf{g}_j} e^{i \mathbf{g}_j \cdot \mathbf{r}}, \qquad (2.18)$$

where $\{\mathbf{g}_j | j = 1, \dots, 6\}$ are the smallest reciprocal lattice vectors of the mini Brillouin zone. While the situation for twisted bilayers of Graphene turns out to be subtle [61], twisted bilayer TMDs can admit simple descriptions [44]. In the low energy limit the corresponding moiré bands are given by the single particle Hamiltonian:

$$\hat{h} = \frac{\hbar^2}{2m_e^*} \nabla^2 + V_M(\mathbf{r}), \qquad (2.19)$$

where we have suppressed potential dependence on internal the structure of the electrons. Generically this will lead to isolated bands, as shown in Fig. 2.6c), which can be well represented by a simple tight binding model once suitable Wannier functions are determined. Taking Coulomb interactions into account, the many-body Hamiltonian takes the form of a simple Hubbard model:

$$\hat{H} = - \sum_{ij,\sigma} t_{ij}\, c_{i,\sigma}^\dagger c_{j,\sigma} - \mu \sum_{i,\sigma} n_{i,\sigma} + U \sum_i n_{i,\uparrow} n_{i,\downarrow} + V \sum_{\langle i,j \rangle} \left(n_{i,\uparrow} + n_{i,\downarrow} \right) \left(n_{j,\uparrow} + n_{j,\downarrow} \right), \quad (2.20)$$

where t_{ij} is the hopping matrix and U and V specify on-site as well as nearest-neighbor interactions and we have neglected direct-exchange interactions [62]. In deriving Eq. 2.20, we have included the effect of the moiré potential on the hole bands only, such that we only

need to worry about a single spin degree of freedom, c.f. Fig. 2.3 b).

These Hubbard models enjoy a large amount of tunability, while being able to access low temperatures that can stabilize exotic quantum phases. Subsequently a lot of emphasis was placed on understanding electronic orders such as generalized Wigner crystals and Mott states [22, 48, 47, 63], while the magnetic properties of these models remains largely unexplored, see Ref. [46, 64, 65, 66] for notable exceptions. In Chapter 5, we discuss how topologically ordered spin states can be engineered in multilayer TMD structures.

3

Optical detection of strongly correlated electrons: Mott states, Wigner crystals, and quantum Hall states

This chapter is based on the publications

- "Optical signatures of charge order in a Mott-Wigner state", Yuya Shimazaki*, Clemens Kuhlenkamp*, Ido Schwartz*, Tomasz Smolenski, Kenji Watanabe, Takashi Taniguchi, Martin Kroner, Richard Schmidt, Michael Knap and Atac Imamoglu, Physical Review X 11, 021027 (2021)

- "Observation of Wigner crystal of electrons in a monolayer semiconductor", Tomasz Smoleński, Pavel E. Dolgirev, Clemens Kuhlenkamp, Alexander Popert, Yuya Shi-

mazaki, Patrick Back, Martin Kroner, K. Watanabe, T. Taniguchi, I. Esterlis, Eugene Demler and Atac Imamoğlu, Nature 595, 53-57 (2021)

Text, figures and structure have been modified for this thesis.

3.1 Signatures of correlated electrons in two dimensions

When Coulomb interactions dominate over kinetic energy, electrons in two dimensions organize themselves in various different phases. Famous examples include Quantum Hall states and Wigner crystals in continuum systems; as well as non-trivial Mott-Wigner insulators when electrons are confined to move in a periodic lattice. The quest to understand these phases has motivated numerous theoretical and experimental studies of solid state systems over the years [67, 68, 69, 70, 71, 72, 73, 74, 75, 76, 77, 78, 79]. Striking signatures of such phases were discovered also in the context of two dimensional materials [21, 80], which in turn sparked the development of novel methods to characterize electronic states [81]. Despite this effort, a majority of the reported signatures were not sensitive to the spatial correlations of the quantum state. Studies of the two-dimensional Wigner crystal, for example, have primarily focused on DC and AC conductivity measurements.

This has a simple reason: these correlations appear on much smaller scales than one could hope to access optically. Probing spatial correlations, however, remains a highly desireable task, as correlated systems have a strong tendency to break translational symmetries in order to minimize interaction energies.

In this chapter, we discuss a solution to this longstanding problem by introducing a class of particularly simple, yet completely generic optical signatures of emerging electronic order, that is directly sensitive to the spatial structure. First, we will discuss a theoretical model of optical signatures and then apply these ideas to probe the appearance of a Mott-Wigner state, a Wigner crystal and a magnetoroton mode in the integer Quantum Hall effect.

Due to strong exciton-electron interactions in TMD monolayers [82, 83, 51] described in Eq. 2.15, the formation of periodically ordered electrons has the potential to modify the spectrum of the exciton. As a result we will find that a new *Umklapp exciton-polaron* peak can appear in the resonant reflection spectrum, heralding the presence of electronic order. By applying band-theory the energy shift of this new resonance is determined by the reciprocal lattice vector of the emerging order and by the strength of exciton-electron interactions. For simplicity we focus only on a single layer which hosts the electrons.
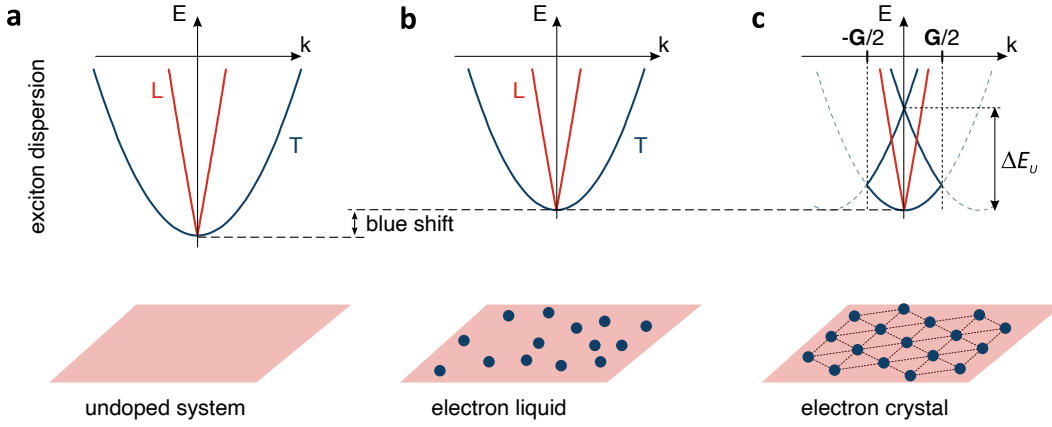
Figure 3.1: Electron crystallization and optical signatures. (a) Schematic depiction of the simplified exciton dispersion in a monolayer semiconductor hosting an electron system in various structural phases. The exciton bands are split by the electron-hole exchange interaction J into parabolic- and linear-in-momentum branches that correspond to the exciton dipole oriented along transverse (T) or longitudinal (L) directions with respect to the momentum vector. For the electrons in a liquid state **(b)**, the exciton bands are blueshifted with respect to the undoped case due to polaron formation **(a)**, while we neglect broadening due to scattering of the Fermi surface. In a crystalline phase **(c)**, the exciton umklapp scattering off the periodic electron lattice leads to band-folding. This gives rise to emergence of a new, zero-momentum umklapp resonance with an energy $\Delta E_U \simeq \hbar^2 \mathbf{G}^2/2M$ determined by reciprocal lattice vector $\mathbf{G}$ of the electronic order.

We first introduce the Hamiltonian describing a dilute concentration of excitons. Due to the steep light-cone, optically active excitons carry momentum $\mathbf{k} = 0$ and are σ^+ (K-valley) and σ^- (K'-valley) polarized. However, for exciton momenta outside the light cone, the long-range electron-hole exchange interaction strongly couples the K and K' valley excitons [84, 85, 86]. In the pseudo-spin basis, where spin-up (down) corresponds to an exciton

in the $K(K')$ valley, the dynamics of an exciton is described by the following Hamiltonian

$$H_0 = \sum_{\mathbf{k}} \begin{pmatrix} x^\dagger_{\mathbf{k},K} \\ x^\dagger_{\mathbf{k},K'} \end{pmatrix}^T \left[\frac{\hbar^2 \mathbf{k}^2}{2m_X} + \frac{|\mathbf{k}|}{|K|}J \begin{pmatrix} 0 & e^{-i2\theta} \\ e^{+i2\theta} & 0 \end{pmatrix} + \frac{|\mathbf{k}|}{|K|}J \right] \begin{pmatrix} x_{\mathbf{k},K} \\ x_{\mathbf{k},K'} \end{pmatrix}, \quad (3.1)$$

where $x^\dagger_{\mathbf{k},K}$ ($x^\dagger_{\mathbf{k},K'}$) creates an exciton in the $K(K')$ valley with center of mass momentum $\mathbf{k}$, $\hbar$ is Planck's constant, m_X is the exciton mass, $\theta = \mathrm{atan}(k_y/k_x)$ and J is the exchange coupling[*]. The second and the third terms of Eq. 3.1 describe inter-valley and intra-valley exchange interaction, respectively. We remark that the exchange coupling is not easily accessible experimentally, but that its value can be estimated to be $J \simeq 300\mathrm{meV}$[†]. The exciton dispersions are given by $E^\pm(\mathbf{k}) = \frac{\hbar^2 \mathbf{k}^2}{2m_X} + \frac{|\mathbf{k}|}{|K|}J \pm \frac{|\mathbf{k}|}{|K|}J$ and are schematically depicted in Fig. 3.1 a. Exchange interactions split the polarizations into two branches with parabolic and linear dispersion. The linearly dispersing excitons fall on a steep cone, which leads to a large energy detuning from the parabolic branch.

The interaction between electrons and excitons is modelled by an effective repulsive contact interaction, which is justified, as we limit our discussion to features that appear at low energies $0 \le E \ll |E_T^0|$. The electron-exciton interaction Hamiltonian then takes the form:

$$H^{\mathrm{int}}_{e-x} = \int d^2r \, \lambda^{e-x} \left[\hat{n}_e(\mathbf{r}) \hat{n}_X^K(\mathbf{r}) + \hat{n}_e(\mathbf{r}) \hat{n}_X^{K'}(\mathbf{r}) \right], \quad (3.2)$$

where $\hat{n}_X^{K,(K')}$ is the density operator of excitons in the K (K') valley and $\hat{n}_e$ is the density operator of the electrons. The interaction itself is short-range and repulsive and we assume for simplicity that the strength λ^{e-x} is identical for both polarizations. Once electrons choose to order, it becomes sensible to perform an expansion around the order parameter $\langle \hat{n}_e(\mathbf{r}) \rangle = \sum_{\{\mathbf{G}_i\}} e^{i\mathbf{G}_i \mathbf{r}} \tilde{n}(\mathbf{G}_i)$, which leads to a simple mean field model

$$H_{\mathrm{eff}} = H_0 + \int d^2r \, \lambda^{e-x} \left[\hat{n}_X^K(\mathbf{r}) + \hat{n}_X^{K'}(\mathbf{r}) \right] \langle \hat{n}_e(\mathbf{r}) \rangle, \quad (3.3)$$

---

[*]To model the experiments we use $m_X = m_e^* + m_h^* = 1.3\,m_e$, where $m_e^* = 0.7\,m_e$ [87] and $m_h^* = 0.6\,m_e$ [88, 89] are the effective masses of electrons and holes.

[†]While first principle calculations yield large values of $J \sim 1$ eV, we expect, that the experimentally relevant coupling is likely to be reduced by dielectric screening due to the hBN encapsulation, as well as due to screening by electrons [86]. The conclusions in this chapter are however insensitive to the precise value of J and are unaffected for a range of couplings 1 eV $\ge J \ge$ 150 meV.

This suggests the following picture: excitons feel a spatially modulated potential, which allows excitonic states with momentum $\mathbf{k}$ and $\mathbf{k} + \mathbf{G}_i$ to hybridize. Via this hybridization, excitons carrying the ordering wavevector of the electrons can pick up oscillator strength from the optically bright $\mathbf{k} = 0$ modes and become visible in optical experiments. We refer to excitons carrying a reciprocal lattice momentum colloquially as *umklapp excitons*. These bright states allow us to distinguish liquid and crystalline order, as shown in Fig. 3.1 b-c. The energy separation between the exciton and the first Umklapp scattered exciton in the limit of weak λ^{e-x} is given by the following expression

$$\Delta E_{X^U-X} = \frac{\hbar^2 |\mathbf{G}_1|^2}{2m_X}, \tag{3.4}$$

where $\mathbf{G}_1$ is chosen from the smallest reciprocal lattice vectors of the electronic order.

A full calculation yields further restrictions due to the symmetry of the electronic order. We illustrate this for electrons ordered in a triangular lattice —the configuration that optimizes Coulomb energy in two dimensions. There, the six reciprocal lattice vectors suggest 12 bright states, arising from the K and K′ valley. However, only two out of these bands can become optically active at the Γ point: one in σ^+ polarization and one in σ^- polarization. The restricted number of bright states is a consequence of the C_6 symmetry of the triangular lattice. Owing to strong long-range electron-hole exchange interaction, 6 of these bands (associated with longitudinally-polarized excitons) are pushed to high energies, and are therefore inaccessible. The remaining 6 lower-energy finite-momentum excitons mix with the two main ($k = 0$) resonances via the electronic lattice potential. The C_6 symmetry only allows bright $k = 0$ states to couple to umklapp states in the same irreducible representation. Consequently, the $k = 0$ exciton in $K^\pm$ valley mixes only with one $\sigma^\pm$-polarized umklapp state, corresponding to a properly-phased-superposition of the exciton states at $\mathbf{k} = \mathbf{G}_i$ with a C_6 eigenvalue of $\exp(\pm i\pi/3)$. The remaining four umklapp bands remain optically dark which, as we will see, is in agreement with experimental observations.

The relative oscillator-strength of the Umklapp states can be estimated by their zero-momentum exciton content

$$\frac{|\langle \mathbf{k} = 0 | X^U(\mathbf{\Gamma}) \rangle|^2}{|\langle \mathbf{k} = 0 | X(\mathbf{\Gamma}) \rangle|^2}, \tag{3.5}$$

where $|X\rangle$ and $|X^U\rangle$ are the exciton and the bright Umklapp-exciton states of a given po-

larization, while $\mathbf{\Gamma}$ labels vanishing lattice momentum. In Eq. 3.5, the vector $|\mathbf{k}\rangle$ is a plane wave state of the exciton with proper momentum $\mathbf{k}$. The amount of mixing and the band splittings are determined by the strength of the potential and the density profile of the electrons. We will show later, that the relative brightness of the Umklapp state can reach several percent compared to the main exciton resonance.

We also highlight, that this constitutes a non-invasive probe. The delocalized nature of optically generated excitons ensures that the electronic states are largely unperturbed if the intensity of the probe-light is sufficiently weak.

3.2.1 Magnetic field dependence

A main concern of this proposal, is that additional bright states could have various origins and are not bound to originate from finite momentum $\mathbf{k} = \mathbf{G}$ excitons. Strikingly, we can circumvent this issue and identify finite-momentum excitons by their unusual properties in finite magnetic fields. In the presence of a perpendicular magnetic field B, the excitonic Hamiltonian Eq. 3.6 picks up an additional Zeeman term:

$$H = H_0 + \frac{1}{2} g \mu_B B \sum_{\mathbf{k}} \begin{pmatrix} x^\dagger_{\mathbf{k},K} \\ x^\dagger_{\mathbf{k},K'} \end{pmatrix}^T \sigma_z \begin{pmatrix} x_{\mathbf{k},K} \\ x_{\mathbf{k},K'} \end{pmatrix}, \tag{3.6}$$

where $g \approx 4.3$ is the exciton g-factor which we assume to be independent of the exciton momentum [90, 91, 92, 93]. This coupling leads to the usual Zeeman splitting of $\mathbf{k} = 0$ excitons, which lifts the degeneracy of the σ^+ and σ^- polarizations. For excitons with finite momentum $\mathbf{k}$, however, the exchange interaction quickly dominates over the Zeeman term $J|\mathbf{k}|/|K| \gg g\mu_B B$. This is another way of saying, that finite momentum excitons —and Umklapp excitons in particular— are strongly polarized in-plane and will resist external magnetic fields. If the Umklapp states are sufficiently bright, this behaviour can be confirmed experimentally, simply by switching on external fields.

Before moving on to experiments, we note that by using H_{eff}, we neglect the dynamical dressing of excitons by virtual excitations out of the electronic state. While this is an excellent approximation in the presence of classical charge order, we abandon this assumption at

the end of this chapter, where we discuss the optical signatures of roton-modes in quantum Hall states.
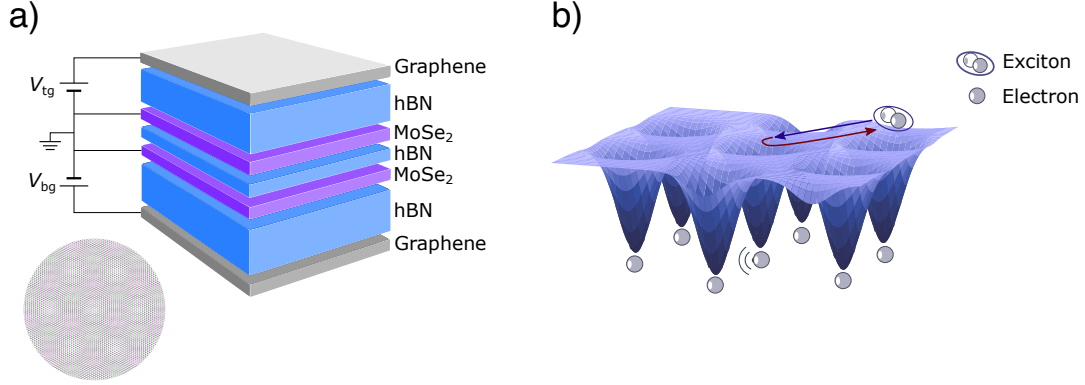
Figure 3.2: Moiré lattice in $MoSe_2/hBN/MoSe_2$ and basic characterization. (a) Schematic picture of the device structure. The left bottom picture shows a moiré lattice. (b) Schematic picture of the potential for excitons created by electrons trapped in a moiré lattice.

Here we apply the theoretical model to study a twisted $MoSe_2/hBN/MoSe_2$ homobilayer structure, which exhibits an incompressible single-layer Mott state for unity-filling of the underlying electronic moiré potential [47]. The device is shown schematically in Fig. 3.2 a). In comparison to hetero-bilayer structures [22, 48], the presence of monolayer hBN in between the $MoSe_2$ monolayers leads to two new features: first, the on-site and possibly inter-site Coulomb repulsion energy exceeds the strength of the moiré potential, which is drastically weakened by the hBN monolayer. Second, the energy difference between the electronic states in the two layers is tunable, resulting in a robust layer pseudo-spin degree-of-freedom that can be controlled using an applied vertical electric field.

Before proceeding, we note that a moiré potential in bilayer structures generally also imprints directly on excitons [94, 95, 96, 97, 98]. This periodic potential is particularly strong if the TMD monolayers are in direct contact, which has lead to the observation excitonic resonances arising either from localization at high symmetry stacking points or from Umklapp processes [99, 100, 101]. In stark contrast to these works, the periodic static moiré potential experienced by the excitons in our sample is weak compared to the exciton linewidth due to the hBN barrier layer, which is why we can neglect a direct effect of the Moire potential on the excitons.
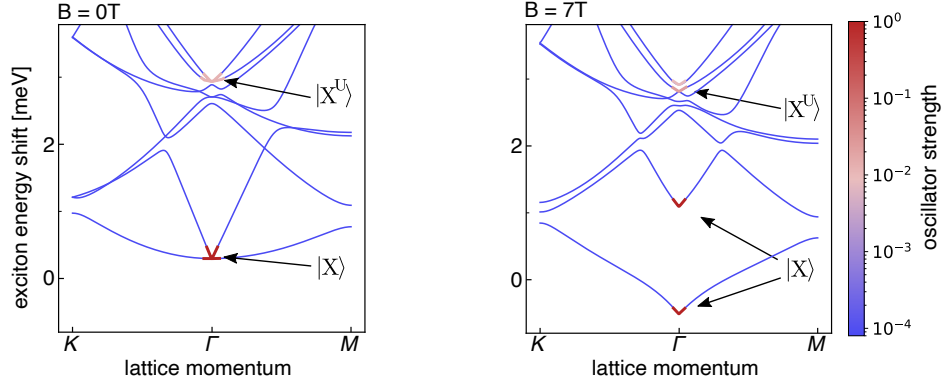
Figure 3.3: Exciton band structure based on the effective model. Exciton bands along a path in a moiré Brillouin zone, assuming $J = 300$ meV. The oscillator strength of each state is indicated by the color bar, which is saturated for all blue lines. As photons carry almost vanishing momentum, only modes close to the Γ-point may obtain finite oscillator strength (we artificially extended the momentum range of the bright states for better visibility). While most states remain dark, only a single Umklapp band per polarization obtains sizable oscillator strength. (Left) Dispersion in the absence of magnetic field. The splitting between Umklapp state and main resonance is ~ 3 meV. The additional bright state carries 1.2% of the oscillator strength of the bare exciton. The oscillator strength of higher bands is significantly suppressed due to the larger energy splitting, which reduces the coupling to light. (Right) Exciton dispersion for $B = 7$ T. While the main resonance splits significantly, the Umklapp peaks are only marginally affected by the magnetic field.

Since the moiré potential is expected to be weak also for electrons and Coulomb interactions are long-ranged, the electronic wavefunctions will localize in the incompressible Mott-like phase. Up to details of their wavefunction, electrons will therefore generate an effective potential for the excitons, as illustrated by the cartoon in Fig. 3.2 b). Assuming that the electrons are rigidly locked in place in the correlated Mott state, we can model the system with Eq. 3.3. We phenomenologically fix the Hartree shift induced by λ^{e-x} to match the experimentally measured blue-shift of the repulsive-polaron resonance induced by the electrons at low densities. This determines $\lambda^{e-x} = 2.1 \times 10^{-12}$ meV $\cdot$ cm^2 to produce an excitonic blue-shift of 0.4 meV at fillings slightly away from $\nu = 1$, where the electron density is expected to be homogeneous. To keep our model minimal, we assume a Gaussian density profile for electrons $\langle \hat{n}_e(\mathbf{r}) \rangle = \frac{1}{2\pi\xi^2} \sum_{\mathbf{R}} e^{-\frac{1}{2\xi^2}(\mathbf{r}-\mathbf{R})^2}$, where $\mathbf{R}$ is a triangular lattice vector and ξ characterizes the extent of the electronic wave functions around the moiré sites [102]. The lattice constant a_M for this device has been previously determined using different methods in [47] to be $\simeq 25$ nm. We show the band-structure resulting from the electron-induced potential

in Fig. 3.3(b) for an electronic lattice with $a_M = 25$ nm and $\xi = 4$ nm. While the precise localization of the electrons is not known, we have checked that our results are roughly independent on ξ's within 3 nm $< \xi < 6$ nm. The new bands in the moiré Brillouin zone appear as a consequence of the periodic excitonic potential, which couples excitons carrying momentum $\mathbf{k} = \mathbf{G}_i$ with optically active $\mathbf{k} = 0$ excitons. Using Eq. 3.5 our model predicts a an oscillator strength of $\simeq 1.2\%$ relative to the main peak, a value well within experimental detection capabilities. As mentioned in the theory section, only two states among the first Umklapp band become bright. To have non-vanishing coupling to light the relevant states need to be circularly polarized. This corresponds to eigenstates of C_6 with eigenvalues $\exp(il\pi/3)$ where $l = \pm 1$. The oscillator strength of the bright resonances decreases rapidly as the Umklapp energy increases; which is why we expect that only the first Umklapp band is accessible in experiments.

3.3.1 EXPERIMENTAL OBSERVATION IN A TMD BILAYER
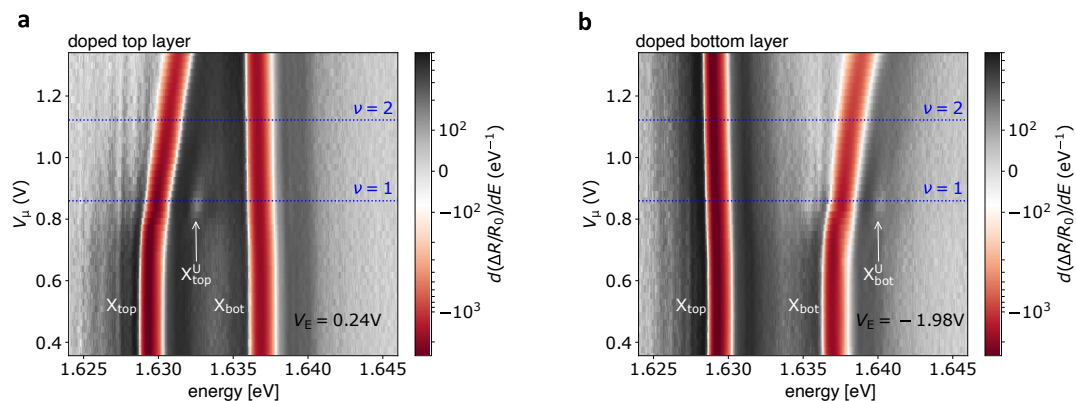
Figure 3.4: Exciton resonances in the presence of charge doping. Differential reflectance differentiated with respect to energy as a function of chemical potential V_μ. **a** We fix $V_E = 0.24$ V, to ensure only the top layer is doped. **b** We fix $V_E = -1.98$ V, to ensure only the bottom layer is doped. In both **a** and **b** the exciton resonances of the two layers are clearly visible. A Mott state appears for $\nu = 1$ indicated by the dashed blue line. At this point we observe the appearance of additional bright states at higher energies, which we denote by $X^U_{top/bot}$. The scale of the color bars are logarithmic for $|d(\Delta R/R_0)/dE| > 10^2$ eV^{-1} and linear for $|d(\Delta R/R_0)/dE| < 10^2$ eV^{-1}.

In the experiment graphene sheets on the top and bottom of the device are used as gates. We define the gate voltage axes as V_E and V_μ, as linear combination of top and bottom gate

voltages, which leave the electric field and the chemical potential invariant. This allows us to change the chemical potential in each layer individually. The system is studied by optically probing the excitonic spectral function via the differential reflectance ($\Delta R / R_0 = (R - R_0)/R_0$). R denotes the reflectance of the $MoSe_2$/hBN/$MoSe_2$ homobilayer structure, whereas R_0 is the background reflectance obtained from a region of the sample without $MoSe_2$ layers. Even in the absence of charge doping, the exciton resonances in the top and bottom layer posses a small energy shift, which we attribute to inhomogeneous strain [103, 104, 105]. This allows us to distinguish the optical response of the top and bottom $MoSe_2$ layers. When one of the layers is electron doped, exciton-electron interactions lead a new attractive resonance around the trion-binding energy of $\simeq$ 30meV and a blue-shift of the resonance frequency of the exciton due to polaron formation [57, 106]. Since the exciton-electron interactions are short-ranged and tunneling of electrons is suppressed by the hBN layer, excitons in a given layer scatter almost exclusively with electrons in the same layer.

The electrons become visibly correlated in a half-filled moiré subband ($\nu = 1$), where each moiré site is occupied by a single electron. Since our structure has a layer degree of freedom, we specify the electron filling factor of top and bottom layers as ν_{top} and ν_{bot}, with $\nu = \nu_{top} + \nu_{bot}$ (see the Supplemental Material S2 in Ref. [107] for the identification of filling). In Fig. 3.4(a), we show the chemical potential V_μ dependence of the reflectance spectrum. We choose a fixed V_E for which the bottom layer remains neutral and only the filling of the top layer is tuned along the V_μ axis[‡]. Remarkably, once the top layer is doped to $\nu = 1$ where $(\nu_{top}, \nu_{bot}) = (1, 0)$, an additional higher energy exciton resonance labeled as X_{top}^U appears. The estimated energy separation between X_{top} and X_{top}^U is $\simeq$ 2.7 meV, which agrees well with the expectation based on our theoretical model. A corresponding resonance X_{bot}^U also appears when only the bottom layer is doped to $\nu = 1$, which is indicated in Fig. 3.4(b). The energy separation between X_{bot} and X_{bot}^U is also estimated to be $\simeq$ 2.7 meV. As discussed in the previous section, the energy of the new bright states should be determined predominantly by the reciprocal lattice vector of the electron-induced potential, which is fixed by the moiré-periodicity.

34
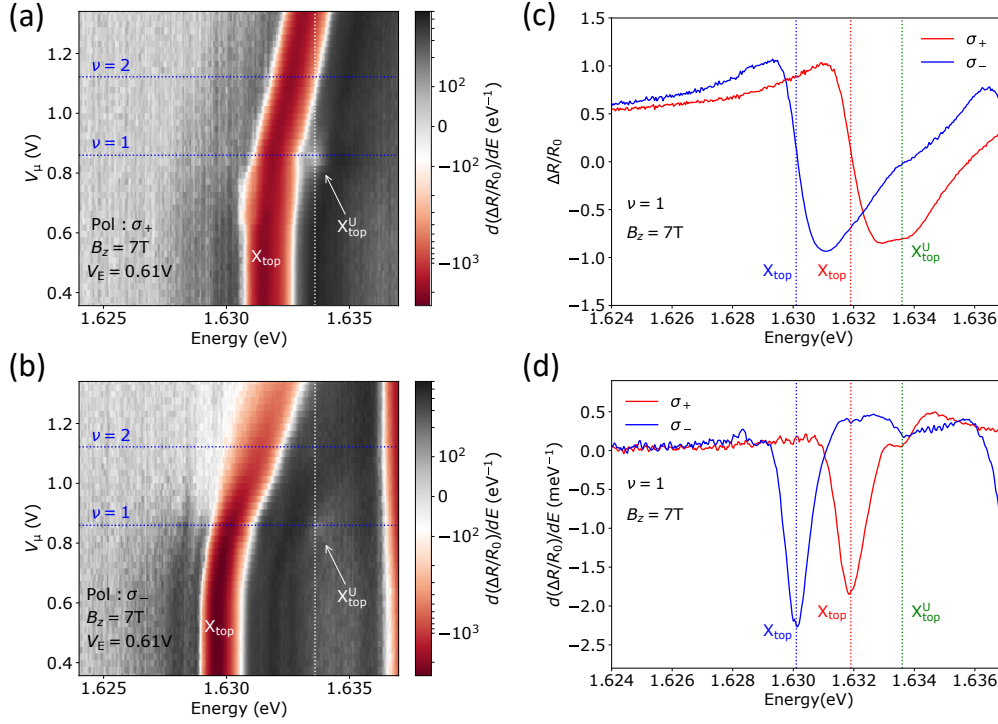
Figure 3.5: Exciton and Umklapp exciton resonances at $\nu = 1$ under magnetic field $B_z = 7$ T. (a), (b) V_μ dependence of differential reflectance differentiated with respect to energy E in σ_+ (a) and σ_- (b) polarization. (c), (d) Line cuts of the reflectance spectrum (c) and its energy differentiation (d) at $\nu = 1$, $V_E = 0.61$ V.

3.3.2 Magnetic field dependence of Umklapp states

The matching of observed and predicted energy splittings as well as oscillator strenghts, is suggestive, but does not unambiguously identify the Umklapp states as originating from finite momentum. As discussed in the theory section, one should check their magnetic field dependence to see if the excitons are indeed in-plane polarized. Therefore we apply a magnetic field of $B = 7$ T. Polarization resolved $\Delta R/R_0$ measurements show the emergence of Umklapp states (X_{top}^U) in both σ_+ and σ_- polarization around $\nu = 1$ where $(\nu_{top}, \nu_{bot}) = (1,0)$, see Fig. 3.5(a) and (b). In Fig. 3.5(c) and 3.5(d) we show the line cuts of the $\Delta R/R_0$ spectrum and its derivative with respect to emission energy at $\nu = 1$ where $(\nu_{top}, \nu_{bot}) = (1,0)$. Compared to the large Zeeman splitting of X_{top} of $\simeq 2$ meV, the energy splitting of

---

‡This is also evidenced by the blue shift of X_{top} resonance

X_{top}^U is much smaller.

This observation has two main implications: On the one hand, the vanishingly small Zeeman splitting of the high energy resonances appearing at $\nu = 1$ confirms their identification as Umklapp peaks. On the other hand, our measurements provide a direct evidence for the important role played by long-range electron-hole exchange interaction for high momentum exciton states. Overall, the appearance of a single Umklapp line per polarization, its estimated oscillator strength, and its behaviour under magnetic fields are in good agreement with our theoretical predictions. This confirms that Umklapp exciton/repulsive-polaron resonances provide a direct probe of the periodic structure of the Mott-like correlated insulating state. We emphasize that previously reported optical spectroscopy of Mott-like correlated insulators states revealed signatures of incompressibility, but a direct evidence for the presence of periodic ordering of electrons has been elusive. The observation of the Umklapp exciton resonance on the other hand, is a direct consequence of the emergence of a periodic lattice of electrons.

In the next section, we shift gears to investigate the appearance of Umklapp peaks in a compressible state, where it provides direct evidence for spontaneous breaking of translational invariance due to formation of a Wigner crystal [26, 68, 108, 34].

The electronic properties of most metals and semiconductors at low temperatures can be described using Fermi liquid theory. This is a consequence of the fact that in most material systems typical kinetic energy of electrons exceeds the Coulomb interaction energy. Investigation of strong electronic correlations that emerge in the complementary regime where the ratio r_s of the Coulomb interactions to the kinetic energy well exceeds unity has been a holy grail of condensed-matter physics. As discussed in the introduction a landmark state of strongly correlated matter is a Wigner crystal [26]. In this state electrons spontaneously break translational symmetry and form a periodic lattice. Quantum Monte Carlo calculations [27] indicate that $r_s \gtrsim 30$ is necessary for the Wigner crystal to be the ground state of a two dimensional electron system. Since $r_s = m_e^* e^2 / (4\pi\varepsilon_0 \varepsilon \hbar^2 \sqrt{\pi n_e})$ with ε, n_e and m_e^* denoting the dielectric constant, electron density and effective electron mass, systems with large electron masses m_e^*, low densities n_e and weak screening ε should be used to reach the required r_s values. However, simultaneously satisfying the above mentioned stringent conditions is difficult. Up to a few remarkable exceptions [109, 110, 111], this has hindered the search for an electronic Wigner crystal in the absence of magnetic fields. Instead, the majority of the experimental efforts [67, 68, 69, 70, 71, 72, 73, 74, 75, 76, 77, 78, 79] have focused on two dimensional electron gases in the presence of large magnetic fields $B > 0$ at n_e much lower than the Landau level (LL) degeneracy. In this regime, the magnetic field quenches the kinetic energy of electrons and Coulomb interactions remain the only relevant energy scale.

As we have discussed in the introduction, TMD monolayers offer new opportunities to overcome this conundrum. One the one hand, high m_e^* and reduced screening makes it possible to reach the high r_s values necessary for $n_e \sim 1 \cdot 10^{11}$ cm^{-2} even when $B = 0$: [112]. On the other hand, Umklapp scattering of excitons allows for direct optical signatures of translational symmetry breaking. Here we discuss the principle behind optical signatures of crystallization and present the recently found experimental evidence for an electronic Wigner crystal in TMD devices [113, 114]. A more careful experimental analysis is described in the main text and the supplemental material of the original publication [113].
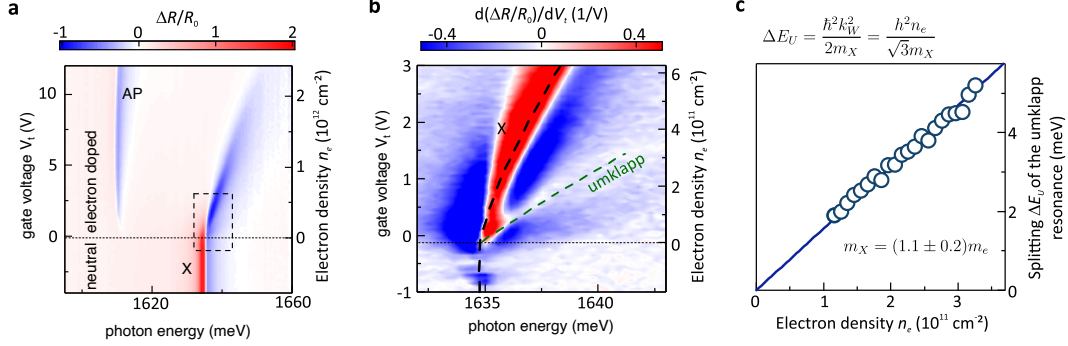
Figure 3.6: Optical signatures of a Wigner crystal at zero magnetic field and mK-temperatures.
(**a**) Doping-dependence of the reflectance contrast spectrum featuring charge-neutral and electron-doped regions. (**b**) Close-up into the exciton spectral range in the low-density regime (marked by dashed rectangle in panel **a**) showing derivative of reflectance contrast with respect to the top gate voltage. The weak, higher-energy resonance is due to Umklapp scattering of the excitons off the electron Wigner crystal. Black dashed line marks the fitted position E_X of the exciton resonance, while the green line corresponds to the expected position of the Umklapp peak $E_X + \Delta E_U$. (**c**) Energy splitting ΔE_U between the exciton and Umklapp peaks determined as a function of the electron density n_e. Solid line marks the linear fit corresponding to the exciton mass of $m_X = (1.1 \pm 0.2)m_e$.

We first discuss what has been observed experimentally. The optical reflectance contrast spectrum $(R - R_0)/R_0 = \Delta R/R_0$ of a TMD monolayer at $B = 0$ and $T = 80$ mK is shown in Fig. 3.6**a**. R is the reflectance measured in the MoSe$_2$-monolayer region, while R_0 represents a background reflectance. As in the bilayer case charge doping can be controlled by applying a voltage V_t to a nearby graphene gate. The presence of free electrons then dresses optical excitations due to interactions with the Fermi sea. This leads to the formation of an attractive polaron (marked as AP in the figure), which is clearly visible in Fig. 3.6**a** at $V_t > 0$. In parallel, the exciton transforms into a repulsive polaron that blueshifts with increasing n_e. The interaction parameter r_s is maximal for small electron densities, so we focus on the low n_e region to search for signatures of periodic order. Remarkably, after differentiating $\Delta R/R_0$ with respect to V_t, or equivalently n_e (Fig. 3.6**b**) an Umklapp peak appears in the spectral the spectral vicinity of the exciton resonance for low densities. The Umklapp resonance blueshifts faster than the exciton with increasing n_e and becomes indiscernible at $n_e \gtrsim 3 \cdot 10^{11}$ cm^{-2}. At the same time, its energy splitting ΔE_U from the main exciton

transition, determined by fitting both resonances with dispersive Lorentzian spectral profiles [113], scales linearly with n_e and extrapolates to zero at $n_e = 0$ (Fig. 3.6c). Electrons in this systems form a Wigner crystal at low n_e and low temperature!

Ordering wavevector— The energy of the Umklapp resonance ΔE_U is simply determined by the exciton kinetic energy $\hbar^2 \mathbf{G}^2/2M$ at an ordering wavevector $\mathbf{G}$, where M is the exciton mass. Here the reciprocal lattice vector $|\mathbf{G}| \sim 1/a_W \sim \sqrt{n_e}$, which implies that the Umklapp energy increases linearly with n_e, as the Wigner crystals lattice constant a_W is reduced, in full agreement with the experiments. Knowing the exciton mass therefore allows us to estimate $|\mathbf{G}|$ of the Wigner crystal. Conversely, assuming that electrons form a triangular lattice, the Umklapp energy is given by $\Delta E_U/n_e = h^2/\sqrt{3}m_X$. Thus, by extracting the slope of the Umklapp peak from the data in Fig. 3.6c, one can determine the exciton mass. Experimentally, it is more natural to fit the slope, which yields $m_X = (1.1 \pm 0.2)m_e$ which is in good agreement with previous literature $m_X = 1.3m_e$ [88, 87].

Order parameter and melting transition— Recall that the order parameters for the Wigner crystal phase are expectation values of

$$\langle \tilde{n}(\mathbf{k}) \rangle \neq 0, \quad \text{for any } \mathbf{k} \neq 0. \tag{3.7}$$

Up to a factor of λ^{e-x} it is exactly these Fourier harmonics $\tilde{n}(\mathbf{k})$ which introduce the periodic potential to the excitons. Consequently, the emergence of the Umklapp resonances is directly related to the spontaneous symmetry breaking of the Wigner crystal. Strikingly, we can infer both the *wavevector* $|\mathbf{G}|$ and the *strength of the order parameter* by carefully analyzing the resonance. Based on Fermi's golden rule, the oscillator strength of the Umklapp peak scales roughly with the squared order parameter $\tilde{n}(\mathbf{G})^2$ for small λ^{e-x}. As temperature is increased the order parameter, and therefore the oscillator strength of the Umklapp peak are suppressed. Figure 3.7a shows the temperature dependence of back-gate (V_b) voltage evolution of $d(\Delta R/R_0)/dV_b$. Strikingly, the Umklapp signature becomes almost indiscernible already at $T \approx 10$ K and disappears completely for $T = 17$ K, even though the main exciton transition remains only weakly affected by increasing T. This observation signals a phase transition from a Wigner crystal to a liquid state. To determine the corresponding melting temperature T_m, we fix $n_e \approx 1.6 \cdot 10^{11}$ cm^{-2} where the Umklapp resonance is particularly well-resolved and analyze T-dependence of the average value of $d(\Delta R/R_0)/dV_b$
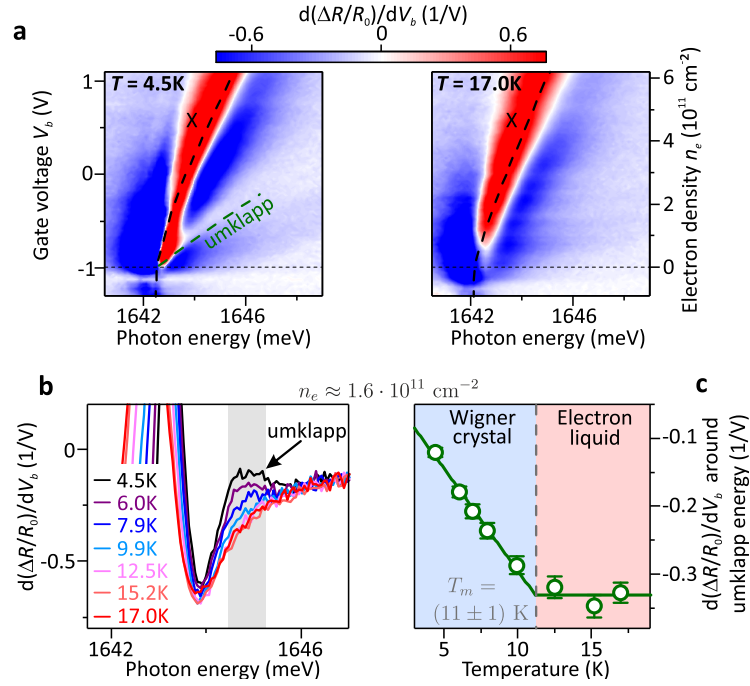
Figure 3.7: Phase transition between Wigner crystal and electron liquid at $B = 0$. (**a**) Back-gate-voltage evolution of the derivative of the reflectance contrast spectrum with respect to V_b measured in a variable-temperature-insert-based setup at $B = 0$ and different temperatures of the sample: 4.5 K (left) and 17.0 K (right). Black dashed lines indicate the fitted energy E_X of the main exciton resonance, while green one represents the expected position of the Umklapp peak $E_X + \hbar^2 n_e / \sqrt{3} m_X$ for the triangular geometry of the Wigner crystal lattice and $m_X = 1.3 m_e$. (**b**) Cross-sections through color-scale plots from panel (**a**) at $V_b = -0.45$ V corresponding to $n_e \approx 1.6 \cdot 10^{11}$ cm^{-2}. (**c**) Temperature-dependent differentiated reflectance contrast $\mathrm{d}(\Delta R/R_0)/\mathrm{d}V_b$ averaged over 0.8-meV-wide energy range around the Umklapp resonance (marked by the shaded region in panel **b**). Solid line represents the fit of the data points with a linear decrease at temperatures $T < T_m$ and constant background level at $T > T_m$, which corresponds to the Wigner crystal melting temperature of $T_m = (11 \pm 1)$ K.

in a spectral window around the Umklapp energy (see Fig. 3.7**b**). As shown in Fig. 3.7**c**, such Umklapp amplitude initially exhibits a linear decrease with T and then saturates at a constant background level for larger T. By tracing the crossover between these two regimes we extract $T_m = (11 \pm 1)$ K. Similar values of T_m are also obtained for n_e ranging from $1.2 - 1.9 \cdot 10^{11}$ cm^{-2} (see the supplemental material of Ref. [113]). Based on the previous discussion, the linear decrease in the spectrum suggests a decrease of order parameter with exponent $1/2$. This is expected from standard mean field calculations of continuous phase

transitions. Nevertheless crystallization transitions (in particular for triangular lattices) are generally first order, which is based on arguments dating back to Landau. Both in theory and experiments it is usually a difficult task to determine the nature of the a quantum phase transition. This can have a simple explanation: the jump in order parameter may be too small to resolve and could be smoothed out by disorder. In the future it will be interesting to explore melting transitions of electronic crystals in more detail. Before moving on, we remark that signatures persist at finite magnetic fields and all the usual checks of the Umklapp peak can be performed. To make a long story short, we find that the experiment results agree with theory models based on Eq. 3.3 and Eq. 3.6 when $n_e(\mathbf{x})$ in the Wigner crystal is modelled by Gaussian quantum states [113]. However, the presence of magnetic fields can also lead to qualitatively new features in the optical spectrum, which are discussed in the next section.

3.5 Optical signatures of correlations in liquids: Magneto-rotons in the Integer Quantum Hall state

We now shift our focus to explore correlations in electronic liquids. On a first glance, one may expect that these states have rather unremarkable signatures: the average electron density is homogeneous in a liquid, therefore interactions do not affect the optical response in any obvious way. Thankfully, it turns out that the physics is much richer even for linear-response quantities. Imagine a strongly correlated liquid that is in close proximity to a crystallization transition, where the crystalline state is characterized by an ordering wave vector $\mathbf{G}$. If we perturb the density distribution of the liquid by a generic wave-like pattern, this will be accompanied by a large energy cost as density-accumulations in the liquid generically repel each other. However if the modulation-pattern is described by a wave vector close to $\mathbf{G}$, the energy of the configuration can be low as this resembles the nearby crystalline ground state. A particularly nice example of this effect is found at finite magnetic fields B, if the electrons form integer or fractional quantum Hall states. There, density excitations are gapped and are dominated by a single eigenstate known as the *magneto-plasmon*. This mode can become soft when it carries a reciprocal lattice momentum $\mathbf{G}$ of the nearby Wigner crystal. We now derive the effects of such low-lying density-modes on optical excitations.

a

b magneto-plasmon dispersion
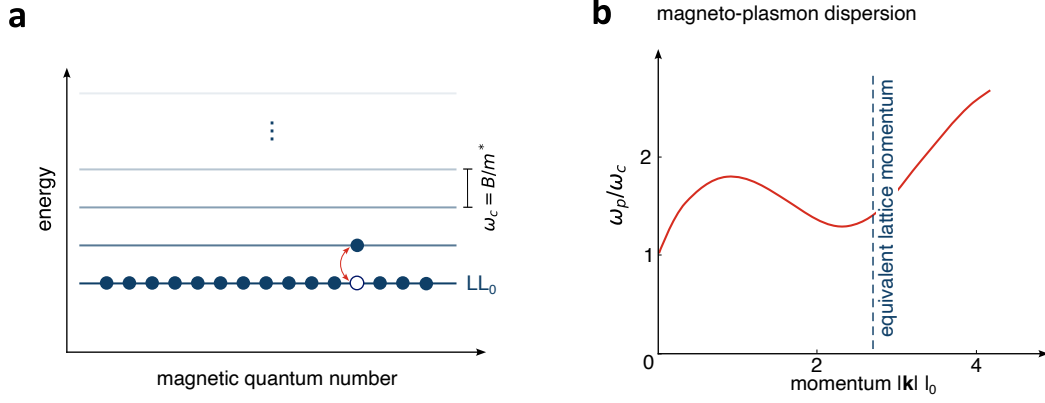
Figure 3.8: Excitations of Quantum Hall states. (a) Landau levels forming in the the conduction band of a two dimensional Fermi liquid in finite mangetic fields. The spacing of Landau levels defines the cyclotron frequency $\hbar\omega_c = B/m^*$. In the $\nu = 1$ state the lowest Landau level (LL$_0$) is fully occupied and the system is an insulator. The excitation gap is then simply given by $\hbar\omega_c$, which is highlighted by the red double arrow. Kohn's theorem guarantees that there exists an exact excitation at $\hbar\omega_c$ even in the presence of interactions. (b) Schematic depiction of the low energy density-wave excitations in the Quantum Hall state, known as *magneto-plasmons*. Interactions endow their dispersion with a characteristic *roton*-minimum close to the reciprocal lattice vector of a nearby crystalline configuration, which is indicated by the dashed line.

Studies of quantum Hall states are often restricted to their rich ground-state properties. Deep inside integer and fractional quantum Hall phases this is a good starting point. However, once a phase transition is approached, the dynamical collective excitations start to play important roles. Such excited states can be highly non-trivial in the presence of strong correlations: while charged excitations can be fractionalized, neutral (density) excitations carry information about nearby phases. In the presence of magnetic fields the kinetic energy is fully quenched and eigenstates form flat Landau levels (LL). Correlations are then quantified by the ratio of Coulomb interaction (E_c) to the cyclotron energy ($\hbar\omega_c$): $\kappa = E_c/\hbar\omega_c = m_e^* e/(4\pi\varepsilon_0\varepsilon l_0\hbar B) = r_s\sqrt{\nu/2}$, where $l_0 = \sqrt{\hbar/(eB)}$ and ν denote the magnetic length and LL filling factor, respectively[§]. For simplicity we focus on $\nu = 1$ quantum Hall states, where the lowest Landau level (LL$_0$) is fully occupied, see Fig. 3.8 **a**. A simple neutral excited states is formed when an electron is lifted to the next Landau level, indicated by the red

---

[§]Since $\kappa \geq 30$ for $B \sim 5$ T in TMD monolayers, interactions lead to strong LL mixing and it is no longer possible to treat electron motion as being restricted to a single LL

arrow. Rather intuitively such an excitation costs $\hbar\omega_C$, if it carries zero momentum $\mathbf{k} = 0$. Remarkably, Kohn's theorem ensures that this naive picture remains exact even for $\kappa \neq 0$, where many Landau levels will be mixed [115]. A quantitative analysis in this regime was performed by Kallin and Halperin, who calculated the dispersion of neutral excitations using a Bethe-Salpeter approach [116]. They found the energy of density-wave excitations at larger momenta $\mathbf{k}$ starts to depend on the interaction strength κ. The case $\kappa \ll 1$, is determined by single-particle physics. In the opposite limit where $\kappa \gg 1$ (but small enough to ensure an electron liquid) a well-defined eigenstate at energies lower than $\hbar\omega_c$ appears. Its dispersion is sketched in Fig. 3.8 **b**. The minimum in the dispersion is called a *magneto-roton*, in analogy to the roton mode that appears in superfluid helium [117]. A softening of the magneto-roton energy indicates a competing charge-density-wave order. Indeed, one finds that the momentum around the magneto-roton minimum is roughly given by the reciprocal lattice vector of a triangular lattice, indicated as a dashed line in Fig. 3.8 **b**[¶]. We remark that our conclusions also carry over to the fractional quantum Hall effect, which hosts a similar magneto-roton mode discovered by Girvin, MacDonald and Platzmann [118].

3.5.2 Optical signatures of neutral excitations

We now continue analyzing the optical signatures of this mode. To this end we first revisit the Hamiltonian of the electron-exciton system:

$$H = H_0 + H_{\text{el.}} + \int d^2r\, \lambda^{e-x}\, \hat{n}_e(\mathbf{r})[\hat{n}_X^K(\mathbf{r}) + \hat{n}_X^{K'}(\mathbf{r})], \tag{3.8}$$

where $H_{\text{el.}}$ is the electronic Hamiltonian tuned describing a correlated integer quantum Hall state which is close to a Wigner crystallization transition. In contrast to the previous sections, electrons are not classically ordered and reside in a liquid states. By inserting two identity operators we can rewrite the Hamiltonian as follows:

$$H = H_0 + H_{\text{el.}} + \int d^2r\, \lambda^{e-x} \sum_{\alpha\beta} \langle\alpha|\hat{n}_e(\mathbf{r})|\beta\rangle\, |\alpha\rangle\langle\beta|\, [\hat{n}_X^K(\mathbf{r}) + \hat{n}_X^{K'}(\mathbf{r})], \tag{3.9}$$

[¶]Indeed, one should think of a crystal as a condensate of a density-wave excitation with finite momentum $\mathbf{k} = \mathbf{G}$.

a   **Theory**
optical signatures of the magento-roton

b   **Experiment**
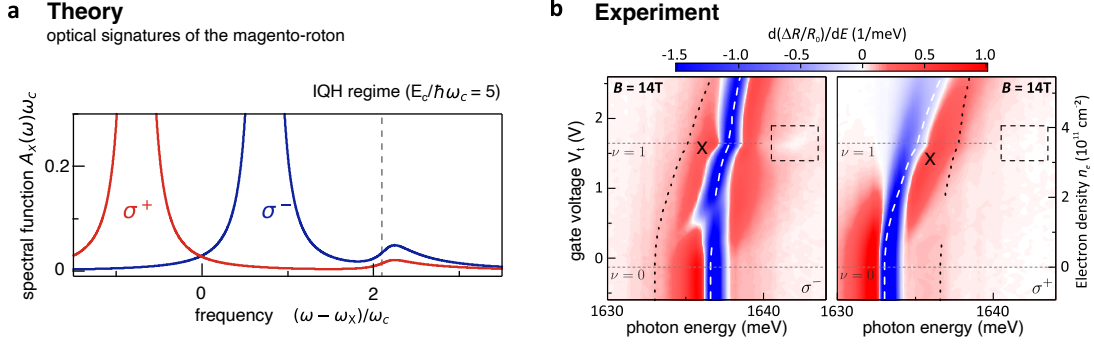
Figure 3.9: Optical sensing of a magento-roton. (**a**) Spectral function of the exciton due to the presence of a soft magneto-roton mode in a liquid IQH state, based on the self-energy given in Eq. 3.14. The qualitative behaviour is in good agreement with experimental obervations. The roton-mode leads to the appearance of a broad mode that is particularly visible in σ^- polarization and much broader than the Umklapp resonance. (**b**) Experimental observation of a satellite peak at $\nu = 1$. Top-gate-voltage dependence of the differentiated reflection contrast spectrum for $B = 14$T and $T = 80$mK in the two circular polarizations: σ^- (left) and σ^+ (right). Grey horizontal lines mark integer filling factors, while white (black) dashed (dotted) lines indicate the fitted energy of the co-polarized (cross-polarized) main exciton resonance in each map. The dashed rectangle marks the region where a higher-energy peak reappears around $\nu = 1$. At lower fillings the appearance of an Umklapp peak is also visible.

where α, β label a complete set of states, which includes the soft magnetoroton mode. Since we expect a broad continuum of density wave excitations at energies $\hbar\omega_c \gtrsim 2$, we restrict this sum to the two low-energy modes we expect to be dominant, i.e. the vacuum $|\Omega\rangle$ ($\alpha = 0$) and the magneto-plasmon $|\text{Pl.}, \mathbf{k}\rangle$ ($\alpha = \text{Pl.}, \mathbf{k}$). This yields

$$
\begin{aligned}
H &\simeq H_0 + H_{\text{el.}} + \lambda^{e-x} \int_r n_X(r) \sum_{\mathbf{q}} \langle 0|n_e(r)|\text{Pl.}, \mathbf{q}\rangle \, |0\rangle\langle\text{Pl.}, \mathbf{q}| + h.c. \\
&= H_0 + H_{\text{el.}} + \lambda^{e-x} \sum_{\mathbf{q}} n_X(-\mathbf{q}) \underbrace{\langle 0|n_e(\mathbf{q})|\text{Pl.}, \mathbf{q}\rangle}_{Z^{n_e}(\mathbf{q})} (b_{\mathbf{q}} + b^\dagger_{-\mathbf{q}}),
\end{aligned}
\tag{3.10}
$$

where $b^\dagger_{\mathbf{k}}$ creates a magneto-plasmon with momentum $\mathbf{k}$ and $Z^{n_e}(\mathbf{k})$ is known as the wave-function renormalization of the magneto-plasmon. The latter simply measures with which amplitude a density operator excites the mangeto-plasmon after acting on the vacuum $|\Omega\rangle$. Either way, it can be extracted by repeating the diagrammatic analysis by Kallin and Halperin [116], and then playing the same identity insertion trick on the density-density

response function $\chi^{n_e, n_e}(\omega, \mathbf{k})$ of the electrons [119]. This yields:

$$\chi^{n_e, n_e}(\omega, \mathbf{k}) \sim |Z^{n_e}(\mathbf{k})|^2 \frac{1}{\omega - \omega_{\text{pl.}}(\mathbf{k}) + i0^+} + \text{regular terms}, \qquad (3.11)$$

if the energy $\hbar\omega$ is taken to be sufficiently close to the energy $\hbar\omega_{\text{pl.}}(\mathbf{k})$ of the magneto-plasmon. To determine the effect of this pole on the exciton, we can proceed perturbatively to second-order in λ_{e-X}. Diagrammatically the (single-excited-plasmon) self-energy of the exciton has the following representation
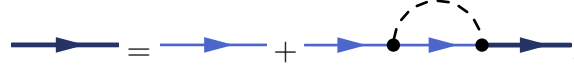
The dark/light blue line denote the dressed/bare propagator of the exciton, while the dashed line represents the propagation of an excited density-wave mode. Translating this expression into equations we find:

$$\Sigma_{X,ab}(\omega, \mathbf{k}) = i\lambda_{e-X}^2 \int \frac{d^2\mathbf{q}}{(2\pi)^2} \frac{d\omega'}{2\pi} \chi^{n_e n_e}(\mathbf{q}, \omega') G_{X,ab}^{(0)}(\omega - \omega', \mathbf{k} - \mathbf{q}). \qquad (3.12)$$

Here indices a, b refer to the two valleys and $G_{X,ab}^{(0)}$ is the unperturbed exciton Greens function. Using the same approximation as above, we obtain:

$$\Sigma_X(\omega, 0) \simeq \lambda_{e-X}^2 \int \frac{d^2\mathbf{q}}{(2\pi)^2} U_{\mathbf{q}} \operatorname{diag}\left[\frac{|Z^{n_e}(\mathbf{q})|^2}{\omega - \lambda_+(\mathbf{q}) - \omega_p(\mathbf{q}) + i0^+}, \frac{|Z^{n_e}(\mathbf{q})|^2}{\omega - \lambda_-(\mathbf{q}) - \omega_p(\mathbf{q}) + i0^+}\right] U_{\mathbf{q}}^\dagger$$

$$= \operatorname{diag}(\Sigma_X^{\sigma_+ \sigma_+}, \Sigma_X^{\sigma_- \sigma_-}),$$

$$(3.13)$$

where $U_{\mathbf{q}}$ is the unitary matrix which diagonalizes the exciton Hamiltonian of Eq. 3.6, and $\lambda_{\pm}$ are the corresponding eigenenergies. In components this yields

$$
\begin{aligned}
\Sigma_X^{\sigma_+\sigma_+} = \lambda_{e-X}^2 \int \frac{d^2\mathbf{q}}{(2\pi)^2} \Big[& \frac{\varepsilon_q + \frac{1}{2}g\mu_B B}{2\varepsilon_q} \frac{|Z^{n_e}(\mathbf{q})|^2}{\omega - \lambda_+(\mathbf{q}) - \omega_p(\mathbf{q}) + i0^+} \\
& + \frac{\varepsilon_q - \frac{1}{2}g\mu_B B}{2\varepsilon_q} \frac{|Z^{n_e}(\mathbf{q})|^2}{\omega - \lambda_-(\mathbf{q}) - \omega_p(\mathbf{q}) + i0^+} \Big], \\
\Sigma_X^{\sigma_-\sigma_-} = \lambda_{e-X}^2 \int \frac{d^2\mathbf{q}}{(2\pi)^2} \Big[& \frac{\varepsilon_q + \frac{1}{2}g\mu_B B}{2\varepsilon_q} \frac{|Z^{n_e}(\mathbf{q})|^2}{\omega - \lambda_-(\mathbf{q}) - \omega_p(\mathbf{q}) + i0^+} \\
& + \frac{\varepsilon_q - \frac{1}{2}g\mu_B B}{2\varepsilon_q} \frac{|Z^{n_e}(\mathbf{q})|^2}{\omega - \lambda_+(\mathbf{q}) - \omega_p(\mathbf{q}) + i0^+} \Big].
\end{aligned}
\tag{3.14}
$$

The fact that the exciton Greens function is also diagonal for $\mathbf{k} = 0$ simplifies the computation of the two spectral functions. By plugging in Z^{n_e} and $\omega_p(\mathbf{q})$ obtained by the Kallin and Halperin analysis, one obtains the excitonic spectral function illustrated in Fig. 3.9 **a**. Remarkably, the soft magnetorotons of the integer Quantum Hall state imprint a resonant, high energy peak in the exciton spectral function. On a first glance this *satellite peak* appears to be similar to the Umklapp resonance of the crystalline state. However, its origin must be completely distinct as the underlying electronic state is a liquid. On a physical level it appears due to a transition of the optically active exciton into a virtual state containing a magneto-roton carrying momentum $\mathbf{q}_{\text{min.}}$ and an exciton with equal and opposite momentum $-\mathbf{q}_{\text{min.}}$. $\mathbf{q}_{\text{min.}}$ denotes the momentum for which the magneto plasmon dispersion reaches its minimum. If the magneto-roton is sufficiently soft, the energy of this intermediate state is roughly determined by $\hbar\omega_p(|\mathbf{q}_{\text{min.}}|) + \hbar^2\mathbf{q}_{\text{min.}}^2/2M \simeq \hbar^2\mathbf{q}_{\text{min.}}^2/2M$. In stark contrast to the signatures of a crystal, this mode gives a finite-width resonance even at $T = 0$ for a clean system. Since the spectral function integrates to the commutation relation of the exciton operators, we can compute an approximate spectral weight of the roton-induced satellite peak. For experimental parameters, we estimate it to be a few percent.

The magneto-roton mode was also explored experimentally, in the same monolayer TMD as before, albeit in the presence of a magnetic field $B = 14\text{T}$. The differentiated reflectance spectrum in σ^- (σ^+) polarization as a function of electron doping is shown in the left (right) panel of Fig. 3.9 **b**. At low doping, we find a characteristic Umklapp peak. In σ^- polarization, it appears below the main exicton resonance due to the large Zeeman splitting of the

main resonance. At intermediate electron doping, however, Umklapp signatures are absent. An exception arises when the electrons form an incompressible state at $\nu = 1$. In this regime a broad resonance appears in the region highlighted by the dashed box. This feature is clearly visible in σ^- polarization as expected from our theoretical model. As discussed, we identify this resonance as originating from a soft magneto-roton. The observation of an additional satellite peak in experiments supports our claim that the state at integer filling is a quantum Hall state. The energy of the peak and its width are indicative of strong correlations present in the underlying quantum Hall state. In chapter 5 we will briefly return to roton modes appearing in the spin-response of exotic Mott insulators. Unlike in continuum systems, on lattice models the roton may soften fully in the vicinity of a universal critical point, since spin-ordering on a lattice is not necessarily a weak first order transition.

In conclusion, we proposed, analyzed and found novel optical signatures of spatial correlation in two dimensional semiconductors. Optically bright Umklapp-excitons appear due to scattering off the electronic density profile. The method was applied to probe Mott-Wigner states in bilayer TMDs [107], whose existence had already been suggested by indirect obervables [47]. It further proved useful in monolayer devices, where the appearance of Umklapp peaks allowed for a first observation of Wigner crystals in monolayers of two dimensional materials [113]. In stark contrast to previous studies, which focused predominantly on indirect signatures such as compressibility and transport, Umklapp scattering is directly sensitive to translational symmetry breaking in the system. This is a main advantage of our approach. Furthermore, during these efforts we realized that low-lying collective density-wave modes in electronic liquids can lead to optically bright states whose energies scale similarly to the Umklapp peaks. However, these states are distinguished by their large broadening even at zero temperatures. This allowed us to identify the presence of soft modes magneto-rotons in $\nu = 1$ quantum Hall states, which are precursors of crystallization and herald the proximity of a phase transition [113].

Moving forward, there are several interesting opportunities to advance this line of research. For one, our findings open up possibilities to study strongly correlated electrons in previously inaccessible territory. The metal to Wigner crystal transition in two-dimensions is particularly challenging to model theoretically and turns out to be subtle as phase separation is forbidden by long-range interactions [30]. This paves the way for exotic intermediate phases such as Bubbles, stripes and emergent magnetism [120, 121]. In fact, Umklapp signatures have been used very recently to analyze thermal and quantum melting transitions of crystals in this regime [122].

Another exciting direction is the investigation of emerging spin order and its relation to the crystalline structure [123]. Our calculations based on Eq. 3.3 assumed an exciton-electron coupling independent of electrons spins. Strictly speaking, this assumption is not justified since different exciton-electron scattering channels give rise to similar, but not identical, repulsive interactions [51]. While this was a good approximation for the experiments considered in this thesis, it is in principle possible to not only probe crystalline charge order but

also spin-density wave order. Probing schemes in this direction would be highly desirable, since triangular lattices are geometrically frustrated and appear naturally in Wigner crystals or can be designed in twisted bilayers. As a result, the magnetic order in these systems is debated and is potentially exotic. We have already taken first steps to explore such signatures in Ref. [124].

Once experimental sample quality improves further, more exotic states will become accessible in particularly clean devices. A prime example are fractional quantum Hall liquids and their nearby crystalline and liquid phases. While the integer quantum Hall state exists in absence of interactions, they are crucial in stabilizing its fractional counterpart. This naturally leads to the appearance of roton modes. First estimates suggest that our method is indeed sensitive to such collective excitations. Furthermore, it will also be interesting to probe collective spin-modes in two dimensional electronic systems. In combination with complementary non-optical approaches, such as the recently introduced quantum-twist-microscopes, a clear track to obtain a more complete understanding of correlated electrons in two dimensions seems to be within reach.

4

Tunable interactions via solid-state Feshbach resonances

This chapter is based on the publications

- Clemens Kuhlenkamp, Michael Knap, Marcel Wagner, Richard Schmidt and Atac Imamoglu: "Tunable Feshbach resonances and their spectral signatures in bilayer semiconductors", Physical Review Letters, 129, 037041, (2022)

- Caterina Zerba, Clemens Kuhlenkamp, Atac Imamoglu and Michael Knap: "Realizing Topological Superconductivity in Tunable Bose-Fermi Mixtures with Transition Metal Dichalcogenide Heterostructures", arXiv:2310.10720, (2023)

Text, figures and structure have been modified for this thesis.

Long-range interactions among quantum particles give rise to charge-ordered crystalline configurations. Surprisingly, even in a dilute and gaseous phase —that is when the average particle separation $l_0 \sim n^{-1/2}$ is large compared to the typical range of interactions r^*— quantum particles can nevertheless exhibit strong correlations which drastically alter the properties of the gas [125]. While strongly correlated gases sound like an oxymoron, scattering of slow quantum particles differs from our classical expectation: for attractive potentials the effective length-scale a within which slow quantum particles interact with each other is set by the inverse binding-energy E_B^{-1} of two-body complexes. This scale $a \simeq \hbar / \sqrt{2\mu_{\mathrm{red}} E_B}$ is known as the *scattering length*. Importantly, a can be entirely independent of the typical range of interactions r^* and can be the largest scale in the system $a \gg l_0, r^*$ which is due to the wave-like nature of particles which have large de-Broglie wavelengths at low temperatures. By the uncertainty principle such low momentum waves cannot probe arbitrarily short distances which explains why short-ranged potentials can then be described only by their scattering length a.

If the binding energy of a bound state is very small $E_B \to 0$, the scattering length diverges $a \to \infty$. This effect is known as a *resonance*, and signals the onset of strong correlations even in dilute gases. Such resonances rarely occur naturally as binding energies have no reason to be particularly small, but they can be reached by tuning external parameters in what are known as *Feshbach resonances* [126]. The main idea is simple: the energy of an existing bound state E_B is reduced by penalizing its formation with a tunable energy-barrier.

4.1 Feshbach Resonances in atomic gases

Feshbach resonances thus far have had their biggest impact in atomic physics and constitute one of the most important tools in ultra cold atomic gases [127, 128, 43, 129]. There, the precise control of the scattering length a^{3D} enabled the study of polaron formation, the BEC-BCS crossover including the formation of pseudo-gaps, Bose-Fermi mixtures and various aspects of Bose and Fermi Hubbard models [130, 131, 132, 133, 54, 134]. The basic principle of an atomic Feshbach resonance is illustrated in Fig. 4.1 a). Two atoms separated by large distances r experience an attractive van der Waals potential which decays as $1/r^6$. This potential hosts several bound-states independent of the atomic spin configuration.
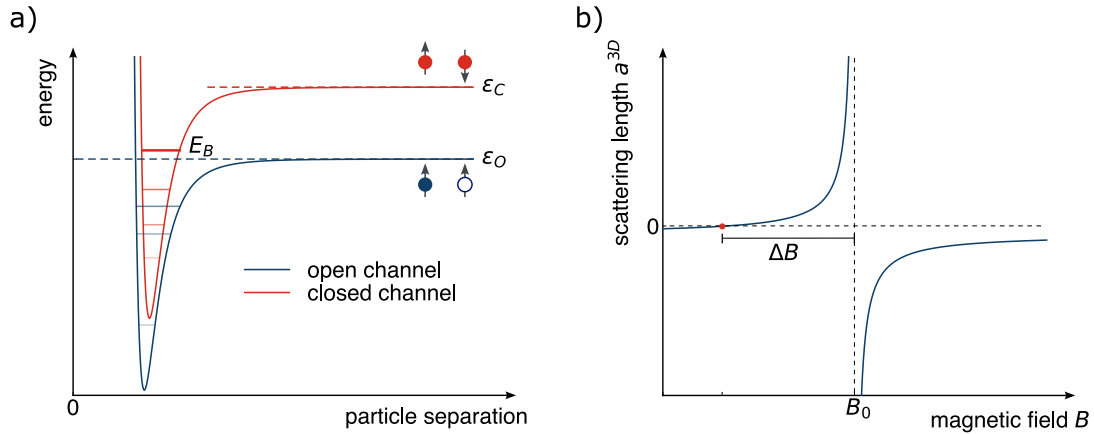
Figure 4.1: Illustration of a Feshbach resonance in atomic physics. (a) Schematic interaction potentials for two atoms in different spin configurations, neglecting hyperfine interactions. Electronic spins are denoted as arrows and the nuclear spin changes are denoted by color changes of the atoms. For large separations two atoms reside in an electronic triplet, which constitues the open (blue) channel. Energetically costly configurations form the closed (red) channel. By changing the magnetic field, the energy of the low-lying bound state (shown as a thick red line) in the closed channel can be tuned relative to the open channel. This induces a Feshbach resonance once the two channel mix due to finite hyperfine coupling. **(b)** Behaviour of the 3D scattering length across the Feshbach resonance. At the resonance position B_0 the lowest lying molecular state becomes unbound. This is reflected in a sign change of the scattering length at $a \to \infty$. The resonance width is defined as the magnetic field distance between the points where a crosses zero and diverges.

The configuration of spatially separated atoms defines their *scattering channels*. In a typical quantum gas experiment, magnetic fields are applied to polarize the electronic spins **S** of the atoms, meaning that atoms predominantly scatter off each other with electronic spins in a triplet configuration, shown by the blue potential in Fig. 4.1 a). Since this is the typical configuration of atoms, it is referred to as the *open channel* and has energy ε_O. Other spin-configurations, such as the singlet have higher energies ε_C and are referred to as *closed channels*, since they are energetically inaccessible. Nevertheless, closed channels can also host bound-states whose energies may be close to the to the open-channel threshold, these are shown in red in Fig. 4.1. The nuclear spin **I** couples only weakly to magnetic fields and is important mostly to fix symmetry properties of the wavefunction, it is indicated by the color of the atoms in Fig. 4.1a). Note that the Zeeman effect is responsible for the energy splitting between channels

$$\varepsilon_C - \varepsilon_O \sim \delta\mu\, B, \tag{4.1}$$

where $\delta\mu$ is the difference in magnetic moment. By adjusting the magnetic field, it is therefore possible to bring a closed-channel bound state into proximity of the scattering configuration of an open channel, i.e. the typical energetic configuration of the atoms in the quantum gas. Hyperfine interactions of the form $\hat{H}_{hf} \sim \alpha_{hf}\,\mathbf{S}\cdot\mathbf{I}$, couple open and closed channels. This allows atoms in the open channel to couple to molecular states in the closed channel. A naive energetic counting shows that open-channel atoms can feel an attractive reduction of energy which is roughly $\varepsilon_C - \varepsilon_O - E_B$, where E_B is the binding energy of the relevant bound state in the closed channel. Combined with Eq. 4.1, this tells us that the magnetic field can efficiently tune an attractive interaction between the two particles in the open channel. Detailed calculations, which can be found in Ref. [127, 43], reveal that the three-dimensional scattering-length for atoms in the open channel takes the simple form:

$$a^{3D}(B) = a_0\left(1 - \frac{\Delta B}{B - B_0}\right), \tag{4.2}$$

where a_0 denotes the background scattering length, B_0 labels the position of the resonance and ΔB its width. The functional behaviour of Eq. 4.2 is shown in Fig. 4.1 b).

In the rest of this chapter we establish connections between cold atomic gases and two-dimensional materials by demonstrating how interactions between electrons and excitons can be tuned by changing external electric fields, thereby realizing solid-state versions of Feshbach resonances.

4.2 SOLID-STATE FESHBACH RESONANCES

We now turn to bilayer structures of 2d materials, which were introduced as fascinating platforms for realizing exotic phases of electronic matter [135, 136]. Much of their success is driven by a new level of control, arising from twisting the two layers with respect to each other during stacking. This has lead to the discovery of unconventional superconductivity [21, 137], correlated insulators, and charge density waves [48, 22, 47] in bilayer graphene and transition metal dichalcogenides (TMDs). As discussed in chapter 2 of this thesis, semiconductors such as TMDs can also host bosons in the form of excitons, which act as rigid and mobile quantum impurities. Excitons interact with free electrons or holes to
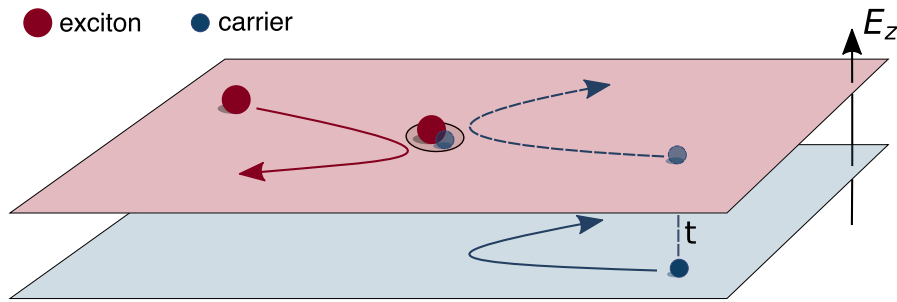
Figure 4.2: Tunable Feshbach resonances in bilayer heterostructures. Illustration of exciton-carrier scattering in a bilayer TMD. The electrostatic potential energy is different in the two layers and can be tuned by a perpendicular electric field E_z. Scattering between excitons and electrons is enhanced when the intra-layer trion energy is tuned into resonance with the energy of an electron and an exciton in seperate layers.

form charged trions. This renders bilayer TMDs as promising candidates to study complex Bose-Fermi mixtures. However, in solid state structures the molecular binding energies, and correspondingly the interaction strength among particles, are generically fixed by material properties, limiting the experimentally accessible regimes.

Motivated by the opportunities Feshbach resonances revealed in atomic quantum gas experiments, we address this challenge by introducing a solid-state analogue of a such resonances. Using the layer degree of freedom as a pseudo-spin, we demonstrate that the energy of a closed-channel bound state can be tuned with respect to scattering states in an open channel, simply by applying an external electric field E_z. The counterpart of hyperfine interactions in atomic systems, is provided by coherent inter-layer electron or hole tunneling. The emerging Feshbach molecule controls the inter-layer scattering and originates from the hybridization of exciton-electron scattering states with the intra-layer (closed channel) trion state [138]. As such, it is fundamentally distinct from the formation of inter-layer trions due to interactions determined by the material properties that are not tunable [139]. We demonstrate the impact of such Feshbach resonances on the spectrum of a single optically-injected exciton immersed in a Fermi sea of charge carriers, taking into account the radiative exciton decay. Close to the Feshbach resonance we find a striking modification of the exciton spectrum. In particular, we show that the spectral shape is sensitive to the finite range of the effective interactions relative to the Fermi wavelength.

We consider a bilayer semiconductor setup as depicted in Fig. 4.2. As we are interested in low-energy scattering, details of the underlying atomic lattice are irrelevant due to the large separation of scales between the lattice momentum and the momenta of excitons and electrons. In this regime excitons and electrons have essentially parabolic dispersions. Tunneling of electrons (or holes) between the two layers can be described by an effective average coupling constant t, which can be adjusted by incorporating tunnel barriers [47][*]. For concreteness we focus on two identical TMD layers separated by a distance d. Generically, the exciton resonances in the top and bottom layers have different energies, either due to difference in material properties or strain, enabling layer-selective exciton creation. Furthermore, hybridization between inter- and intra-layer excitons is small, due to the sizable difference in binding energies. This allows us to focus only on intra-layer excitons [†]. For simplicity we assume that excitons are injected optically and are present only in the top layer. The system is then described by the effective Hamiltonian

$$\hat{H} = \sum_{\mathbf{k}} x_{\mathbf{k}}^{\dagger} \frac{k^2}{2M} x_{\mathbf{k}} + \begin{pmatrix} c_{\mathbf{k},T}^{\dagger} \\ c_{\mathbf{k},B}^{\dagger} \end{pmatrix} \begin{pmatrix} \xi_{\mathbf{k}} + \Delta & t \\ t & \xi_{\mathbf{k}} \end{pmatrix} \begin{pmatrix} c_{\mathbf{k},T} \\ c_{\mathbf{k},B} \end{pmatrix} + \frac{U}{V} \sum_{kk'q} c_{\mathbf{k},T}^{\dagger} c_{\mathbf{k}+\mathbf{q},T} x_{\mathbf{k}'}^{\dagger} x_{\mathbf{k}'-\mathbf{q}}, \quad (4.3)$$

where $x_{\mathbf{k}}^{\dagger}$ creates an exciton of mass M in the top layer, and $c_{\mathbf{k},T}^{\dagger}$ and $c_{\mathbf{k},B}^{\dagger}$ create fermions of mass m in the top and bottom layer, respectively.

From now on we refer to itinerant charges as electrons, although all conclusions apply equally to holes. We omit the valley and spin degree of freedom and assume that electrons and excitons reside in different valleys, since only this scattering channel will be resonantly enhanced. As the exciton's Bohr radius is small, excitons and electrons experience sizable attractive contact interactions U, only when both particles are in the same layer and opposite valleys. We also neglect the composite nature of the exciton and treat it as a structureless

---

[*]The phenomenological treatment of the tunnel coupling t can break down for specific stackings: if the layer separation d is small, pronounced moire potentials with spatially modulated tunneling will form. In this case our phenomenological description is useful only for Fermi wavelengths much larger than the lattice constant of the super lattice.

[†]Large electric fields could overcome the energy difference resulting in sizable hybridization with inter-layer excitons, which would then contribute to inter-layer scattering of electrons and excitons. Here are we are interested in smaller fields on the order of the trion binding energy where these processes are suppressed.

boson [51]. The potential energy difference $\Delta = qdE_z$ between the two layers, can be tuned by changing E_z, as illustrated in Fig. 4.2. We consider the scenario where Δ is chosen such that electrons reside predominantly in the bottom layer.

4.4 Feshbach resonance in exciton-electron scattering

To understand scattering properties in such a heterostructure, we focus on the two-particle subspace of the system. In the center of mass frame, Eq. 4.3 can then be expressed in first quantization as:

$$
\begin{aligned}
\hat{H}_{2\,\text{body}} &= \hat{H}_0 + \hat{U} \\
&= \begin{pmatrix} -\frac{\nabla_{\mathbf{R}}^2}{2m_{\text{tot}}} - \frac{\nabla_{\mathbf{r}}^2}{2\mu_{\text{red}}} + \Delta & t \\ t & -\frac{\nabla_{\mathbf{R}}^2}{2m_{\text{tot}}} - \frac{\nabla_{\mathbf{r}}^2}{2\mu_{\text{red}}} \end{pmatrix} + U \begin{pmatrix} \delta^2(\mathbf{r}) & 0 \\ 0 & 0 \end{pmatrix},
\end{aligned}
\tag{4.4}
$$

where $\mu_{\text{red}} = 1/(m^{-1} + M^{-1})$ and $m_{\text{tot}} = m + M$ are the reduced mass and the total mass respectively. The wave function carries the layer degree of freedom and the part describing the relative motion can be expressed as $\psi(\mathbf{r}) = (\psi_T(\mathbf{r}), \psi_B(\mathbf{r}))^T/\sqrt{2}$. As in the atomic case, asymptotic eigenstates with large spatial separation between the two particles define the open and closed channel. We consider E_z for which $\Delta \simeq |E_B^0|$, where E_B^0 is the binding energy of the intra-layer trion. Although both channels are hybridized between the layers, only the open channel is energetically accessible and electrons reside predominantly in the bottom layer (Fig. 4.3). The scattering threshold for the open (ε_O) and closed (ε_C) channel is $\varepsilon_{O,C} = \Delta/2 \mp \sqrt{t^2 + \Delta^2/4}$.

The outgoing scattering states $|\psi_\alpha^+\rangle$, in channel α with energy E can be found as solutions of the Lippmann-Schwinger equation:

$$
|\psi_\alpha^+\rangle = |\varphi_\alpha\rangle + \frac{1}{E - \hat{H}_0 + i0^+} \hat{U} |\psi_\alpha^+\rangle,
\tag{4.5}
$$

where $\langle\mathbf{r}|\varphi_\alpha\rangle \sim e^{ikx}$ is an incoming plane wave [129, 140, 119]. We can reformulate the problem by introducing the T-matrix $\hat{T}^R|\varphi_\alpha\rangle = \hat{U}|\psi_\alpha^+\rangle$, which connects the incoming plane waves with the full outgoing scattering state. Eq. 4.5 translates to an equation for the
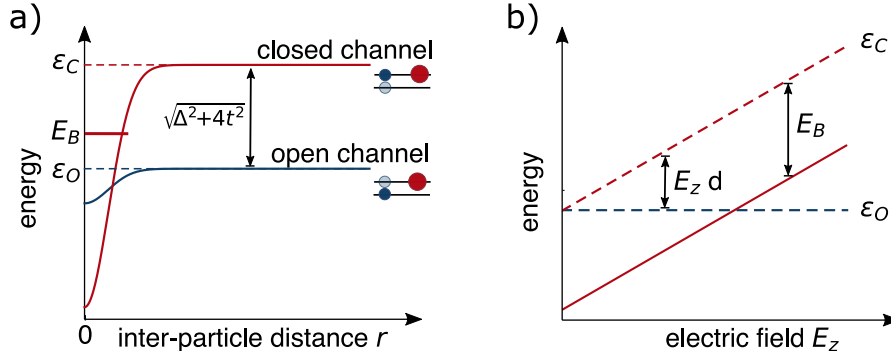
Figure 4.3: Illustration of scattering channels. (a) Inter-particle potential for an exciton and an electron prepared in the open (blue) or closed (red) channel. Tunnel coupling imprints the closed channel attraction also on the open channel. **(b)** Threshold energies of the open and closed channel ε_O and ε_C, as the electric field is varied. The bare closed channel bound-state has a binding energy of E_B and is denoted by the red line. This bound state can be brought into resonance with ε_O for an appropriately chosen electric field.

off-shell T-matrix $\hat{T}^R(E)$:

$$\hat{T}^R(E) = \hat{U} + \hat{U}\left(E - \hat{H}_0 + i0^+\right)^{-1} \hat{T}^R(E). \tag{4.6}$$

We solve Eq. 4.6 analytically in a plane-wave basis which diagonalizes $\hat{H}_0$:

$$\hat{T}^R(E, \mathbf{k}) = [1_{2\times2} - \hat{U} \cdot \Pi^R(E, \mathbf{k})]^{-1} \cdot \hat{U}$$

$$\Pi^R_{\alpha\beta}(E, \mathbf{k}) = \int \frac{d^2q}{(2\pi)^2} \frac{\delta_{\alpha\beta}}{E - \frac{q^2}{2\mu_{\text{red}}} - \frac{k^2}{2m_{\text{tot}}} - \varepsilon_\alpha + i0^+}, \tag{4.7}$$

where E is the scattering energy, and $\mathbf{k}$ is the total incoming momentum. The 2×2 matrix structure of $\hat{T}^R(E, \mathbf{k})$, and $\hat{U}$, due to the two channels, is implicitly assumed.

Scattering can be resonantly enhanced if E_z is tuned such that the closed channel bound state is in proximity of the open channel threshold ε_O, see Fig. 4.3 (b) for an illustration. Similar to cold atomic systems, we are interested in two-particle collisions with small incoming momenta. In this case, scattering is accurately described by a finite-range expansion, which is performed by expanding the denominator of the T-matrix in powers of $E - \varepsilon_O$. In

two dimensions the finite range expansion of the on-shell T-matrix takes the universal form:

$$T^R(\mathbf{k}^2/2\mu_{\mathrm{red}}, 0)^{-1} = \frac{\mu_{\mathrm{red}}}{2\pi}\left(i\pi - \ln(\mathbf{k}^2 a^2) + \frac{r_0 \mathbf{k}^2}{2} + \mathcal{O}(\mathbf{k}^3)\right),$$ (4.8)

which is characterized by the scattering length a and effective range r_0 [141, 142]. We relate this expansion to our effective description by integrating Eq. 4.7 and matching the open channel scattering amplitude $T_{OO}^R(\mathbf{k}^2/2\mu_{\mathrm{red}}, 0)$ to Eq. 4.8. This way we obtain the open channel scattering length a_O and effective range r_0:

$$a_O = a \exp\left\{-\frac{1}{2}\left(\frac{\Delta}{2t} + \sqrt{1 + \frac{\Delta^2}{4t^2}}\right)^2 \ln\frac{-E_B^0}{\sqrt{4t^2 + \Delta^2}}\right\},$$

$$r_0 = \frac{1}{2\mu_{\mathrm{red}}}\frac{(\Delta/2 + \sqrt{t^2 + \Delta^2/4})^2}{t^2\sqrt{t^2 + \Delta^2/4}},$$ (4.9)

where $a = 1/\sqrt{2\mu E_B^0}$ is the scattering length of the closed channel in absence of tunnel coupling. Analyzing Eq. 4.7–4.9 we find that the open channel T-matrix has a pole at energies below the scattering threshold ε_O. This is the signature of a Feshbach molecule which forms in inter-layer scattering [119]. Eq. 4.8 demonstrates that the energy of the molecule depends on both the scattering length a_O and range r_0. We plot the energy of the Feshbach molecule as a function of detuning in Fig. 4.4 for three different t. As the detuning becomes large and positive, the scattering length starts to diverge while the molecular energy approaches the scattering threshold. For large detunings the binding energy is then approximately given by $1/2\mu_{\mathrm{red}}a_O^2$. In the case $E_B^0, \Delta \gg t$ we obtain simple expressions for the binding energy of the Feshbach molecule E_B and the effective range close to resonance, which read

$$E_B \simeq E_B^0\frac{1}{e^{-2}}\left|\frac{\Delta}{E_B^0}\right|^{-\frac{\Delta^2}{t^2}}, \qquad r_0 \simeq \frac{1}{\mu_{\mathrm{red}}}\frac{\Delta}{t^2}.$$ (4.10)

This demonstrates the power of a Feshbach resonance: complete control over the energy of the Feshbach molecule can be achieved simply by changing E_z. Thus the system can be electrically tuned to arbitrarily large scattering lengths [143]. [‡] We remark that while we discuss structures consisting of two identical TMD layers, the emerging Feshbach physics

---

[‡] More importantly, for any given electron density, it is possible to choose E_z such that $k_F a_O \sim 1$, which yields the strong correlation regime.
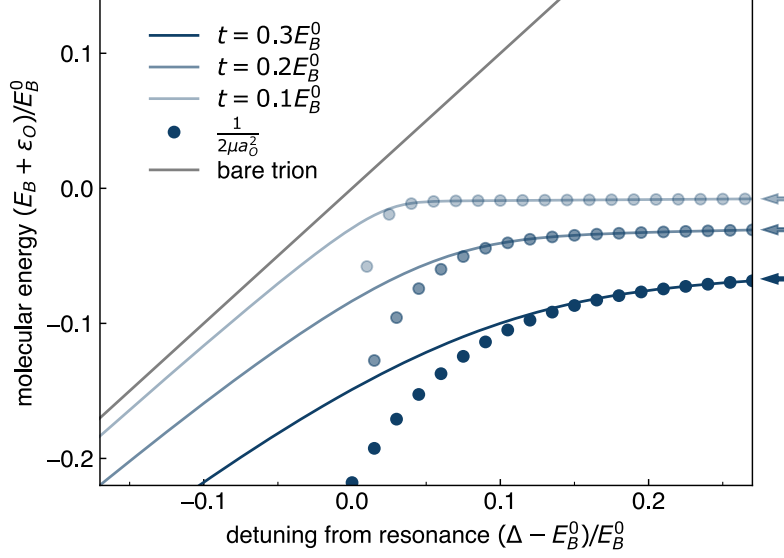
Figure 4.4: Feshbach molecule binding energy. Molecular energy as a function of electric field (solid blue lines). We have assumed an exciton mass of $M = 2m$ and contact interactions between the exciton and electron. In two dimensions, and in the absence of inter-layer repulsion, a bound state exists for all values of Δ. When the size of the molecule exceeds the range of the interactions, the scattering length alone determines the binding energy (blue dots). For large positive detunings the molecular energy approaches the open channel threshold ε_O (arrows), implying that the binding energy E_B goes asymptotically to zero. For large negative detunings the binding energy approaches the energy of the bare intra-layer trion.

is universal. By choosing different TMD's and spacer materials one can vary the tunnel coupling and therefore the resonance width r_0. While the binding energy of the Feshbach molecule changes exponentially, the effective range r_0 depends only linearly on E_z. We find that weakly coupled layers lead to large values of r_0, and the resulting physics is reminiscent of narrow Feshbach resonances in atomic systems appearing for small hyperfine coupling. However, the exponential behaviour is completely distinct from that of three dimensional resonances appearing in atomic systems. There, the dependence on the tuning parameter is algebraic, as can be seen in Eq. 4.2. This difference persists, even in the presence of repulsive background scattering, as discussed in appendix A, and can be attributed to the purely two dimensional geometry in the system.

Close to a Feshbach resonance, when $\Delta \simeq E_T^0$, scattering is dominated by the inter-layer trion bound state. We can thus consider an effective model for the T-Matrix where scattering between exciton and top layer electrons is mediated by a virtual molecule. In this limit, we expect our system to be described by an effective Hamiltonian containing holes $\hat{c}$, trions (molecules) $\hat{m}$, and excitons $\hat{x}$:

$$\hat{H} = \sum_{\mathbf{k}} \frac{k^2}{2m} \hat{c}_{\mathbf{k}}^{\dagger} \hat{c}_{\mathbf{k}} + \sum_{\mathbf{k}} \left(\frac{k^2}{2m + 2M} + \Delta \right) \hat{m}_{\mathbf{k}}^{\dagger} \hat{m}_{\mathbf{k}} + \sum_{\mathbf{k}} \frac{k^2}{2M} \hat{x}_{\mathbf{k}}^{\dagger} \hat{x}_{\mathbf{k}} + g \sum_{\mathbf{k},\mathbf{k}'} [\hat{m}_{\mathbf{k}}^{\dagger} \hat{c}_{\mathbf{k}'} \hat{x}_{\mathbf{k}-\mathbf{k}'} + \text{h.c.}],$$

(4.11)

where the first three terms describe the energies of propagating charges in the open channel, the closed-channel molecules and the excitons. All interaction effects are encoded in the last term, and are quantified by the bare molecule-exciton-hole coupling g.

To understand how these coefficients relate to those of the full Feshbach problem, we match the off-shell T-matrices. To second order in g we find that Eq. 4.11 gives rise to:

$$T^E(\omega) \sim \frac{g^2}{\omega - E_T^0 + \Delta + i\varepsilon},$$

(4.12)

which has a pole at the molecular energy. For a consistent description we require this pole to be the same as the one encountered in the microscopic model for exciton-charge scattering, which close to resonance yields

$$\frac{2\pi E_T^0}{\mu_{\text{red}}(\omega - E_T^0 + \Delta + i\varepsilon)}.$$

(4.13)

This relation is obtained by expanding the logarithm of the two-dimensional T-matrix. The tunneling process is added perturbatively by introducing a vertex with tunneling strength t and a propagator that describes tunneling of the upper layer charge carrier to the bottom layer. Then, close to resonance, the tunneling process to the bottom layer and back contributes a factor $\frac{t^2}{\Delta^2}$. The T-matrix is thus $\sim \frac{2\pi E_T^0}{\mu_{\text{red}}\Delta^2(\omega - E_T^0 + \Delta + i\varepsilon)} t^2$. Comparing the two expres-

sions yields a simple matching condition:

$$g = \sqrt{\frac{2\pi}{\mu_{\mathrm{red}} E_T^0}} t, \qquad (4.14)$$

relating the scattering matrix in the microscopic and effective model. This makes the narrow resonance limit $t \to 0$ explicit. In this case the coupling g vanishes and molecules, charges and excitons are completely decoupled.

4.6 Strongly coupling a single Boson to the Fermi sea
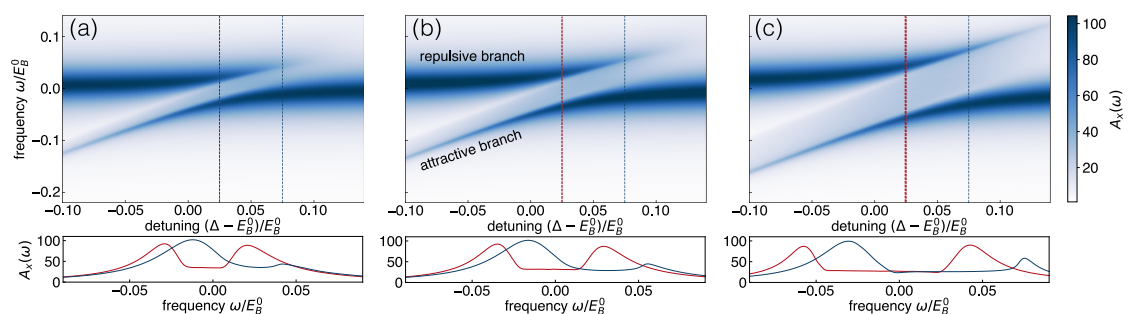
Figure 4.5: Exciton spectra across the Feshbach resonance. The spectral function of a dissipative exciton as a function of the bias Δ, computed within a T-matrix approximation. The Fermi energy E_F is increasing from left to right: **(a)** $E_F = E_B^0/30$, **(b)** $E_F = E_B^0/20$, **(c)** $E_F = E_B^0/10$. All spectra are computed for weak channel coupling $t = 0.15 E_B^0$. The splitting of the repulsive and attractive branch depends on E_F, as highlighted in the line cuts of the spectra for two different Δ in the lower panels. For large E_F, finite range corrections become increasingly important and the repulsive branch is stabilized and regains oscillator strength. Motivated by experiments [144, 145], the exciton is assumed to have a radiative lifetime of $\Gamma = E_B^0/30$.

Resonantly enhanced two-particle scattering affects correlations in electron-exciton mixtures. We consider a low concentration of excitons injected into a Fermi sea of electrons in the open channel. The excitons in such a system are mobile impurities and form collective excitations known as Fermi polarons [57, 146, 106, 147, 55]. Here we analyze the polaron spectrum as E_z is tuned over the Feshbach resonance.

Our previous discussions focused on two-body scattering with small but finite momentum,

for which the exciton is long-lived and the scattering matrix is essentially unitary[§]. Here, we focus on optically excited $\mathbf{k} = 0$ excitons. In this regime excitons couple to the radiation field, which allows them to decay via electron-hole recombination via emission of an optical photon. As this decay process is essentially memory-less, it can be described by a Lindblad master equation

$$\dot{\rho}(t) = -i[\hat{H},\rho] + \sum_{\mathbf{k}} L_{\mathbf{k}}\rho L_{\mathbf{k}}^{\dagger} - \frac{1}{2}\{L_{\mathbf{k}}^{\dagger}L_{\mathbf{k}},\rho\},$$
$$L_{\mathbf{k}} = \sqrt{2\Gamma(\mathbf{k})}\, x_{\mathbf{k}}\,, \tag{4.15}$$

where $\Gamma(\mathbf{k})$ is the decay rate of the exciton and $L_{\mathbf{k}}$ denotes the quantum jump operator. In the presence of a Fermi sea Eq. 4.15 constitutes a complex many-body system, which can not be solved exactly. However, it was found that key properties can already be inferred purely from the scattering properties of the system [148, 149] and that T-matrix approximations provide an accurate description of the ground and excited states of mobile impurities [60, 150, 151, 152, 153, 154, 155, 142, 156].

For our heterostructure setting we develop a T-matrix approximation to include dissipation as well as finite-range corrections from the Feshbach resonance:

$$\hat{T}^{R}(E, \mathbf{k}) = [1_{2\times2} - \hat{U} \cdot \Pi^{R}(E, \mathbf{k})]^{-1} \cdot \hat{U}$$
$$\Pi_{\alpha\beta}^{R}(E, \mathbf{k}) = \int\limits_{|\mathbf{q}'|>k_F} \frac{d^2q'}{(2\pi)^2} \frac{\delta_{\alpha\beta}}{E - \xi_{\mathbf{q}'} - \varepsilon_{\alpha} - \frac{(\mathbf{k}-\mathbf{q}')^2}{2M} + i\Gamma(\mathbf{k}-\mathbf{q}')}. \tag{4.16}$$

Details on the calculation can be found in appendix A. Compared to Eq. 4.7, the momentum of the electron in the open channel is now restricted to lie above the Fermi surface due to Pauli blocking by the Fermi sea. Exciton recombination results in an imaginary part $i\Gamma(\mathbf{k})$ of the exciton energy [158, 159]. Using this T-matrix, we then determine the self-energy of the exciton as a function of frequency ω:

$$\Sigma^{R}(\omega, \mathbf{k}) = \int\limits_{|\mathbf{q}|<k_F} \frac{d^2q}{(2\pi)^2} T_{OO}^{R}(\omega + \xi_{\mathbf{q}}, \mathbf{k} + \mathbf{q}). \tag{4.17}$$

This equation originates from the creation of a particle-hole pair in the open channel, with

---

[§]Finite momentum excitons are long-lived due to the steep light-cone, which renders only $\mathbf{k} = 0$ excitons optically active.

hole momentum $|\mathbf{q}| < k_F$. The spectral function of the exciton then reads

$$A_x(\omega, \mathbf{k}) = -2\mathrm{Im}\left[\frac{1}{\omega - \mathbf{k}^2/2M - \Sigma^R(\omega, \mathbf{k}) + i\Gamma(\mathbf{k})}\right]. \qquad (4.18)$$

As the master equation fulfills fluctuation-dissipation relations and we have treated dissipation exactly, the resulting spectral function respects the sum rule $\int \frac{d\omega}{2\pi} A_x(\omega, \mathbf{k}) = \langle[x_{\mathbf{k}}, x_{\mathbf{k}}^\dagger]\rangle = 1$.

We compute the spectrum as a function of detuning, by integrating Eq. 4.18 numerically. We show the resulting exciton spectra in Fig. 4.5 for three different Fermi energies (a)-(c). They are characterized by the formation of an attractive branch, with maxima at negative frequencies; and a repulsive branch, with maxima at positive frequencies. For small Fermi energies (Fig. 4.5(a)) the two resonances approach the Feshbach molecule and bare exciton energy respectively: the spectrum can be understood in terms of the formation of a Fermi polaron and is highly asymmetric. We observe that the repulsive polaron abruptly transfers spectral weight to the attractive branch as the Feshbach molecule becomes weakly bound and blue-shifts in energy.

With increasing carrier density, the maximal splitting between the repulsive and attractive branch grows (Fig. 4.5(b)). Surprisingly, we find that the repulsive polaron branch is stabilized with growing electron densities, as seen in Fig. 4.5(c), despite the possible relaxation channel via excitations in the Fermi sea. This change in spectral shape cannot be explained assuming contact interactions, but rather arises from significant finite range corrections [160, 161]. Since the average scattering process involves momenta on the order of k_F, the non-logarithmic terms in Eq. 4.8 become successively more important at high densities and strongly renormalize the spectrum. In our setup Feshbach resonances are rather broad, which leads to characteristic spectral asymmetries due to the strong coupling to a continuum of scattering states. For Feshbach resonances based on polaritons on the other hand, this coupling is typically very weak due to the steep polariton dispersion, which can obscure the relevant scattering physics [162]. As the spectral function of the exciton is directly accessible in reflection measurements, the features we identified provide particularly clear experimental signatures of strong correlations, which we study in the next section.

This section is based on the publication

- Ido Schwartz, Yuya Shimazaki, Clemens Kuhlenkamp, Kenji Watanabe, Takashi Taniguchi, Martin Kroner and Ataç Imamoğlu: "Observation of electrically tunable Feshbach resonances in twisted bilayer semiconductors", Science 374, 6565, pp. 336-340, (2021)

Text, figures and structure have been modified for this thesis.
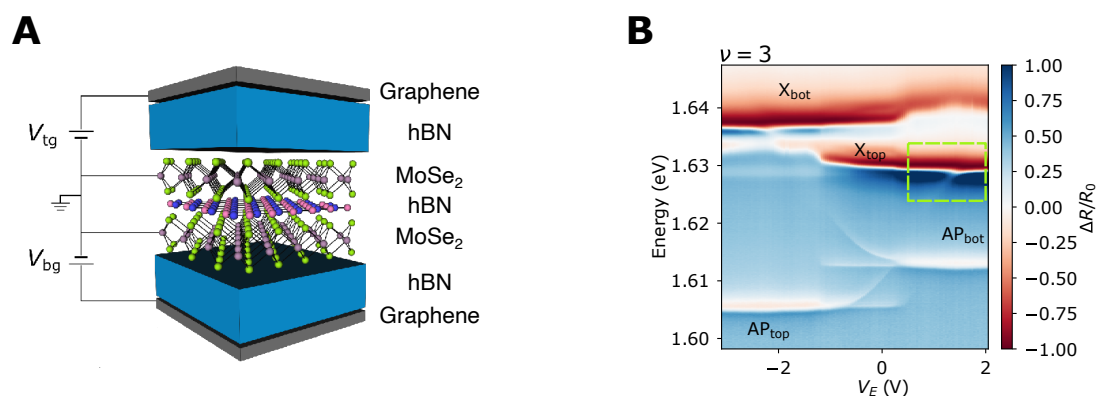
Figure 4.6: Optical properties of a bilayer TMD device. (A) Schematic depiction of the experimental setup consisting of two MoSe$_2$ layers separated by a single layer of hBN. **(B)** V_E dependent differential reflectance spectra at a fixed chemical potential for $\nu = 3$. A Feshbach resonance is reached when the energy of a top-layer trion is in resonance with a bottom layer hole, as highlighted by the dashed green box.

Here we demonstrate a tunable Feshbach resonance in a homobilayer MoSe$_2$/hBN/MoSe$_2$ heterostructure, which provides the experimental basis for tunable interactions between bosonic (exciton or polariton) and fermionic (electron or hole) particles. The experimental setup is illustrated in Fig. 4.6A, and is aligned with the general theoretical model introduced in the previous sections. The hBN spacer suppresses the inter-layer hole tunneling. Top and bottom gate voltages V_{tg} and V_{bg} allow us to adjust the filling and electric field independently, which is important as the latter tunes the potential energy of the holes depending on

their layer-configuration. We use V_{E} and V_{μ} to denote linear combinations of V_{tg} and V_{bg} that results in a minimal change to E_z and the chemical potential μ. The main difference to the theoretical model is a finite twist-angle between the two MoSe$_2$ layers, which introduces a weak moire superlattice and leads to a striking filling factor dependence of the many-body system: for unity filling of the moire superlattice ($\nu = 1$) we observe the Mott-like correlated insulator states in the top or bottom layers, as evidenced by the observation of an umklapp resonance as discussed in chapter 3. Nevertheless, for high fillings $\nu > 1$, excess holes in the system are tunnel-coupled and occupy layer hybridized sites in the moire lattice. In this limit signatures of the Feshbach resonance appear, which we study via the strong electric field (E_z) and hole density dependence of the exciton spectrum [57, 106], which demonstrates a strong-coupling regime of the Fermi polaron.

We show a wide range of the V_{E} dependent $\Delta R/R_0$ spectra at $\nu = 3$ in Figure 4.6B. The excitation spectrum clearly shows the neutral exciton resonances X_{top} and X_{bot} of the top and bottom layers. As V_{E} is increased from $-2\mathrm{V}$ to $2\mathrm{V}$, doped holes in the system transferred from top to bottom layer. The shift of holes to the bottom (top) layer is evidenced by the disappearance of the X_{bot} (X_{top}) exciton resonance as the bottom (top) layer is charge doped and the exciton starts to be modified by the presence of fermions in the same layer. At the same time this also leads to the formation of an attractive polaron AP_{bot} (AP_{top}) in the bottom (top) layer at lower energy. A more interesting effect occurs once the molecular energy of a top layer trion becomes resonant with a hole in the bottom layer, which is marked by the green box in Fig. 4.6B. For $V_E \geq 1.3\,\mathrm{V}$, the oscillator strength of the V_E-dependent top layer AP transition starts to increase and exhibits a highly asymmetric anti-crossing with the top-layer exciton transition at $V_E = 1.4\,\mathrm{V}$. The corresponding avoided crossing between the bottom layer AP and the bottom layer exciton transitions is observed at $V_E = -2.1\,\mathrm{V}$. These are the Feshbach regions, which we will focus on in the following. There the X_{top} (X_{bot}) resonance is modified, despite the top (bottom) layer being almost completely void of holes. The increasing oscillator strength of the top layer AP originates from intra-layer trions resonantly coupled to a continuum of inter-layer exciton-hole states and identified as a Feshbach molecule [127].

For finite doping the Feshbach resonance allows us to strongly couple the exciton to a Fermi sea. We demonstrate this experimentally in Figure 4.7, where we show the derivative of $\Delta R/R_0$ with respect to energy in the spectral region highlighted with the green dashed box
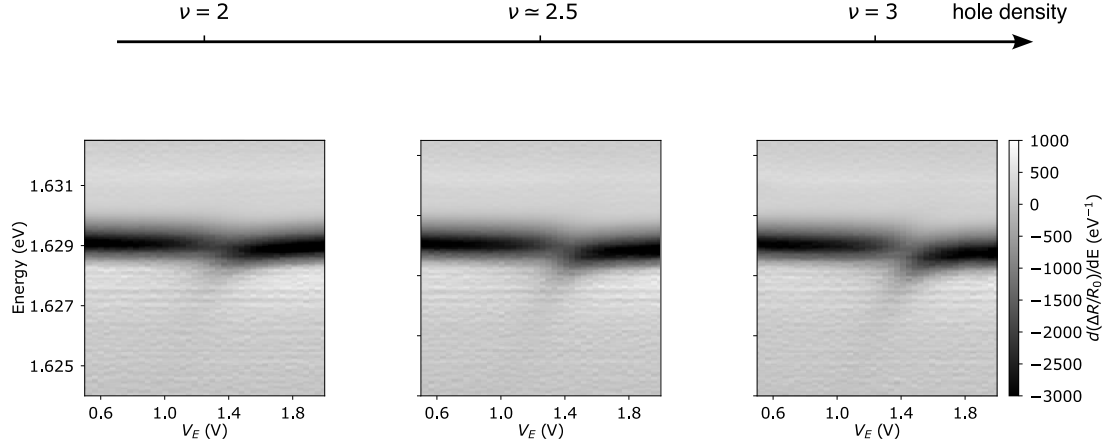
Figure 4.7: Signatures of the polaron spectrum close to the Feshbach resonance. Evolution of the V_E dependent differential reflectance spectrum differentiated with respect to energy E, for hole-densities $\nu = 2$, $\nu \simeq 2.5$ and $\nu = 3$. The spectrum around the top-layer exciton resonance X_top is visibly asymmetric even though holes predominantly reside in the opposite layer. For larger Fermi surfaces the effect is more pronounced, as expected from Fermi polaron formation with a Feshbach molecule.

in Fig. 4.6B. For small densities $\nu \simeq 2$ the splitting between the exciton and the molecular branch is much smaller than the coherent hole tunnel rate, as expected for a Feshbach resonance. As the filling ν is increased from 2 to 3, we find that the splitting grows: this enhancement is consistent with the fact that the oscillator strength of the Feshbach attractive polaron resonance as well as the splitting between the attractive and repulsive resonances scale with the density of holes. As such, the nature of the anti-crossing is strikingly different from that of a simple avoided crossing: the physics underlying the excited state splitting is the tunnel coupling of a single molecular (trion) state to a continuum of exciton-hole scattering states. The observed strongly asymmetric anti-crossing in the optically excited state is therefore a purely many-body effect and is due to the formation of attractive and repulsive polarons associated with the emerging inter-layer Feshbach molecule. Remarkably, the observed hole density dependence of the avoided crossing is in good agreement with the theoretically predicted density-dependence of the Fermi-polaron.

We also point out that our theoretical model is easily adapted to explain off-resonant features in the full range of V_E. As before we perform a T-matrix approximation, but also allow for a large population of holes in the same layer as the exciton. The resulting spectral

functions for a Fermi energy of 1 meV and a radiative decay rate of $\Gamma = 1.5$ meV are shown in Fig. 4.8. Even though we do not take into account interference effects arising from the device geometry (which lead to the dispersive line shapes observed experimentally), the theoretical model still captures the most important features shown in Fig. 4.6B. The exciton
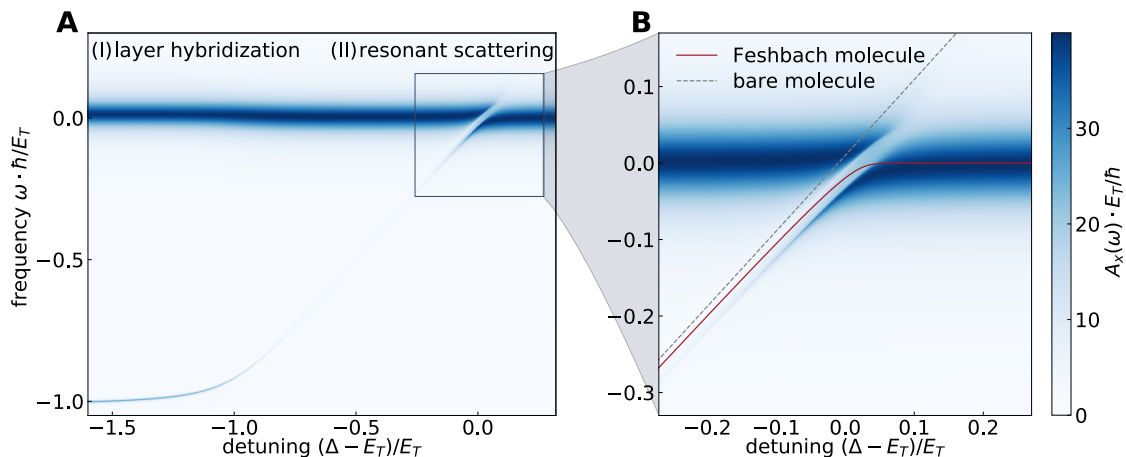
Figure 4.8: Theory of exciton spectra across the Feshbach resonance. Spectral functions of a single exciton coupled to a Fermi sea of holes, as a function of detuning $\Delta = edE_z$. (**A**) shows a full electric field scan. Two regions are distinguished: (I) For weak electric fields, observed shifts arise from hybridization of holes between the two layers. (II) Once $\Delta \simeq E_T$, scattering is strongly enhanced due to the formation of a weakly bound inter-layer molecule. Remarkably, in this regime the holes are strongly pinned to the opposite layer of the exciton. (**B**) shows a zoom-in on the resonant region, where the asymmetric transfer of spectral weight between the attractive and repulsive polaron is clearly visible. The bare trion energy in the absence of tunnel coupling, and the energy of the Feshbach molecule are shown as dashed (grey) and solid (red) lines.

spectrum is characterized by two distinct regimes:

1. For $eE_zd \simeq 0$ we find an attractive polaron branch originating close to the intralayer trion energy $|E_T| \gg E_F$, with small oscillator strength. In the experiment this is the AP_{top} branch that is associated with holes originally at the MM sites of the moiré lattice. As V_E is increased, this branch continues to blue shift while losing oscillator strength. This is a consequence of the fact that as V_E is increased, the probability of finding a lowest energy MM site hole in the top layer is decreased. Since the hole in the initial state of the optical transition is predominantly in the bottom layer, the photon energy required to create a top layer AP increases linearly with V_E. Naturally,

67

for large V_E the probability to find the hole in the top layer MM site is small, which is confirmed experimentally by the very faint AP_{top} signal.

2. Once $eE_z d \simeq |E_B|$ the molecular bound state is close to the continuum of scattering states at which point the system features resonantly enhanced interactions between the exciton and the Fermi sea. Here, the exciton can efficiently scatter particle-hole pairs, leading to an abrupt loss of the excitonic (repulsive polaron) branch, as clearly seen in Fig. 4.8B.

Although our modeling given by Eq. 4.4 and Eq. 4.17 neglects complex features of the experiment such as the underlying moiré potential, the fact that inter-layer hole-tunneling is only possible around the MM sites of the moiré lattice, long-range Coulomb interactions and mass renormalization, we are able to obtain very good qualitative agreement with the experimental observations. This demonstrates that the underlying physics can be effectively described by a simple model of a rather broad two-dimensional Feshbach resonance. Our observation therefore provides unequivocal evidence for a 2D Feshbach resonance [162] and the presence of attractive and repulsive polaron branches associated with the emerging inter-layer Feshbach molecule.

4.8 Conclusions and Outlook

In this chapter we have carried atomic Feshbach resonances over to solid state systems. This establishes important connections between distinct experimental platforms, whose typical energy scales are separated by several orders of magnitude. Further, expressed in terms of electric field tunable layer pseudo-spins of electrons, the condensed matter set-up makes the Feshbach mechanism of introducing an energy barrier for bound-state formation particularly evident. Since excitons and electrons in these setups are naturally and strongly confined to two dimensions, this allowed us to study the previously unexplored regime of perfectly two dimensional Feshbach resonances. More importantly, however, solid-state Feshbach resonances enable tunable, strong correlations in Bose-Fermi systems independent of their total density; which posed a major obstacle in their experimental realization. As a proof of principle, we have shown that the formation of Fermi Polarons can be controllably

studied via the Feshbach resonance. We observed experimentally and theoretically that the Fermi polaron exhibits a highly asymmetric and density-dependent spectrum in the strongly interacting regime. This can be understood as a realization of a maximally imbalanced Bose-Fermi mixture. While such systems have also been studied in cold atomic gases [55], solids can reach much lower temperatures on the order of few mK, which corresponds to remarkably low ratios $T/T_F \ll 0.1$, which have remained inaccessible until now.

In the future, several directions will be particularly interesting to explore. For one, our observations open the exciting direction to increase the Boson density away from the Polaron limit which can enable a controlled study of the rich phase diagram of Bose Fermi mixtures. We have already made first steps to extend our setup to finite exciton densities, where excitations of an excitonic Bose gas mediate superconductivity in a Fermi sea [163, 164]. Since the bound state exists only for excitons and electrons with different spin/valley degree-of-freedom, the Feshbach-resonance allows for spin selective interaction control which drives exotic pairing channels, where Cooper pairs can carry finite angular momentum. Strikingly, such systems typically break time-reversal symmetry and can host elusive Majorana fermions.

We want to highlight that Feshbach resonances can also form in different scattering channels than the one considered here, i.e. an electron and an inter-layer exciton in resonance with an intra-layer bound state. This could prove to be useful in the context of long-lived indirect exciton condensates [165]. This is possible as inter- and intra-layer excitons have been shown to hybridize due to tunneling, and the energy of the former can be tuned electrically [47, 166].

Lastly, our work generates the opportunity to study few-body physics in two dimensional semiconductors. The tunable scattering length can be used to explore exotic multi-particle bound states, where a single electron binds multiple excitons [167, 168]. While we specifically considered resonant scattering between excitons and electrons, Feshbach physics in 2D materials could be a generic phenomenon that may also be relevant for understanding purely electronic processes [169].

To believe or not to believe.

Xiao Gang Wen

5

Stabilizing Chiral Spin Liquids in twisted TMDs

This chapter is based on the publication

- Clemens Kuhlenkamp, Wilhelm Kadow, Atac Imamoglu, Michael Knap: "Tunable topological order of pseudo spins in semiconductor heterostructures", arXiv:2209.05506 (2022)

Text, figures and structure have been modified for this thesis.

5.1 Spin Liquids and the triangular lattice Hubbard model

If a many-body state is invariant under all symmetries of the Hamiltonian it naively seems to describe a rather trivial *disordered* configuration, such as a paramagnet. In the presence of

strong interactions, however, disordered quantum states can develop intricate entanglement structures and host exotic excitations. Such states are known as spin-liquids and are studied by high-energy, condensed-matter and quantum information physicists alike. Given the large amount of approaches and ideas, it is difficult to write down an inclusive definition of what constitutes a spin liquid without being too restrictive [11, 12]. This makes defining a spin liquid a surprisingly non-trivial task. Nevertheless, there are several properties which a state of matter usually fulfills if it is referred to as a spin liquid:

1. As the name suggests, the building blocks of spin-liquids are usually bosonic *spin* degrees of freedom residing on a lattice. In contrast to conventional magnetic phases, spin-liquids are typically disordered in their quantum ground state and not described by any local order parameters.

2. All spin-liquids host *fractional* excitations: any local operator acting on the ground state generates at least two quasi-particles. Experimentally, this implies that measuring properties of isolated quasi-particles is difficult, since linear response measurements reveal a broad continuum of states rather than a single sharp mode. On a theoretical level this motivates *parton constructions*, where local operators (i.e. $S(x)$) are decomposed into redundant *partons*. These redundancies naturally lead to an emergent gauge-structure and connect the field to high-energy physics. Spin liquids are then identified as the *deconfined phases of gauge theories*. We will discuss this point of view in section 5.7. Since gauge theories are not inherently quantum, fractionalization can also be observed in classical systems, such as spin-ice [170].

3. Ground states of gapped spin liquids should possess a notion of robust long-range entanglement, which makes it impossible to easily connect the spin liquid to a simple product state, such as a ferromagnet. This robustness, which is independent of any symmetry, is called topological order [171].

Already the first requirement is difficult to satisfy, as spin systems at low temperatures have a strong tendency to form various types of magnetic order. The first examples of spin-liquids appeared in the context of magnetic systems on triangular lattices by Philip Warren Anderson in the 70s [172]. Geometric frustration, as it is present on the triangular lattice, is a convenient way to disfavor anti-ferromagnetic order of Ising spins, see Fig. 5.1. The main

71

idea behind Andersons proposal was to find low energy states in the Heisenberg model by superimposing singlet coverings of the lattice. A canonical guess for a spin-liquid wavefunction is a coherent superposition of all dimer coverings, known as a resonating valence bond (RVB) state. Excitations in RVB states are naturally fractional, as breaking a singlet generates two spin-1/2 excitations. However, the RVB state turns out not to be the ground-state of the Heisenberg model on the triangular lattice. Classical order prevails and a 120° Neel ordered state is formed, which is illustrated schematically in Fig. 5.2. This state spontaneously breaks $SU(2)$ symmetry and hosts gapless Goldstone modes. Surprisingly, recent unbiased numerical studies suggest that the triangular lattice Hubbard model does host a bona-fide spin liquid phase close to the Mott transition [41]. The phase diagram is summarized in Fig. 5.3. For $U/t \ll 1$ electrons are mobile and the system is metallic or undergo a superconducting instability. In the complementary limit $U/t \gg 1$ the system is well described by an effective Heisenberg model and orders magnetically. As the Mott transition at $U/t \simeq 9$ is approached from the insulating side, corrections to the Heisenberg Hamiltonian are particularly strong due to the small charge-gap. In this regime the system is found to form a spin liquid, which happens to spontaneously break time-reversal symmetry [173]. This is remarkable and we will discuss the properties of the spin liquid in the next section. However the small area in the phase phase diagram Fig. 5.3 tells us that experiments must be carefully designed to reach and observe a spin liquid regime.

This situation is rather generic. Spin liquids happily exist in theory land but despite having attracted tremendous amounts of theoretical and experimental studies, the decade long quest for the experimental realization of such long-range entangled states has been chal-
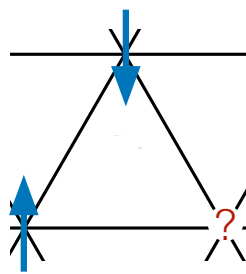

Figure 5.1: Geometric frustration of the triangular lattice for Ising spins. Simple Ising antiferromagnets are forbidden.
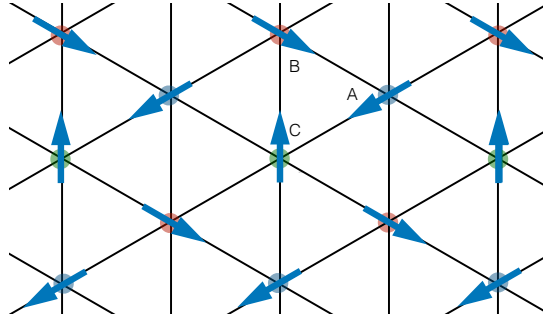
Figure 5.2: 120° Neel state. Illustration of the ground state magnetic order in the Heisenberg model on the triangular lattice. The spins are co-planar. The system is organized in A,B and C sites, on which the spins are ordered in a 120° pattern. Other possible ground-state scan be obtained by SO(3) spin rotations of this configuration.
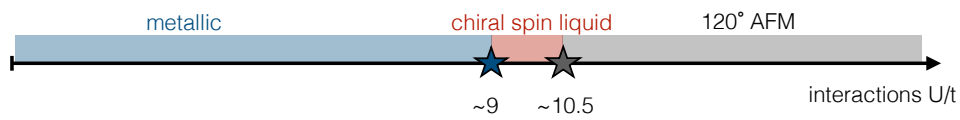
Figure 5.3: Potential diagram of the triangular lattice Hubbard model. The system is found to spontaneously break time-reversal symmetry to form a fully gapped spin liquid close to the Mott transition around $U/t \simeq 9$. Numerical values and a detailed investigation can be found in [41]

lenged by their fragility. In particular, when topological order is encoded in an electronic spin degree of freedom, a characterization and manipulation of the excitations becomes intractable. Even in theoretical models, spin liquids often appear only for very specific parameters, which makes finding good candidate materials difficult [12, 174]. Consequently, conclusive evidence for spin liquids in solids is hard to come by, which makes it essential to identify tunable solid-state platforms that allow for novel probes of the spin liquid states.

Here, we show that large external magnetic fields can induce a particularly rich phase diagram, ranging from Hofstadter physics for small interactions to spin-liquid phases in the Mott insulating regime [175, 172, 176, 173, 177, 64]. Strikingly, the magnetic field reliably tunes ring-exchange processes, which stabilize exceptionally robust chiral spin liquids (CSL) [177, 178]. While this stability is a generic feature of the triangular lattice Hubbard model, we will focus on and propose a particularly natural experimental realization in moiré

heterostructures of two dimensional materials. In both conventional materials and two dimensional materials, large magnetic fields eventually polarize the electronic spin. However, as we have seen in chapter 4, one can retain a $SU(2)$ symmetric model by considering a synthetic layer pseudo-spin degree of freedom instead [179, 180, 59]. By engineering a moiré lattice, the lowest bands of such systems in the presence of external magnetic fields can be described by effective triangular lattice Hubbard models with large lattice constants. The large moiré unit-cell then makes it possible to insert a high enough flux and therefore to explore the full spectrum of the Hofstadter butterfly [175, 181]. This is an ideal setting to study the interplay of geometric frustration and strong interactions [48, 47, 22, 65, 64]. Indeed, we will see that such systems enable us to study a large variety of previously inaccessible phases, including exotic insulator-to-insulator transitions between topological charge and spin sectors.

5.2 FRUSTRATED HUBBARD PHYSICS IN TWISTED TMD BILAYERS
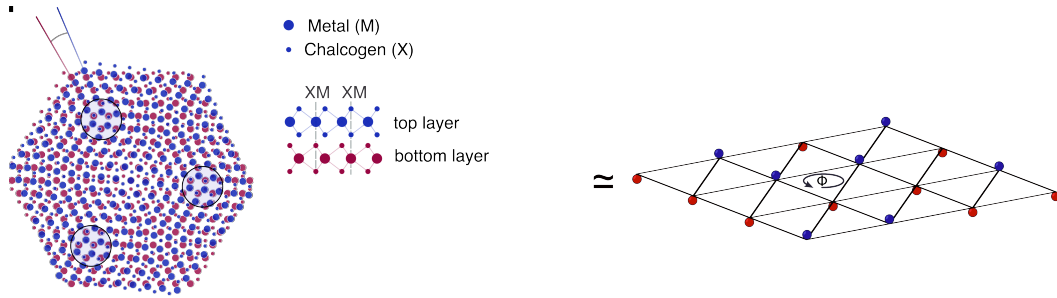
Figure 5.4: Proposed setup. A twisted AB-stacked homobilayer TMD setup to realize a triangular Hubbard model is shown in the left panel. Top and bottom layers are drawn in blue and red. Electrons with pseudo-spin up (down) in the effective Hubbard model are depicted as blue (red) spheres in the right panel.

Heterostructures of two dimensional (2D) materials form moiré patterns, either if there is a lattice constant mismatch between the materials, or if some of the layers are twisted against each other. This commonly results in honeycomb and triangular structures, which imprint lattices on the electrons. Motivated by recent work [64, 182], we consider triangular moiré patterns, in which two lattices in different layers coincide spatially. This can be achieved in multiple ways: in 'sandwich' stacked trilayer systems; for AB-stacked homobilayers with a

74

twist [64, 183], as shown in Fig. 5.4; via twisted hexagonal boron nitride structures in proximity to a homobilayer TMD [182, 184]; or via electrostatically imprinted potentials [185]. Depending on the depth of the lattice potential [186], the lowest lying moiré band of the TMD heterostructure can then realize an effective triangular Hubbard model, with two electronic degrees of freedom: spin and layer. Here we explore the phase diagram of these models by tuning the external magnetic field B_z. Once the Zeeman effect fully polarizes the electrons, their spin can be discarded and the TMD system is described by an interacting Hofstadter-Hubbard model on the triangular lattice:

$$\hat{H} = -t \sum_{\langle ij \rangle, \sigma=\{T,B\}} \left(e^{i\varphi_{ij}} \, c_{i,\sigma}^{\dagger} c_{j,\sigma} + \text{h.c.} \right) + t_{\perp} \sum_i \left(c_{i,T}^{\dagger} c_{i,B} + \text{h.c.} \right) + U \sum_i n_{i,T} \, n_{i,B}, \qquad (5.1)$$

where we have assumed that longer-range interactions have been screened by nearby gates. The operator $c^{\dagger}$ (c) creates (annihilates) spin-polarized fermions and the index $\sigma \in \{T, B\}$ labels the top and bottom layer of the heterostructure, see Fig. 5.4 for an illustration. Electrons are subject to a hopping term with strength t and an inter-layer tunnel coupling $t_{\perp}$. In AB stacking, one of the layers is rotated by $60°$ which exchanges the K and K' points. Due to spin-valley locking, this strongly suppresses $t_{\perp}$. For sandwich structures and twisted h-BN imprinted potentials, $t_{\perp}$ can be made vanishingly small via an insulating barrier. In the following we analyse Eq. 5.1 and assume $t_{\perp} = 0$ throughout. We interpret electrons in the top (bottom) layer as having pseudo spin $+1/2$ ($-1/2$). The magnetic field does not couple directly to the pseudo-spin, and its only effect is the generation of Peierls phases φ_{ij}.

Hamiltonian 5.1 then describes lattice versions of quantum Hall systems, which give rise to a large variety of phases. In the absence of interactions the system realizes a Hofstadter model that hosts a multitude of topologically non-trivial electronic bands which are induced by the magnetic field; see Fig. 5.5 a) for an example. As solid state systems are generically interacting, it is crucial to study the fate of these bands once electron repulsion is considered. While some states directly connect to the Hofstadter model at $U = 0$, interactions stabilize exotic phases of matter. One such example are excitonic superfluids, which arise when pseudo-spin symmetry is broken spontaneously by the interactions. Another, even more exciting possibility, is the formation of states with intrinsic topological order, such as fractional Chern insulators. As opposed to integer Chern insulators they feature emergent gauge fields, anyonic excitations and long-range entanglement [187, 188].
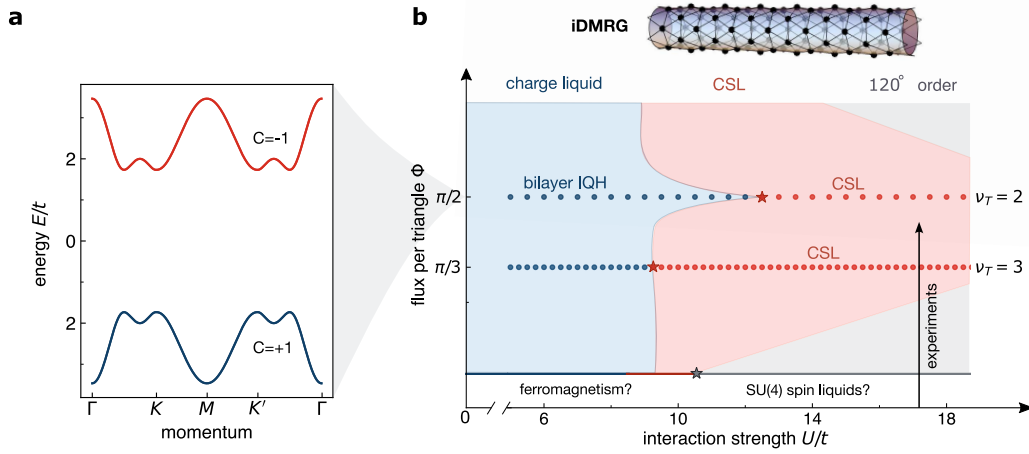
Figure 5.5: Schematic phase diagram. a) Typical topological band structure of the Hofstadter model at $\pi/2$ flux and vanishing interactions. **b)** Schematic phase diagram of the half-filled triangular Hubbard model as a function of flux and interactions. Circles represent iDMRG data obtained on cylinders of circumference $L_y = 6$ and stars mark phase transitions. Remarkably, for intermediate to large interactions the dominant fraction of the phase diagram is a Chiral Spin Liquid (CSL). For weak interactions, the magnetic flux gives rise to a large variety of Hofstadter states, which can directly transition to the CSL.

As correlated insulating phases give rise to particularly interesting spin physics, we consider a single electron per moiré unit cell $n_e = 1$ from now on. This allows the system to become Mott insulating for strong enough interactions, which is the natural regime for TMDs [189, 114, 113]. This limit is understood by eliminating the doubly occupied subspace with a Schrieffer-Wolff transformation [177], leading to the following effective Hamiltonian

$$
\hat{H}_{\text{eff.}} = \frac{1}{U} \sum_{ij,\sigma\sigma'} t_{ij}t_{ji} \left(c_{i\sigma}^\dagger c_{i\sigma'}\right) \left(c_{j\sigma'}^\dagger c_{j\sigma}\right) - \frac{2}{U^2} \sum t_{ij}t_{jk}t_{ki} \left(c_{i\sigma}^\dagger c_{i\beta}\right) \left(c_{k\beta}^\dagger c_{k\alpha}\right) \left(c_{j\alpha}^\dagger c_{j\sigma}\right)
$$
$$
+ \mathcal{O}(t^4/U^3),
$$
(5.2)

which is equivalent to an effective spin system

$$
\hat{H}_{\text{eff.}} = J_H \sum_{\langle ij \rangle} \mathbf{S}_i \cdot \mathbf{S}_j + J_\chi \sum \mathbf{S}_i \cdot (\mathbf{S}_j \times \mathbf{S}_k) + \mathcal{O}(t^4/U^3),
$$
(5.3)

with anti-ferromagnetic Heisenberg interactions J_H and a chiral spin coupling J_χ. The cou-

plings are related to the Hofstadter-Hubbard model parameters as follows

$$J_H = 2t^2/U, \quad J_\chi = 24 \, \sin(\Phi) \, t^3/U^2, \tag{5.4}$$

where Φ is the magnetic flux per triangle, which is given by $\varphi_{ij} + \varphi_{jk} + \varphi_{ki}$ if i, j, k label sites on a single triangle.

Although the triangular lattice is frustrated, the ground state of the pure Heisenberg model, obtained for $U = \infty$, is a co-planar 120 degree (pseudo-) magnet [190, 191]. However, when interactions are lowered or the magnetic flux is increased, the ground state of the fermion system is still a subject of debate. We will show that J_χ can melt the 120 degree order and give way to an exceptionally stable CSL. The hallmark of this exotic phase is a fractionalization of the spins into spinons f_α, which is captured by a parton ansatz $\vec{S} = \frac{1}{2} \sum_{\alpha,\beta=0}^{1} f_\alpha^\dagger \vec{\sigma}_{\alpha\beta} f_\beta$. Expressing Eq. 5.3 in terms of the spinons leads to a Hamiltonian, identical to Eq. 5.2 with electrons replaced by the spinons. The price to pay in this representation is a single occupancy constraint $\sum_\alpha f_{i,\alpha}^\dagger f_{i,\alpha} = 1$ which must be imposed on each site i. This is similar to the Schrieffer-Wolff construction in Eq. 5.2, where we projected out double occupancies to describe the Mott insulator. Spinons evolving with Eq. 5.2 may move freely in a correlated fashion if self-consistently generated hopping terms acquire non zero expectation values $\sum_\beta \langle f_{i,\beta} f_{j,\beta}^\dagger \rangle \neq 0$, but remain confined for conventional magnetic phases such as the 120 degree order. A mean-field decoupling around such configurations leads to simple trial Hamiltonians for the spin liquid:

$$H_{\text{trial}} = \sum_{\langle ij \rangle, \alpha} \tilde{t}_{ij} f_{i\alpha}^\dagger f_{j\alpha}. \tag{5.5}$$

This illustrates one of its key properties: a stable mean field solution for the chiral spin liquid exists, when the (self-consistently determined) hopping matrix $\tilde{t}_{ij} \sim \sum_\beta \langle f_{i,\beta} f_{j,\beta}^\dagger \rangle$ breaks time reversal symmetry and induces topological Chern bands. The ground state of the CSL can be thought of as a Chern insulator composed of spinons. Projecting out double occupancies to satisfy the single occupancy constraint then gives the spinons anyonic character [171, 177]. Despite the fragility of the CSL at zero flux and the fact that a Mott state retains a nonzero (but small) fraction of double occupancies, we will show that magnetic fields strongly favor the formation of a quantum spin liquid, see Fig. 5.5 b) for a schematic

77

phase diagram.

While this discussion assumed strong magnetic fields to fully polarize the electronic spin, we point out that rich physics also arises when Zeeman splittings are small. Then, the system has additional approximate symmetries which have been proposed to give rise to more exotic SU(4) spin liquids [64]. How this and other phases interplay with the Hofstadter states is an interesting open question, which is beyond the scope of this work.

Furthermore our discussion based on the effective spin model neglects higher order ring-exchange processes, which become increasingly important close to the Mott transition. In order to fully capture the properties of the system, we instead study the electronic Hamiltonian of Eq. 5.1 directly, without projecting out the higher energy subspace [41]. In the following, we emphasize the rich physics of the model by studying a subset of phase transitions from Hofstadter states to the CSL.

5.3 Phases of the pseudo-spin Hofstadter-Hubbard model at specific flux

We consider in detail the half-filled triangular Hubbard model deep inside the Hofstadter butterfly regime with two fluxes $\Phi \in \{\pi/3, \pi/2\}$. These flux values correspond to total filling factors of $\nu_T = 2\pi n_e/2\Phi \in \{3, 2\}$, where 2Φ is the flux per unit cell and n_e is the number of electrons per unit cell ($n_e = 1$ at half-filling, which is what we consider throughout this work). For these flux values various exotic phases of matter can be stabilized. For example, at weak interactions the system could realize gapped bilayer integer quantum Hall (IQH) and gapless excitonic insulators, respectively. For large interactions, these phases compete with magnetic ordering and exotic spin liquids. Given the insights from the effective spin model in Eq. 5.3 the precise value of the external flux only determines the ratio of J_χ/J_H in the Mott insulator. However, in the quantum Hall regime its value is essential, as it determines charge gap. In order to determine which phases are stabilized by the microscopic Hofstadter-Hubbard model, we resort to numerical methods.

Studying fermions in magnetic fields poses a significant numerical challenge. Here, we use matrix product states (MPS) to obtain an unbiased variational approximation of the many-body wave function. This Ansatz allows for an expansion in terms of the entanglement,
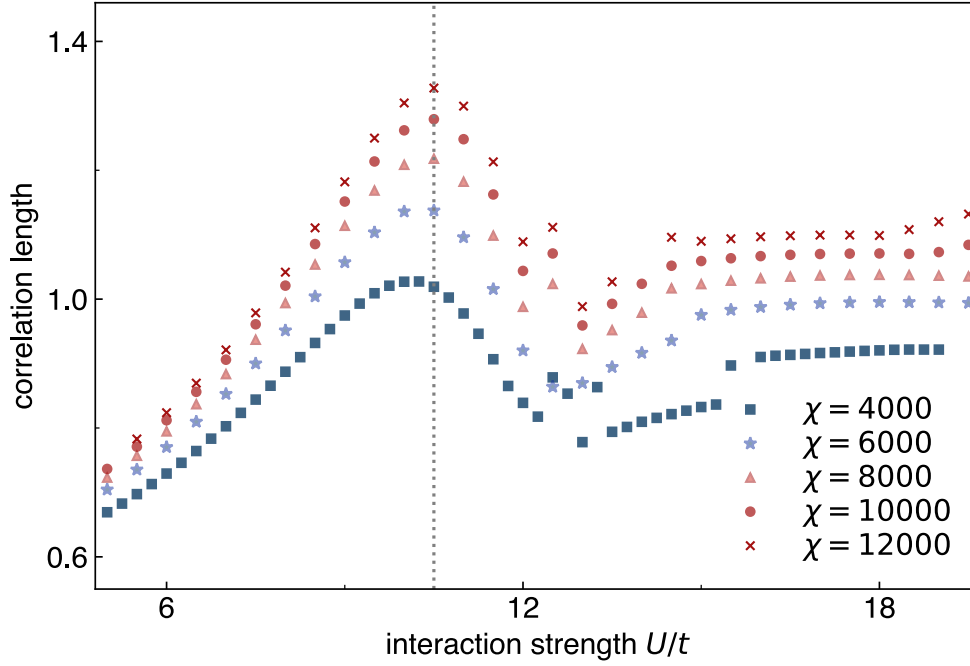
Figure 5.6: Ground state correlation length for $\Phi = \pi/2$**.** We show the correlation length in the charge sector $(S_z, Q, k_y) = (0, 0, 0)$ as a function of U/t for different values of the bond dimension χ. Around $U \simeq 10.5t$ the correlation length grows with bond dimension, which is indicative of phase transition melting the bilayer quantum Hall state. The dotted grey line serves as a guide to the eye.

that is controlled by the maximal bond dimension χ of the MPS. If both the quantum Hall states and the CSL are gapped, they can be efficiently represented in terms of an MPS on a cylindrical lattice, that is finite in one direction but infinite in the other, because the total amount of entanglement is finite for such lattice geometries. This method has been successfully applied to phases with intrinsic topological order, which lead to a better understanding of fractional quantum Hall (FQH) and fractional Chern insulators; see e.g. [192, 193, 194]. We variationally optimize the MPS by infinite Density Matrix Renormalization Group (iDMRG), implemented via the TeNPy library [195]. Since the bond dimension, and hence the numerical costs, grow exponentially with the cylinder circumference, in this work we focus on $L_y = 6$, which fits both fluxes $\Phi = \pi/2, \pi/3$ with periodic boundary conditions.

Working in the infinite limit along the x-direction, we can directly obtain the correlation functions as well as the correlation length from the transfer matrix of the corresponding

MPS unit cell. We use these methods to determine the ground-state phase diagram of the Hofstadter-Hubbard model given by Eq. 5.1. Even though the precise points of the phase transitions may shift depending on the cylinder circumference, we expect the structure of the phase diagram to be similar in the two dimensional limit [41]. To be able to perform the simulations with high bond dimensions and therefore small truncation errors, we utilize the $U(1) \times U(1)$ symmetries generated by the z-component of pseudo spin $\sum_i S_i^z = \sum_i \hat{n}_i^T - \hat{n}_i^B$ and particle conservation $\sum_i \hat{n}_i^T + \hat{n}_i^B$ as well as translation symmetry along the y-direction [196, 197], which determine the S_z, Q, and k_y quantum numbers, respectively.

5.4 QUANTUM PHASE TRANSITION AT $\Phi = \pi/2$

For $\Phi = \pi/2$ flux per triangle and small U/t the system is in a bilayer IQH state, defined by a fully filled topological band with Chern number $C = 1$ for each pseudo spin, see Fig. 5.5a). We find signatures of a phase transition by studying the ground state correlation length as a function of interactions U/t, which is shown for operators carrying the quantum numbers $(S_z, Q, k_y) = (0, 0, 0)$ in Fig. 5.6. As interactions are increased, the correlation length grows significantly with bond dimension around a critical interaction strength of $U_c \sim 10.5t$, which indicates a gap closing phase transition. In contrast to the bilayer IQH state, identifying the phases for $U > U_c$ is more subtle. The most relevant competing states are 120 degree spin-order, tetrahedral spin-order, excitonic insulators, and the chiral spin liquid.

We shed light on the large U phase by noticing that the enhanced correlation length is accompanied by a simultaneous reorganization of the half-cylinder entanglement spectrum, shown in Fig. 5.7 (a,b). The entanglement spectrum directly encodes the energy levels of the edge theory on a half-infinite cylinder, which are distinct for the bilayer IQH and the other candidate phases. The edge theory of the bilayer IQH for small U/t is given by two chiral modes, one for each layer. Their excitations are understood as follows: For $k_y = 0$ there is a unique state where neither of the edge modes is excited, leading to a single dominant entanglement eigenvalue. To create a momentum $k_y = 1 \cdot 2\pi/L_y$ excitation, one can shift the lowest lying electron by one momentum quanta, and promote it to the state just above the Fermi level. As this can be done in both layers, we find two such excitations,
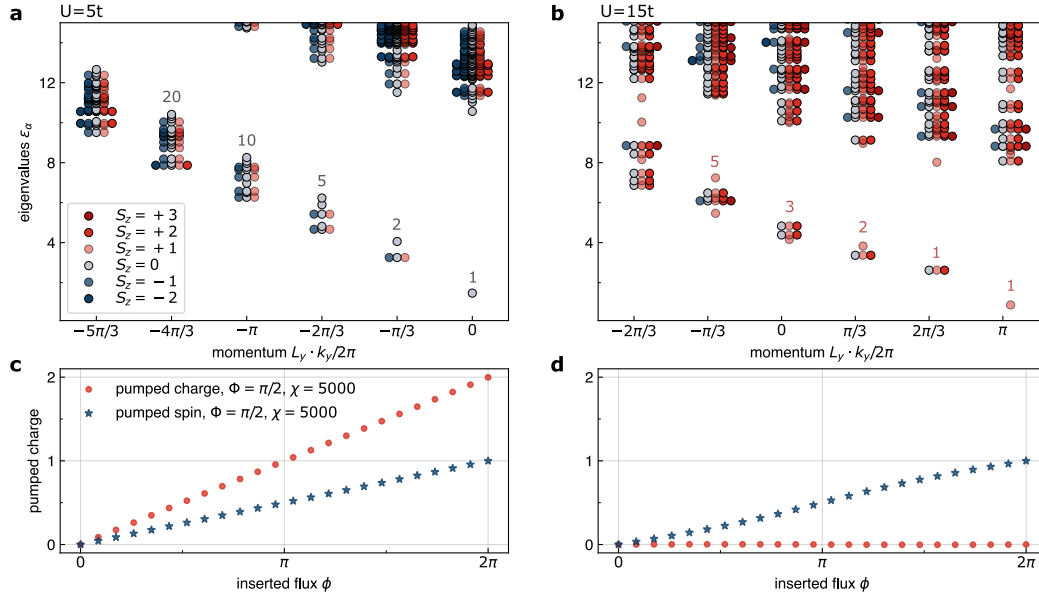
Figure 5.7: Topological properties for $\Phi = \pi/2$. Edge properties and charge pumping for $\Phi = \pi/2$ for $U = 5t$ **(a,c)** and $U = 15t$ **(b,d)**. **a)** Ground state entanglement spectrum in the IQH phase for $\chi = 10000$ and charge $Q = 0$. The spectrum obeys a (1,2,5,10,...) counting rule characteristic for an edge theory of two chiral bosons, which suggests an IQH state in both the top and bottom layer. **b)** Ground state entanglement spectrum in the CSL for $\chi = 10000$ and charge $Q = 0$. The spectrum obeys the (1,1,2,3,5,...) counting rule for the edge theory of the CSL phase. **(c,d)** Pumped charge under flux insertion through the cylinder. Red and blue dots indicate flux that is inserted equally and oppositely in the two layers. While the pumping in **c)** is a direct consequence of two charge-carrying edge modes of the bilayer IQH state, the charge pumping in the CSL regime **d)** vanishes entirely, consistent with the separation of spin and charge degrees of freedom while the spin remains quantized.

leading to two entanglement eigenvalues. In the appropriate basis these excitations decouple completely and correspond to total-density and spin-density wave excitations. Continuing this counting, one finds that the momentum resolved entanglement spectrum for increasing momenta k_y is given by $(1, 2, 5, 10, \dots)$ entanglement eigenvalues in each spin sector, see Fig. 5.7 a). These density- and spin-wave modes are arranged in a representation of an underlying $U(1) \otimes SU(2)_1$ algebra, as expected for the boundary of a double copy of an IQH state. For $U > U_c$, on the other hand, the ground state loses several edge excitations; see Fig. 5.7 b). This is natural once the system turns Mott insulating, at which point density waves acquire a finite energy cost. The spectrum then consists only of spin waves described by a representation of the $SU(2)_1$ algebra, which leads to a $(1, 1, 2, 3, 5, \dots)$ counting. The

edge is therefore captured by a chiral $SU(2)_1$ Wess-Zumino-Witten model, which matches the edge theory of the chiral spin liquid [198, 199].

We further analyse the topological character of the bilayer IQH and the suspected CSL by inserting fluxes through our cylinder, which realizes Laughlins charge pump [200, 201]. The IQH state responds to the insertion of 2π magnetic flux by transferring a single charge from one end of the cylinder to the other in each layer, illustrated in Fig 5.7 c) (red markers). To couple to the charge-neutral spin edge modes, one has to thread opposite fluxes in the two layers. The IQH state then pumps one electron in the top and one hole in the bottom layer each carrying a spin of 1/2, leading to a pseudo-spin transfer of unity, see Fig 5.7 c) (blue markers). Combining these results, we infer that the excitations carry both charge and spin.

For $U > U_c$ the system no longer pumps electric charge when threading magnetic fluxes, consistent with a Mott insulating state. However, it still exhibits quantized spin transfer for oppositely inserted fluxes, see panel d) of Fig. 5.7. Inserting π flux for the electrons corresponds to a 2π flux insertion in the effective spin Hamiltonian Eq. 5.3. From this point of view we pump a single spin after threading 4π spin-flux, realizing a fractional spin Hall effect. This can be intuitively understood via the Kalmeyer-Laughlin construction, where the spin system is mapped to a half-filled Bose-Hubbard model in the presence of a fictitious background magnetic field [176]. Our observed spin pumping is then explained by the formation of a $\nu = 1/2$ bosonic FQH state which is identified as the chiral spin liquid in the spin picture. As such, excitations of the CSL are semions, which are abelian anyons with a statistical phase $\theta = \pi/2$. This leads to a doubly degenerate ground state on cylinders in the thermodynamic limit $L_y = \infty$, which reside in the $k_y = 0$ and $k_y = \pi$ momentum sectors respectively. In our geometry, the ground state energies in these sectors approach each other and cross shortly after the transition, which is a finite size effect of our simulations [41, 178]. The same conclusion can be reached starting from a purely fermionic model, although the discussion is more involved [171]. The fractional spin-Hall effect and the absence of charge transport therefore serves as a direct signature of a fractional Hall state for spin. Putting these findings together we identify the phase into which the bilayer IQH phase transitions when increasing interactions to $U > U_c$ as a CSL.
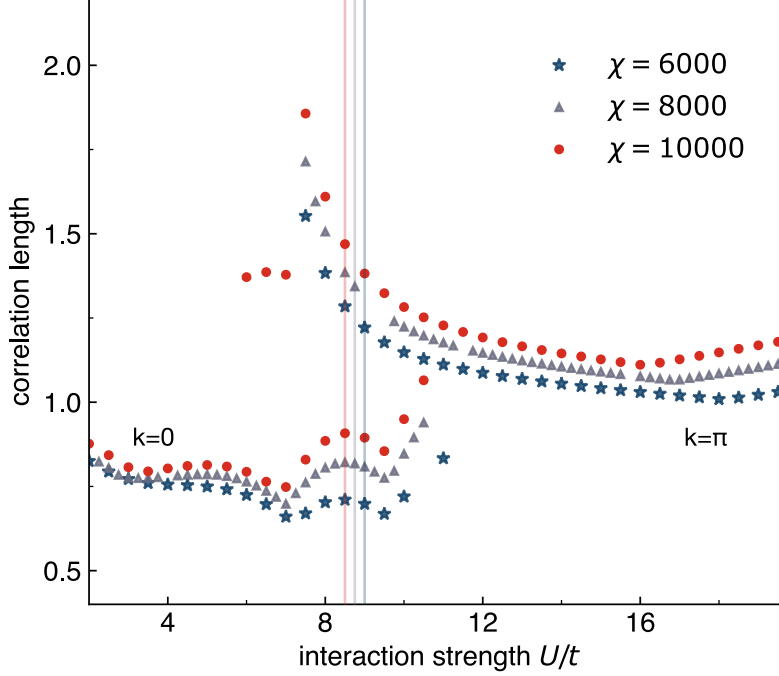
Figure 5.8: Transition for $\Phi = \pi/3$. The ground state correlation length for operators in the sector $(S_z, Q, k_y) = (0,0,0)$. In the lowest energy $k_y = \pi$ state, the correlation length strongly increases around $U \simeq 8.5t$, indicating a sharp transition to a chiral spin liquid. The energy crossing of the $k = 0$ and $k = \pi$ states is indicated by the vertical lines and is a finite size effect. The two momentum states are expected to be the degenerate ground states of the CSL in the thermodynamic limit.

For $\nu_T = 3$, we no longer expect a quantized Hall conductance as the Landau bands are partially filled. This opens the possibilities for other charge liquids, such as excitonic superfluids. Here, we choose unit cells of size $L_x = 3$, which allows us to reliably prepare states with fixed momenta along the y-direction. We provide details in appendix B, where we find that for small U/t the system does not exhibit any quantized pumping. Although it is suggested by the continuum limit, we do not find long range ferromagnetic correlations of the Hall liquid, which may be a feature of the Hofstadter-Hubbard model at half filling. While we cannot uniquely identify the nature of this state, its response is consistent with a featureless Hall state [202]. However, once interactions are raised a sharp transition occurs around $U \simeq 8.5t$, as evidenced by the growing correlation length; see Fig. 5.8.

We find that the transition (on finite cylinders) occurs in steps: First, for small U/t the ground state is found at zero momentum. As U increases the correlation length in the $k_y = \pi$ sector diverges. Then, quickly after this divergence the $k_y = \pi$ state becomes the new ground state of the system. Afterwards the energy splitting between the two states remains roughly constant, as shown in appendix B.

There are several possible candidate states once the system becomes insulating. Following the analysis of the previous section we can identify the phase for $U \geq 8.5t$ as a CSL, see appendix B. In particular, the state exhibits a fractional spin-Hall effect and shows the characteristic half-cylinder entanglement spectra. Although the $k_y = 0$ state is higher in energy than the $k_y = \pi$ state for $U \geq 8.5t$, the edge theories of both states are in good agreement with the $SU(2)_1$ WZW model describing the boundary of the CSL.

While the robust spin liquid is a universal feature of the large U phase for both fluxes, the charge to spin liquid transitions are clearly distinct for $\nu_T = 2$ and $\nu_T = 3$. Most notably for $\nu_T = 3$ the CSL appears already for much weaker interactions compared to $\nu_T = 2$. This indicates that the charge liquid at $\nu_T = 3$ is less stable, than the $\nu_T = 2$ bilayer IQH state. A sketch of the expected phase boundaries is shown in Fig. 5.5 c). This behaviour is reminiscent of the competition between Wigner crystals and Hall states in electron gases, where integer and fractional quantum Hall states extend further into the gapped crystalline phase than their gapless counterparts [203, 113].

5.6 Signatures of layer pseudo spin

Potentially the biggest challenge in spin-liquid physics is to find experimental signatures for their existence. Many of the previously proposed detection schemes of electronic-spin liquid states —such as a quantum thermal Hall effect—are readily generalized to layer-spin systems. However, layer pseudo spin is easier to manipulate and probe which presents a crucial advantage and opens new avenues to detect the spin liquid: (I) By turning on an external magnetic field B_z the ground state changes from a 120 degree Néel state at $B_z = 0$ to the CSL, as sketched in Fig. 5.5 b). Associated experimental signatures are the temperature dependence of the pseudo spin susceptibility $\chi(T)$. At high temperatures, it follows the net-Weiss law $\propto (T - \theta_{CW})^{-1}$, with negative Curie-Weiss temperature θ_{CW} due to an-

tiferromagnetic interactions. At low temperatures, the Néel phase has a broad peak and approaches a constant value towards $T = 0$. The CSL, on the other hand, has a spin gap Δ_S, which leads to exponential decay of $\chi(T)$ below $k_B \Delta_S$. As we discuss below, $\chi(T)$ can be measured optically, which makes these signatures accessible in present-day experiments. (II) In stark contrast to intrinsic electronic spin, pseudo-spin can be electrically addressed, which allows us to couple the two pseudo-spin states to different electric fields (cf. discussion surrounding Fig. 5.7 c) and d)). This enables counterflow measurements, which will exhibit a fractionally quantized Hall response, a hallmark of a CSL. While sample inhomogeneity and the difficulty in electrical isolation of the two layers render such a measurement rather demanding, it would be able to uniquely identify the topological order of the chiral layer-pseudo-spin liquid and distinguish it from all other phases in the phase diagram [64]. (III) Topological properties of the CSL are encoded in the gapless modes on its edge [204]. In addition to spin-modes, one can measure the decay of electron correlation functions $\langle c_\sigma^\dagger(x, t) c_{\sigma'}(0, 0) \rangle$ on the edge, which serve as additional probes of the spinons.

While observing fractional pseudo-spin Hall conductivity requires transport experiments, other signatures of the CSL could be obtained using all-optical measurements, which overcome several obstacles through tight focusing of the probe lasers into regions where the moiré potential is uniform. The spin-susceptibility at finite field E_z can be extracted via the attractive polaron resonance strength of each layer, which measures how many electrons the exciton can form a bound trion state with and thereby directly depends on the electron density [57, 205]. Probing the pseudo-spin magnetization $\langle S_z \rangle$ is then possible since each layer generically has a different exciton resonance*. As outlined above, measurement of magnetization as a function of E_z at low temperatures $k_B T \ll \Delta_s$ should show the existence of a spin-gap. The appearance of the charge gap in turn, is evidenced by the cusps in attractive and repulsive polaron resonances, indicating the modification of dynamical screening of excitons by electrons [47]. Such local probes are particularly relevant for near term devices as they are readily accessible and largely insensitive to large-scale disorder. Further, direct evidence for the emergence of a gauge field could be verified using optical Hall measurements. It has been demonstrated that effective electric fields can be imprinted on excitons using crossed magnetic and time dependent electric fields [206]. A combination of such an effec-

---

*This is true also for twisted homobilayer structures where strain lifts the degeneracy of the exciton resonance

tive dipole electric field and the emergent gauge field should result in layer-contrasting Hall effect [207], which can be measured by determining the spatial dependence of the attractive polaron resonance in each layer along the axis that is orthogonal to the dipole electric field. Furthermore, novel momentum-resolved techniques unique to 2D materials could also allow for the measurement of ARPES-like spectra [208] which can provide signatures of spinon excitations in quantum spin liquids [209].

Complementary insights could be obtained by measuring $\langle S^z_{\mathbf{q}=0}(t)S^z_{\mathbf{q}=0}(0)\rangle$ using correlations between resonantly scattered photons on the attractive polaron resonance. If coherent optical Raman manipulation of layer pseudo-spin is possible, then suppression of spin noise along all axes for $k_B T \ll \Delta_s$ can be measured [210].

5.7 Gauge theory interpretation and phase transitions

We now construct the field theory describing the appearance and disappearance of the chiral spin liquid. While the construction of such theories is rather standard, it gives us important experimental hints on how one may go about probing the spin liquid and provides us with potential critical theories which give rise to these exotic phases. We will therefore give more details than necessary. What follows is largely based on [211]. Understanding the critical theory in our system is important for several reasons:

- The critical theory illustrates the mechanism with which the chiral spin liquid is lost. Although the transition may be first order, this gives insights as to how a realistic spin liquid state could be stabilized.

- While topological order is hard to detect, change of order has much stronger thermodynamic and dynamical signatures. Indeed, we have seen in chapter 3 that soft modes heralding phase transitions can be detected in experiments. As such, critical points are of primary interest to experiments. Unfortunately, the critical theory of the chiral spin liquid is non-trivial and hard to solve. Not all is lost, however, as we can still make predictions that can serve as strong experimental evidence for the formation of the chiral spin state.
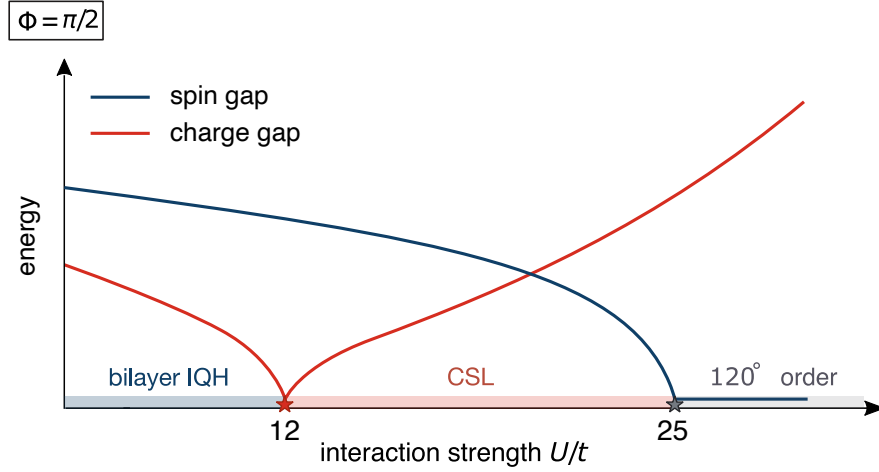
Figure 5.9: Schematic of potential gap closings at $\Phi = \pi/2$. For $U/t \le 12$ the system is in a fully gapped integer quantum Hall state with $C = 2$. The Mott transition is driven by closing of the charge gap, leading to the CSL state with total $C = 0$. Later on the charge gap grows with U, while the spin remains closed once the system forms 120° order at around $U/t \gtrsim 25$.

- We will see that the transitions of the CSL are related to a remarkable duality web [5]. While this is not immediately useful for experiments, it relates to deeper physical structures within quantum field theory.

Before discussing the critical point, we motivate the main ingredients of our physical description based on our numerical results. The first transition from Chern insulator to chiral spin liquid changes the Hall conductivity. The Chern insulator at low U/t has a total Chern number $C = 2$ while the chiral spin liquid is a charge-insulator with $C = 0$. This implies a closing and opening of the charge gap at the Mott transition. Furthermore, the system supports edge spin-waves described by the $SU(2)_1$ theory in both phases, which suggests that the bulk spin gap remains open. The second transition to the 120° Neel state is comparatively simpler. At $U/t \gg 1$, exciting charges is very costly, but the system hosts gapless spin waves due to the formation of 120° magnetic order. As such this transition will be described by a closing of the spin-gap. This scenario is depicted in Fig. 5.9.

Motivated by the above it seems that charge and spin-degrees of freedom could decouple in this system. This suggests the following decomposition of the electron operator [211]:

$$c_{i,\sigma} = f_{i\sigma} b_i, \qquad (5.6)$$

87

where the *spinon* $f_{i\sigma}$ carries information about the spin, while the *chargon* described by b_i encodes charge fluctuations. This provides a first hint pointing towards the emergence of a gauge structure, since this expression remains invariant under the local U(1) transformations:

$$f_{i\sigma} \to e^{i\alpha_i} f_{i\sigma}, \qquad b_i \to e^{-i\alpha_i} b_i. \tag{5.7}$$

This invariance is built into the parton ansatz and must hold in everything that follows to faithfully describe the Fermi Hubbard model. Such a decomposition is always possible. It corresponds to a drastic, artifical enlargement of the local Hilbert space dimension. Among the set of enlarged states there are only four physical states per site

$$
\begin{aligned}
|0\rangle_{\text{phys}} &\leftrightarrow & |0\rangle_{\text{gauge}} \\
c_\uparrow^\dagger |0\rangle_{\text{phys}} &\leftrightarrow & |n_f^\uparrow = 1, n_b = 1\rangle_{\text{gauge}} \\
c_\downarrow^\dagger |0\rangle_{\text{phys}} &\leftrightarrow & |n_f^\downarrow = 1, n_b = 1\rangle_{\text{gauge}} \\
c_\uparrow^\dagger c_\downarrow^\dagger |0\rangle_{\text{phys}} &\leftrightarrow & |n_f^\uparrow = 1, n_f^\downarrow = 1, n_b = 2\rangle_{\text{gauge}},
\end{aligned}
\tag{5.8}
$$

where $n_f^\sigma = f_\sigma^\dagger f_\sigma$ and $n_b = b^\dagger b$ label the occupation of spinons and chargons. In other words physical states must satisfy the gauge constraint that

$$\sum_\sigma f_{i,\sigma}^\dagger f_{i,\sigma} = b_i^\dagger b_i, \tag{5.9}$$

on every site i. This can be viewed as a version of Gauss's law, satisfied by every physical state, and expresses the fact that spinon and chargon carry opposite charge under the local U(1) symmetry. On this level we can perform an exact rewriting of the partition function of the Fermi Hubbard model:

$$
\begin{aligned}
Z &= \int \mathcal{D}a^0 \int \mathcal{D}f\mathcal{D}\bar{f} \int \mathcal{D}b\mathcal{D}\bar{b} \quad e^{iS[f,b]} e^{i\sum_i \int dt\, a_i^0 \left(\bar{b}_i b_i - \sum_\sigma \bar{f}_{i\sigma} f_{i\sigma}\right)} \\
S[f,b] &= \int dt \sum_{i,\sigma} \bar{f}_{i,\sigma}\, i\partial_t\, f_{i,\sigma} + \bar{b}_i\, i\partial_t\, b_i + t \sum_{\langle ij \rangle,\sigma} e^{i\varphi_{ij}}\, \bar{f}_{i,\sigma} f_{j,\sigma} \bar{b}_i b_i + \text{h.c.} - \frac{U}{2}\sum_i |\bar{b}_i b_i|^2,
\end{aligned}
\tag{5.10}
$$

where we introduced a real scalar a_0 to satisfy the gauge constraint Eq. 5.9 and used that the Hubbard interactions only depend on the total charge described by the chargons. This is arguably worse than what we started with due to the correlated hopping. The standard ap-

proach to simplify the action is to decouple the correlated hopping via a Hubbard-Stratonovich field $\chi_{\langle ij \rangle}$, yielding a new action

$$
\begin{aligned}
S[f, b, \chi] = \int dt \sum_{i,\sigma} \bar{f}_{i,\sigma} \, i\partial_t \, f_{i,\sigma} + \bar{b}_i \, i\partial_t \, b_i + \frac{1}{t} \sum_{\langle ij \rangle} \bar{\chi}_{\langle ij \rangle} \sigma_x \, \chi_{\langle ij \rangle} \\
- \sum_{\langle ij \rangle} \left(\bar{\chi}_{\langle ij \rangle} \Psi_{\langle ij \rangle} + \bar{\Psi}_{\langle ij \rangle} \chi_{\langle ij \rangle} \right) - \frac{U}{2} \sum_i |\bar{b}_i b_i|^2,
\end{aligned}
\tag{5.11}
$$

where we have grouped $\Psi_{\langle ij \rangle} = (\bar{f}_{i,\sigma} f_{j,\sigma} e^{i\varphi_{ij}}, \bar{b}_j b_i)^T$. The saddle point of Eq. 5.11 demonstrates mutually generated hopping terms, since $\chi_{\langle ij \rangle} = t\sigma_x \langle \Psi_{\langle ij \rangle} \rangle$, which indicates that spinons see flux and completely fill Chern bands on the triangular lattice, while the chargons do not. Since we are interested in the proximity to the critical point and the systems ground-state properties, most microscopic details, such as the lattice constant, are unimportant as long-wavelength fluctuations dominate the systems behaviour. However, under gauge transformations the Hubbard Stratonovich field transforms as a gauge field $\chi_{\langle ij \rangle} \rightarrow e^{i(\alpha_i - \alpha_j)} \chi_{\langle ij \rangle}$, which constrains the effective action. Assuming a closed manifold, the spinons can be integrated out in the bulk, where they contribute a Chern-Simons term at level $C = 2$. The charges on the other hand are gapped out in the Mott phase. The critical theory for a Mott transition in a bosonic field is well known and hosts a relativistic symmetry as the transition is not density changing [3]. The particle excitations of ϕ essentially describe double occupancies close to the Mott state, while anti-particles correspond to holes. Following Ref. [3] one obtains the following effective action valid in the vicinity of the Mott transition:

$$
S[a, \varphi] = \frac{2}{4\pi} \int a \wedge \mathrm{d}a + \int \mathrm{d}^3 x \, |(i\partial_\mu - A_\mu + a_\mu)\phi|^2 + m^2 |\phi|^2 - \lambda |\phi|^4 + \dots, \tag{5.12}
$$

where A_μ is the background vector potential, where we have kept only relevant terms in the renormalization group sense. We now discuss the phases appearing in limiting cases.

(I) Weak interactions: Physically, we expect any bosonic field to condense at low temperatures in the weakly correlated regime. At tree level this condensation transition appears for $m^2 > 0$. Coupling to the U(1) gauge fields A_μ and a_μ affects the U(1) symmetry breaking due to the Anderson-Higgs mechanism [119]. A translationally invariant mean-field solution $\langle \phi \rangle \neq 0$ exists when $a = A$. This removes fluctuations of the gauge field a and leaves

89

behind a gapped superfluid. However, the Chern-Simons term remains and now reads:

$$S_{\langle \phi \rangle \neq 0}[a, \phi] = \frac{2}{4\pi} \int A \wedge dA + \dots . \qquad (5.13)$$

Since A is the background electromagnetic gauge field, this action describes a genuine $C = 2$ integer Quantum Hall effect, as we have observed numerically [171]. This is also seen directly from the parton ansatz of Eq. 5.6 where spinons can be identified with electrons in the Higgs phase $c_{i,\sigma} = f_{i\sigma} \langle b_i \rangle \sim f_{i\sigma}$, which suggests that the electron operator is not fractionalized.

(II) Strong interactions: In this regime double occupancies and holes are energetically strongly suppressed and the system develops an interaction induced gap. In the effective action 5.12 this occurs when $m^2 < 0$. In this limit ϕ can be integrated out. Since the coefficient of the Chern-Simons term is quantized, it is not renormalized and describes a $\nu = 1/2$ fractional quantum Hall effect [171]. The Chern-Simons action essentially encodes a flux attachment procedure. Coupling a spin or charge current $f_\mu^{s,c}$ minimally to a_μ yields a flux attachment, such that spin and charge excitation transmute into semions with a statistical phase of $\theta = \pi/2$.

(III) IQH to CSL Critical point: At the critical point, the system undergoes a Mott transition to change the quantized Hall conductivity. Both sides of this topological transition are gapped insulators, while the charge gap at the critical point vanishes, suggesting a finite conductivity close to the critical point. This is rather peculiar and can potentially probed via AC and DC conductivity measurements. Furthermore the critical point of Eq. 5.12 is proposed to have a dual fermion description: The Wilson-Fisher fixed point of a boson coupled to a level-2 Chern-Simons action $U_2(1)$ is dual to a fermion plus a $U_{-3/2}(1)$ Chern-Simons theory [5]. We will not treat this dual description of critical point in detail here, but it serves as a good starting point to make experimental predictions about the transition and to search for extended symmetries.

This gives a rather complete picture of the topological phase transition at $U/t \simeq 12$. Although we did not observe it numerically, we expect that a second transition takes place for $U/t \geq 20$ after which the system should form a $120°$ Neel state [178]. Since the magnetic phase is confined one of two things will happen: either a field that is charged under
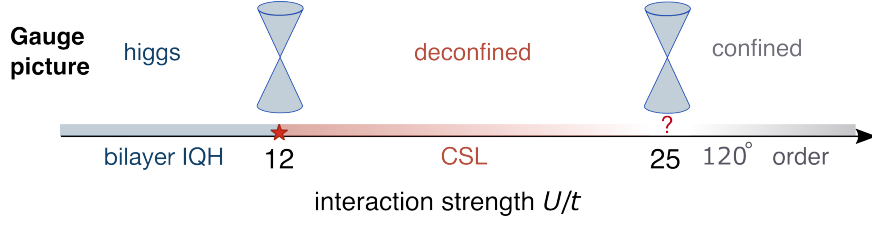
Figure 5.10: Schematic phase diagram and interpretation in the gauge picture. The integer quantum Hall effect can be understood as a Higgs phase, where the Meissner effect requires the emergent and physical gauge fields to equal to each other $a = A$. The transition to the chiral spin liquid at $U \simeq 12$ can be continuous and is dual to a Dirac fermion. The magnetic ordering transition at $U \simeq 25$ deep inside the Mott phase, is accompanied by the softening of a spin-wave mode at the K/K' point. A natural mechanism for a continuous ordering transition would be the closing of the spinon dispersion at another Dirac point.

the emergent $U(1)$ symmetry is condensed leading to a Higgs mechanism, or the topological spinon-gap closes which confines the $U(1)$ gauge theory by monopole proliferation [212]. The latter has a natural interpretation: the chiral spin liquid is a $U(1)_2$ fractional Quantum Hall state of spins. We have seen in chapter 3, such states generically give rise to soft (spin) density wave modes [118]. In our case this would imply a softening of spin-wave modes at the K/K' points, which are the ordering wavevectors of the Neel state. These soft spin-waves can be identified as vortex anti-vortex pairs [213], which can become soft due to a closing of another Dirac cone. This provides an appealing picture describing the phase boundaries of the CSL state, which we depict in Fig. 5.10. In the future it will be interesting to develop numerical and analytical tools to study their properties. Furthermore, the softening of a spin-density-wave mode at K/K' momentum can be experimentally explored via quantum twist microscopes [208, 214].

We have shown how a large class of quantum phases and transitions can be studied in multi-layer TMDs. In particular, topologically ordered CSLs can be stabilized by utilizing the layer degree of freedom as a synthetic spin [64, 59, 215]. The absence of a magnetic Zeeman effect for the pseudo-spin allows us to target topological states by controlling the strength of ring exchange processes using large external magnetic fields. For weak interactions a variety of Hofstadter states can be prepared by sweeping B_z, while a CSL forms for intermediate interaction strengths. At specific fluxes, our model realizes topological insulator-insulator Mott transitions. Understanding the details of these transitions is an interesting direction for future work and will help to better understand the phase boundaries of the CSL. Remarkably, the field induced CSL is found to be exceptionally robust and occupies a large region of the phase diagram. Combined with the electric tunability and layer-selective read-out of layer pseudo-spin, this makes TMD heterostructures particularly promising platforms to study spin liquid physics. Novel probing schemes unique to the pseudo-spin degree of freedom offer an additional advantage of these systems over conventional spin liquid candidates. Competing spin and charge ordered phases can be more easily identified; while counterflow measurements [64] directly probe the topology of the spin liquid. It is also possible to find fingerprints of the spin liquid phase with all optical measurements, which provide local probes that are crucial for near-term devices.

Our results open up several theoretical and experimental avenues to study topological order and exotic phase transitions. For one, Mott insulators can be stabilized at fractional fillings by longer-ranged interactions, leading to spin systems with different lattice geometries and more exotic states for small interaction strengths. More specifically, for $\Phi = \pi/3$ densities of $n_e = 1/3, 1/9, \ldots$ realize excitonic insulator candidates and FQH states respectively, both of which eventually transition to frustrated spin states in Mott-Wigner insulators at large U/t. This poses interesting questions about the nature of quantum phase transitions between topological order in the charge and spin sectors. Furthermore, in the weak field limit a variety of interesting competing states emerges, and their interplay is largely unexplored. Most notably, this regime is expected to feature Hofstadter physics, quantum Hall ferromagnetism and $SU(4)$ spin liquids [64].

A

Feshbach resonances

A.1 Exciton electron interactions and renormalization

Since excitons in TMDs are tightly bound, we have treated the exciton-electron scattering as an effective two particle problem. Microscopically, however, the scattering properties and the exciton-electron potential need to be determined from the eigenstates of the three body problem of a single hole and two electrons. It was shown in Ref. [51], that a simple contact potential between exciton and electron of the form

$$\hat{V} = U \sum_{\mathbf{k},\mathbf{k}',\mathbf{q}} x^{\dagger}_{\mathbf{k}} x_{\mathbf{k}-\mathbf{q}} \, c^{\dagger}_{\mathbf{k}'} c_{\mathbf{k}'+\mathbf{q}}, \tag{A.1}$$

can adequately reproduce the correct long-wavelength scattering physics, if logarithmic UV divergences due to large-momentum virtual states are properly renormalized. Such divergences express the fact that naive contact-like interactions of the form $V(\mathbf{x}) = U\delta^2(\mathbf{x})$ are

ill-defined, which can be fixed by introducing a momentum cutoff Λ and a regularized interaction strength U_Λ, which boils down to replacing $V(\mathbf{x})$ by a pseudo-potential $V_\Lambda(\mathbf{x})$. The idea here is that the pseudo-potentials strength and width —controlled by U_Λ and Λ, respectively— can be tuned to match the proper scattering physics of the underlying microscopic model.

U_Λ is matched by ensuring that the scattering length a, or the relevant binding energy E_B^0, is correctly reproduced. To fix U_Λ we compute the T-matrix and match the position of its pole to the physical value of E_B^0

$$\frac{1}{U_\Lambda} = \int\limits_{|\mathbf{k}|<\Lambda} \frac{d^2\mathbf{k}}{(2\pi)^2} \frac{1}{E_B^0 - \frac{\mathbf{k}^2}{2\mu_{\mathrm{red}}} + i0^+}. \tag{A.2}$$

The binding energy of the exciton-electron complex in monolayer TMDs has been experimentally determined to be around $E_B^0 \simeq 30\mathrm{meV}$. Note that while cut-off Λ is now a free parameter, it tunes the width of $V_\Lambda(\mathbf{x})$ potential as it represents the largest resolvable momentum scale. Taking Λ much larger than any other physical scale, while fulfilling Eq. A.2, ensures that we are describing a short range potential, which is fully captured by specifying E_B^0.

A.2   INTERLAYER SCATTERING

If the spatial separation between the two semiconductor layers is sufficiently large, interlayer scattering in the open channel can be safely neglected. For small separations, or for Feshbach resonances formed with inter-layer excitons, inter-layer molecules may form. As a top-layer exciton with an electron (or hole) in the opposite layer constitute the open channel, an inter-layer molecule (trion) leads to attractive background scattering. Here we study the effect of background scattering on the Feshbach resonance discussed in the main text, by solving Eq. 2 in the presence of an inter-layer molecule with binding energy E_{IB}. Motivated by recent experiments on spatially separated TMDs which suggest inter-layer binding energies $E_{IB} \leq 0.5$ meV, we focus on weak background scattering. The resulting eigenenergies of the system are shown in Fig. A.1(a) for $E_{IB}/E_B^0 = 1/30$ and $t/E_B^0 = 1/10$.
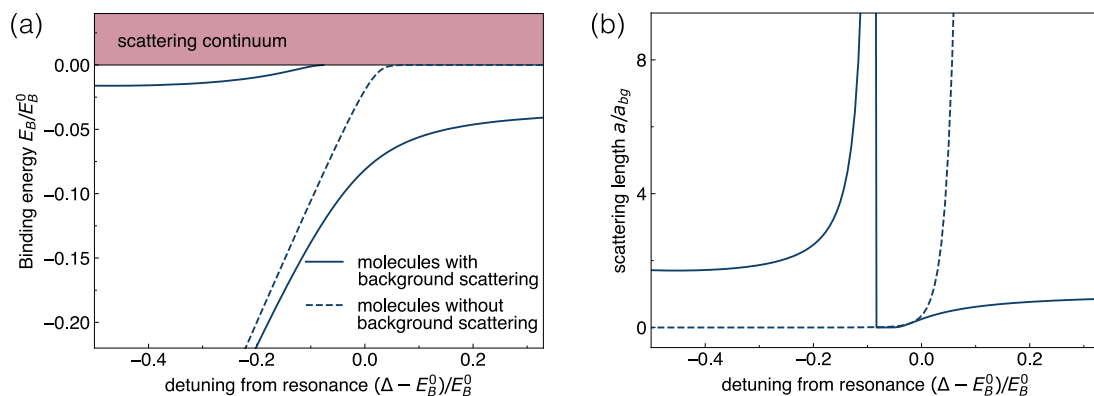
Figure A.1: Exciton electron problem and the effects of background scattering. (a) Molecular energies measured from threshold as a function of detuning. Molecules in the presence (absence) of an inter-layer bound state are shown as solid (dashed) lines. Hybridization between the inter- and intra-layer molecule pushes the Feshbach molecule into the continuum for finite detunings, where it unbinds. For large positive detunings the only remaining bound state is the open channel (inter-layer) molecule. **(b)** Scattering length determined by fitting the low-momentum T-matrix in the open channel. In the presence of inter-layer scattering (solid line) the scattering length diverges when the lowest lying molecule dissolves. In the absence of the inter-layer scattering the molecule remains stable for all detunings (dashed line).

Far from resonance, the molecule with highest energy approaches the energy of the inter-layer trion E_{IB}. Once the inter- and intra-layer molecule energies are comparable the two states repel and the Feshbach molecule is pushed into the continuum, leading to a diverging scattering length even at finite detuning shown in Fig. A.1(b).

While the scattering length remains fully tunable, background scattering may modify many-body properties such as Fermi polaron spectra. We investigate this possibility by including weak attractive inter-layer interactions in our T-matrix analysis.

The resulting spectrum is shown in Fig. A.2(a), and retains the characteristic asymmetry between attractive and repulsive polaron. The repulsive polaron branch, however, never loses its spectral weight completely, which is in contrast to the case of vanishing background scattering as shown in Fig. A.2(b). The repulsive polaron persists, since the Feshbach molecule asymptotically approaches E_{IB} for large electric fields. In the limit $E_{IB} \ll E_F$ the weight of the repulsive branch vanishes for large electric fields, recovering the situation discussed in the main text.
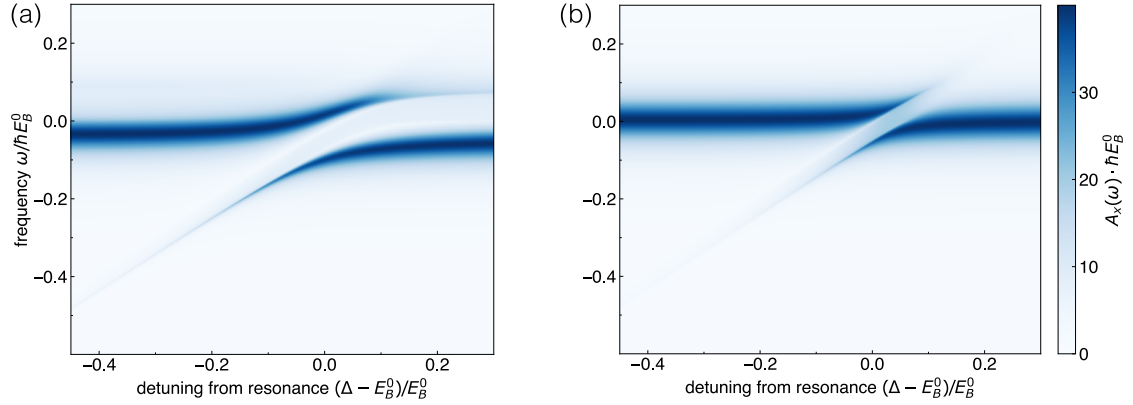
Figure A.2: Comparison of exciton spectra. **(a)** Spectral function of the exciton as a function of detuning, for an inter-layer molecule energy $E_{IB}/E_B^0 = 1/60$ and $E_F/E_B^0 = 1/15$. For large detunings, the two branches correspond to the attractive and a repulsive polaron associated to the inter-layer trion. Due to attractive background scattering the repulsive branch never fully dissolves, however the spectral weight transfer between the branches remains strongly asymmetric. It occurs when the binding energy of a molecule is comparable to the Fermi energy. **(b)** Exciton spectral function in the absence of background scattering (cf. Fig. 4 in the main text). In this case the binding energy of the Feshbach molecule vanishes asymptotically for large detunings, where the polaron energy quickly approaches that of a bare exciton.

A.3 NON-EQUILIBRIUM FORMALISM

In the following we find an approximate solution to Eq. (9) of the main text using non-equilibirum field theory. It has been shown that generic Master equations can be mapped to a functional integral. This is achieved by rewriting the real time evolution of Eq. (9) in a coherent state basis, which yields a field theory on a Keldysh contour [158]. As the density matrix is now in general non-thermal, the system admits two possibly inequivalent correlation functions

$$\mathcal{G}_{\mathbf{k}}^{>}(t,t') = -i\langle x_{\mathbf{k}}(t) x_{\mathbf{k}}^{\dagger}(t')\rangle,$$
$$\mathcal{G}_{\mathbf{k}}^{<}(t,t') = -i\langle x_{\mathbf{k}}^{\dagger}(t') x_{\mathbf{k}}(t)\rangle, \tag{A.3}$$

which would be related to each other by fluctuation-dissipation relations, if the system was in thermal equilibrium. In our case only the excitons couple to the radiation field, which leads to quantum jump operators $L_{\mathbf{k}}$, linear in the exciton operators $x_{\mathbf{k}}$ and $x_{\mathbf{k}}^{\dagger}$. Consequently, dissipation can be treated to all orders simply by modifying the impurity propa-

gator. In the impurity limit $n_I = \sum_{\mathbf{r}} \langle x_{\mathbf{r}}^{\dagger} x_{\mathbf{r}} \rangle / V \approx 0$, this yields

$$\mathcal{G}^{>}(\omega, \mathbf{k}) = \frac{2i\Gamma(\mathbf{k})}{(\omega - \mathbf{k}^2/2M)^2 + \Gamma(\mathbf{k})^2}, \qquad \mathcal{G}^{<}(\omega, \mathbf{k}) = 0. \qquad (A.4)$$

Other quantities, such as the retarded response function $\mathcal{G}^R$, contain no additional information and are defined in terms of $\mathcal{G}^{\lessgtr}$ as usual:

$$\mathcal{G}^R(t, t') = \Theta(t - t') \left(\mathcal{G}^{>} - \mathcal{G}^{<} \right)(t, t'),$$
$$\mathcal{G}^{R/A}(\omega, \mathbf{k}) = \frac{1}{\omega - \mathbf{k}^2/2M \pm i\Gamma(\mathbf{k})}.$$

The electrons on the other hand are in thermal equilibrium and their correlation functions take the simpler form:

$$G_{\alpha}^{>}(\omega, \mathbf{k}) = -2\pi i \left(1 - n_F(\omega) \right) \delta(\omega - \mathbf{k}^2/2m - \varepsilon_{\alpha} + \varepsilon_F),$$
$$G_{\alpha}^{<}(\omega, \mathbf{k}) = 2\pi i \, n_F(\omega) \delta(\omega - \mathbf{k}^2/2m - \varepsilon_{\alpha} + \varepsilon_F),$$

where $n_F(\omega)$ is the Fermi-Dirac distribution function and $\alpha \in \{O, C\}$ labels the channel.

As before we can reconstruct the retarded fermion correlation function

$$G_{\alpha}^R(t, t') = \Theta(t - t') \left(G_{\alpha}^{>} - G_{\alpha}^{<} \right)(t, t'),$$

which takes a particularly simple form in frequency space:

$$G_{\alpha}^R(\omega, \mathbf{k}) = \frac{1}{\omega - \mathbf{k}^2/2m - \varepsilon_{\alpha} + i0^+}.$$

In our analysis we consider Fermions at zero temperature, which is a good approximation for solid state systems as they can be cooled down to milli-Kelvin temperatures. For experimentally typical electron densities $\geq 1 \times 10^{11}$, one can easily reach the regime where $k_B T \ll t, E_F, E_B^0$. That being said, studying the effects of finite temperature on Fermi polarons is an interesting prospect for future work.

Here we determine the T-matrix of Eq. (9) on a Keldysh contour, taking into account the ground state of the electrons. This will allow us to construct an approximate expression for the self energy. Although our nonequilibrium setting allows for additional correlations, the local-in-time structure of the interaction significantly restricts the number of independent components of the T-matrix [157]. In the end the T-matrix has the same causality structure as the propagators and can be expressed in terms of $T^{\lessgtr}(t, t')$. The diagrammatic structure remains the same as for the two-particle problem in Eq. (4) except that time arguments now live on a Keldysh contour
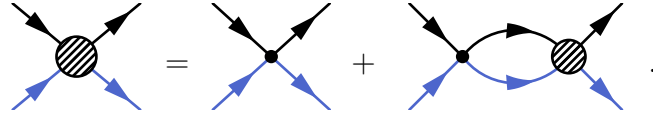

We use Langreth rules to decompose the above equation, which yields the following equations for the components of the T-matrix:

$$T_{\mathbf{k}}^{\lessgtr}(E) = U_{\Lambda} \left[K_{\mathbf{k}}^{\lessgtr}(E) T_{\mathbf{k}}^{A}(E) + K_{\mathbf{k}}^{R}(E) T_{\mathbf{k}}^{\lessgtr}(E) \right] \qquad = U_{\Lambda} \frac{K_{\mathbf{k}}^{\lessgtr}(E) T_{\mathbf{k}}^{A}(E)}{1 - K_{\mathbf{k}}^{R}(E)},$$

$$T_{\mathbf{k}}^{R/A}(E) = U_{\Lambda} \left[1 + K_{\mathbf{k}}^{R/A}(E) T_{\mathbf{k}}^{R/A}(E) \right] \qquad = U_{\Lambda} \frac{1}{1 - U_{\Lambda} K_{\mathbf{k}}^{R/A}(E)}, \qquad \text{where}$$

$$K_{\alpha\beta}^{\lessgtr}(t, \mathbf{x}) = -\mathcal{G}^{\lessgtr}(t, \mathbf{x}) G_{0,\alpha}^{\lessgtr}(t, \mathbf{x}) \delta_{\alpha\beta}, \quad \text{and} \quad K_{\alpha\beta}^{R/A}(t, \mathbf{x}) = \pm \Theta(\pm t) \left(K^{>} - K^{<} \right)_{\alpha\beta}(t, \mathbf{x}).$$
$$\text{(A.5)}$$

$\Theta(x)$ is the Heaviside step function and the kernels K can be explicitly computed as before. Eq. A.5 implies that $T^{<}(t, t') = 0$, as it is proportional to $G^{<}$. This is a consequence of the impurity limit, as $T^{<}$ is proportional to the density of molecules, which vanishes for a single exciton.

We now compute an approximate self energy of the exciton from the many body T-matrix.

Its form is given by the following Dyson equation
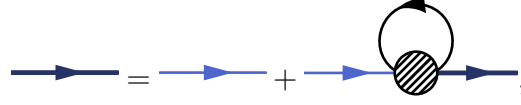
which encodes the following equations

$$\mathcal{G}^R(\omega, \mathbf{k}) = \mathcal{G}_0^R(\omega, \mathbf{k}) + \mathcal{G}_0^R(\omega, \mathbf{k}) \cdot \Sigma^R(\omega, \mathbf{k}) \cdot \mathcal{G}^R(\omega, \mathbf{k}),$$

$$\Sigma^R(\omega, \mathbf{k}) = -i \int \frac{d^2q}{(2\pi)^2} \frac{d\delta\omega}{2\pi} \text{Tr}\{T^R_{\mathbf{k}+\mathbf{q}}(\omega + \delta\omega) \cdot G_0^<(\delta\omega, \mathbf{q})\},$$

(A.6)

where the trace is performed over the two scattering channels. To obtain the second equation we have already assumed $T^<(\omega, \mathbf{k}) = 0$, as the number of molecules is negligible in the impurity limit.

B

Stabilizing Chiral Spin Liquids

B.1 Determining the effective Hubbard paramters

We derive the parameters of the Hubbard model from microscopic properties of the TMDs, following the procedure outlined in Ref. [44]. In the set-up discussed in the main text, holes in the two doped TMD layers feel a potential energy variation $V_M(\mathbf{r})$ which is well approximated by the lowest few harmonics $\{\mathbf{g}_j | j = 1, \dots, 6\}$ in the limit of small twist angles and reads:

$$V_M(\mathbf{r}) = \sum_{j=1}^{6} v_{\mathbf{g}_j} e^{i\mathbf{g}_j \cdot \mathbf{r}}. \tag{B.1}$$

The lowest harmonics of the potential are fully specified by $v_{\mathbf{g}_1} = v_0 e^{i\psi}$. In the low-doping limit, we approximate the valence band dispersion of the TMDs as parabolic and solve the corresponding Schrödinger equation to determine the Moire bands and Bloch functions $u_n(\mathbf{q})$. The hopping parameter t in the Hubbard model is determined by fitting a tight-
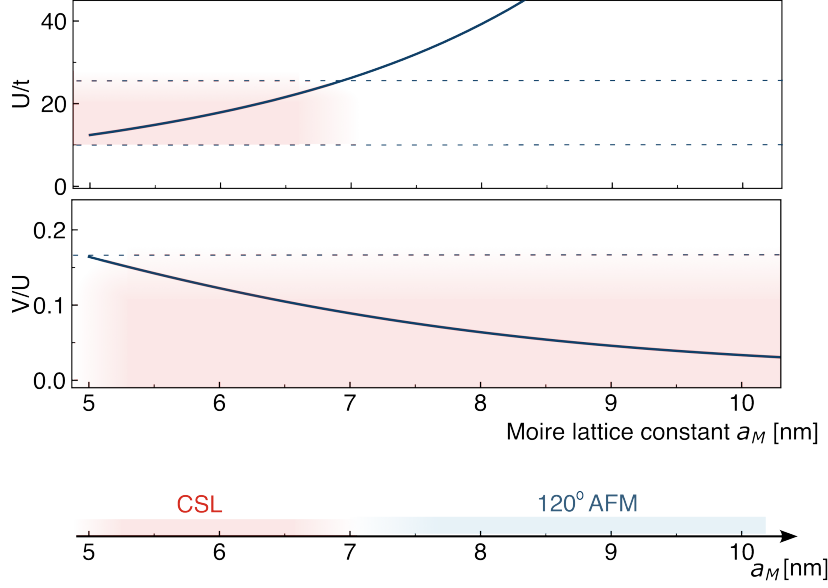
Figure B.1: Hubbard model parameters. U/t and V/U for a WSe$_2$ system as a function of lattice constant a_M, assuming $d = 2$nm, $\psi = -94°$ and $\varepsilon = 7$. Favorable regimes for the CSL are shaded in red. **Top:** Increasing a_M drives the system deeper into the Mott phase which eventually gives rise to a 120 degree magnet once J_H dominates indicated by the upper dashed line, while the system tends to form an integer quantum Hall state for $U/t \leq 10$, as confirmed by our numerical simulations. **Middle:** Nearest neighbor interactions are strongly suppressed for large a_M. We find that the CSL remains robust when $V/U \leq 1/6$ as indicated by the dashed line. **Bottom:** Resulting phase diagram of the $t - U - V$ Hubbard model, as a function of a_M. The CSL is stable in proximity to the Mott transition.

binding dispersion to the lowest-lying Moire band. We calculate the interaction parameter U by employing a projective construction [216, 217] to determine a complete set of localized Wannier functions for the lowest band $w_{\mathbf{R}_n}(\mathbf{r})$, where $\mathbf{R}_n$ labels the position of the unit cell. This yields

$$U = \int d^2\mathbf{x} \int d^2\mathbf{y} \, |w_{\mathbf{R}_n}(\mathbf{x})|^2 \, V_C(\mathbf{x} - \mathbf{y}) \, |w_{\mathbf{R}_n}(\mathbf{y})|^2, \tag{B.2}$$

and a similar expression for the strength of nearest-neighbor interactions

$$V = \int d^2\mathbf{x} \int d^2\mathbf{y} \, |w_{\mathbf{R}_n}(\mathbf{x})|^2 \, V_C(\mathbf{x} - \mathbf{y}) \, |w_{\mathbf{R}_{n+1}}(\mathbf{y})|^2. \tag{B.3}$$

Where we assume an electrostatic Coulomb potential

$$V_C(\mathbf{r}) = \frac{e^2}{4\pi\varepsilon}\left(\frac{1}{|\mathbf{r}|} - \frac{1}{\sqrt{\mathbf{r}^2 + 4d^2}}\right),$$ (B.4)

which takes into account the dielectric constant of the environment ε and that electrons induce mirror charges in a metallic gate separated by a distance d, which screens the Coulomb law down to dipolar interactions $V_D(\mathbf{r} \gg \mathbf{d}) \approx 2e^2 d^2 / 4\pi\varepsilon |\mathbf{r}|^3$ when their separation is much larger than the distance to the gate. Longer-range interaction terms beyond U and V can be neglected as they are strongly suppressed. For concreteness, we focus on a trilayer WSe$_2$/MoSe$_2$/WSe$_2$ setup in the following and assume a potential strength $v_0 \simeq 10$meV and $\psi = -94°$ as suggested by DFT calculations [44], although our results do not depend strongly on the precise values of v_0 and ψ, and apply qualitatively also to the other setups discussed in the main text. The functional dependence of U/t and V/U on the Moire lattice constant a_M is shown in Fig. B.1, for $d = 2$nm. For $U/t \gtrsim 25$ ($a_M \gtrsim 7$nm) the Heisenberg coupling dominates and the system forms a 120 degree state [218]. In the limit of small lattice constants, or larger twist angles, the system eventually forms an bilayer IQH state. For intermediate lattice constants our numerical analysis suggests the CSL is stable over a sizable regime even in the $t - U - V$ Hubbard model. We study the robustness of the CSL to perturbations in detail in the next-section.

B.2 Robustness of the CSL to perturbations

B.2.1 Nearest neighbor interactions

So far, we have discussed the ideal Hubbard model, described by t, U and Φ. Here, we show robustness of the observed CSL phases persists in the presence of nearest-neighbor interactions V, which are naturally present in 2D materials due to strong Coulomb repulsion. We therefore include repulsive terms in the Hamiltonian, which then reads:

$$\begin{aligned}\hat{H} = &- t \sum_{\langle ij\rangle, \sigma=\{T,B\}} e^{i\varphi_{ij}}\, c^\dagger_{i,\sigma} c_{j,\sigma} + \text{h.c.} + U \sum_i n_{i,T}\, n_{i,B} \\ &+ V \sum_{\langle ij\rangle} n_{i,T}n_{j,T} + n_{i,B}n_{j,B} + n_{i,T}n_{j,B} + n_{i,B}n_{j,T}.\end{aligned}$$ (B.5)
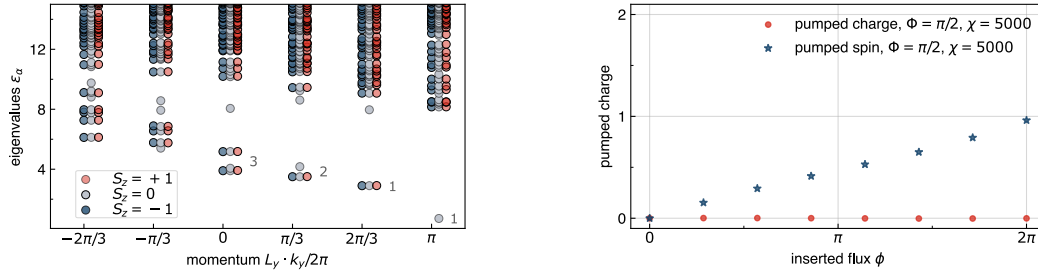
Figure B.2: Effect of nearest neighbor interactions $U/V = 6$ on the entanglement spectrum and charge pumping. For both panels $\Phi = \pi/2$ and $U = 17t$. Left panel: Entanglement spectrum for $\chi = 10000$. The symmetry-resolved spectrum and its degeneracies agree with the CSL prediction even for sizable nearest-neighbor interactions. Right panel: The system pumps an integer pseudo spin under flux insertion, confirming the topological nature of the spinon bands.

In the Mott insulating limit $U, V \gg t$, the nearest neighbor interactions indeed reduce the effective Heisenberg coupling in second-order degenerate perturbation theory

$$J_H = 2t^2/U \rightarrow 2t^2/(U - V), \tag{B.6}$$

which points to a destabilization of the CSL. To study the robustness of the spin-liquid phase, we determine the ground state of Eq. B.5 using iDMRG, with a conservative estimate of $U/V = 6$. For $U/t = 17$ this corresponds to physical parameters of $\varepsilon = 7, d = 2$nm, $v_0 = 6$meV and $\psi = -94$. Having assumed a constant value for U/V, we significantly overestimate V for smaller twist angles, where the plain Hubbard model is an excellent approximation, albeit overall energy gaps are suppressed by t/U. The phase diagram of the main text can be reproduced reliably if $U/V \geq 6$ and the topological features of the CSL can be recovered, as shown in Fig. B.2. Our analysis therefoer reveals a favorable experimental regime for the observation of spin liquid states at intermediate twist angles as highlighted in the bottom panel of Fig. B.1. We note that the CSL regime could be enhanced even further by engineering the dielectric environment to maximize electronic screening as commonly assumed in the literature [64, 65].

As a topologically ordered state, the chiral spin liquid is robust to any small perturbation. While symmetries are not essential ingredients for the CSL, the extent to which $SU(2)$ can be broken before the spin liquid is destabilized is not clear a priori. Although it can be electrostatically ensured that $\sum_i \langle S^z(i) \rangle = 0$, strain can induce hopping of different strengths in the two layers. The minimal model to study these perturbations is given by the following Hamiltonian:

$$\hat{H} = -\sum_{\langle ij \rangle} e^{i\varphi_{ij}} \, t_T c_{i,T}^{\dagger} c_{j,T} + t_B c_{i,B}^{\dagger} c_{j,B} + \text{h.c.} + U \sum_i n_{i,T} n_{i,B}, \tag{B.7}$$

where $t_{T(B)} = t \genfrac{}{}{0pt}{}{+}{(-)} \delta$ label the tunneling strengths in the top (bottom) layer. The IQH state is expected to be robust as the wavefunction is close to a direct product of the two layers. For the CSL, the situation is less clear, as the two layers are correlated due to interactions. We find the leading order correction to the effective spin model describing the CSL by performing a Schrieffer Wolff transformation, which yields the effective spin Hamiltonian:

$$\hat{H}_{eff} = 2\frac{t^2 + \delta^2}{U} \sum_{\langle ij \rangle} \mathbf{S}_i \cdot \mathbf{S}_j + 4\frac{\delta^2}{U} \sum_{\langle ij \rangle} S_i^z S_j^z + \mathcal{O}(\frac{t^3}{U^2}, \frac{\delta^3}{U^2}), \tag{B.8}$$

where chemical potential terms of the form $\sim t\frac{\delta}{U}(n_T - n_B)$ have already been compensated by external electric fields. $SU(2)$ breaking terms only appear at order $\mathcal{O}(\delta^2/U)$ which introduce some anisotropy. This is in accordance with the result of our DMRG simulations for $\delta = 0.1t$ and a flux of $\Phi = \pi/2$, which find very similar phase boundaries, as shown in Fig. B.3 a). The entanglement spectra shown in Fig. B.3 b), clearly show well-defined chiral edge modes that match the expected counting rules of the Chern insulator and the CSL as discussed in the main text. Due to the topological protection of the quantized Hall response, the edge theory remains well-defined and retains its $SU(2)$ multiplets even for sizable perturbations δ.
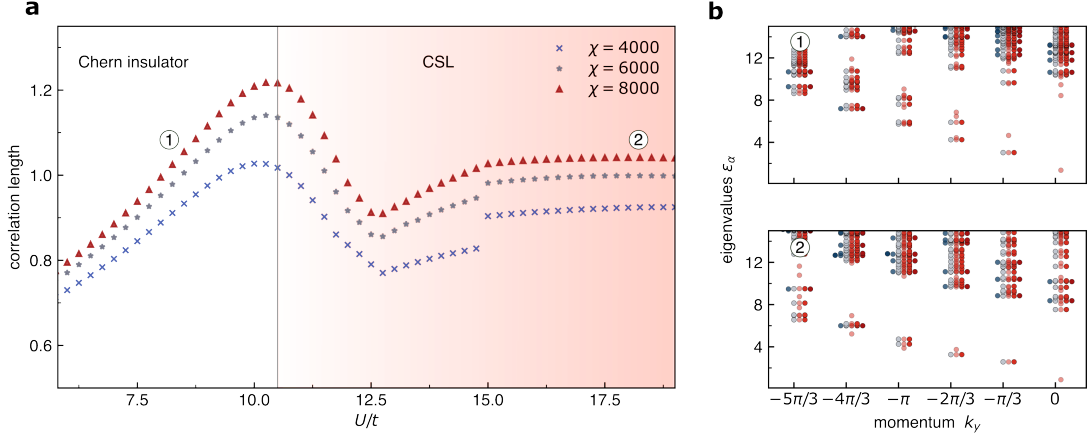
Figure B.3: Triangular lattice Hubbard model with broken $SU(2)$ symmetry. Ground state properties of the triangular lattice Hubbard model for $\delta = 0.1$ at $\Phi = \pi/2$ flux on an infinite cylinder with $L_y = 6$. **(a)** Ground state correlation length in the charge sector $(S_z, Q) = (0, 0)$. As for the $SU(2)$-symmetric model, the correlation length is enhanced around $U/t \simeq 10.5$. **(b)**. Panel 1 and 2 show the ground state entanglement spectrum for $\chi = 10000$ and charge $Q = 0$ at small and large U/t, respectively. We find the characteristic eigenstate countings of a $\nu = 2$ Chern insulator and the CSL. The degenerate $SU(2)$ multiplets remain well-defined on the edge, although the underlying Hubbard model is no longer symmetric.

B.3 Gauge choice for different flux values

To implement a static magnetic field on the triangular lattice we perform a Peierls substitution $t_{ij} \to t_{ij} e^{i\varphi_{ij}}$, where the choice of phases φ_{ij} is not unique. To accommodate for the $\Phi = \pi/2, \pi/3$ flux per triangle and to keep translational invariance in y direction, we perform our simulations on unit cells of size $L_x = 2, 3$. In the main text we chose gauges leading to the phase patterns shown in Fig. B.4. As any gauge choice breaks explicit translational invariance, we work with unit cells and cylinder geometries which are commensurate with the flux.

Remarkably, for $\Phi = \pi/2$, the half-filled Hubbard model has a particle-hole symmetry, meaning that the Hamiltonian is invariant under the transformation

$$
\begin{aligned}
c_{i,\sigma}^\dagger &\to c_{i,\bar\sigma} \\
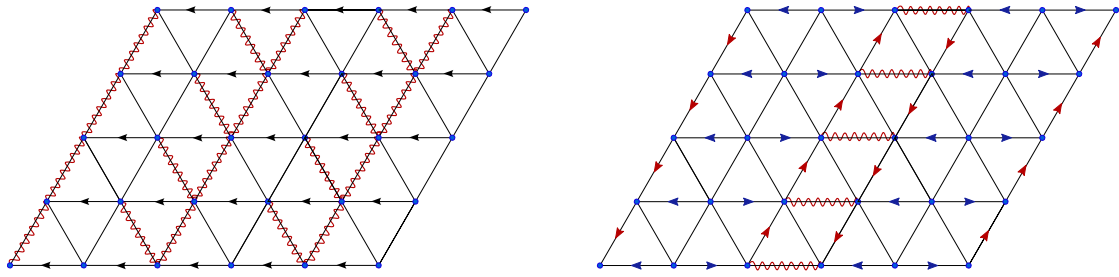c_{i,\sigma} &\to c_{i,\bar\sigma}^\dagger,
\end{aligned}
\tag{B.9}
$$

Figure B.4: Gauge choices for different fluxes. Flux patterns on the triangular lattice leading to $\Phi = \pi/2$ **(a)** and $\Phi = \pi/3$ **(b)**. Hopping along a bond in the direction of a red (blue) arrow yields a phase factor of $e^{i2\pi/3}$ ($e^{i\pi/3}$), while hopping along a black arrow yields a phase of $e^{i\pi/2}$. Squiggly bonds carry a factor of -1.

followed by complex conjugation of all hopping elements. This is surprising, as the triangular lattice is not bipartite, which spoils particle hole symmetry in the absence of magnetic fields, as can be easily seen from the asymmetric single-electron dispersion. At $\Phi = \pi/2$, however, the flux pattern is mapped to a gauge-equivalent configuration, as shown in Fig. B.5. This simple physical observation imposes important constraints on the quantum Phase transition in the Hubbard model: The continuum field theory describing the critical point must be symmetric under a combined $\mathcal{T} \cdot \mathcal{C}$ transformation and therefore has Lorentz symmetry. Note that this does not hold for other fluxes such as $\Phi = \pi/3$ as the particle hole transformation maps this to a pattern with $\tilde{\Phi} = 4\pi/3$ per triangle, however it may still emerge close to a quantum critical point.
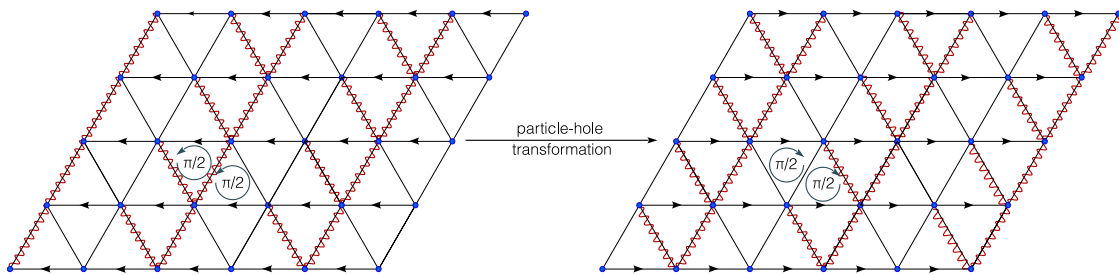

Figure B.5: Extended particle-hole symmetry at $\Phi = \pi/2$. Exchanging particle and hole operators changes the flux pattern from $\pi/2$ flux per triangle (left) to a pattern with $-\pi/2$ flux per triangle (right). A subsequent conjugation of the hopping matrix maps the second-quantized Hamiltonian back to a (gauge-equivalent) version of itself.

B.4 Ground state crossing for $\Phi = \pi/3$

We can reliably prepare states in the $k_y = \pi$ and $k_y = 0$ sectors on the $L_x = 3$ unit cell and flux $\Phi = \pi/3$. As discussed in the main text, the two ground states of the CSL sectors lie at $k_y = 0, \pi$ but are slightly split due to finite size effects. Therefore, in our truncated system the transition from the Hall states to the CSL occurs in two steps: First the correlation length in the $k_y = \pi$ sector diverges and shortly thereafter its energy crosses with the $k_y = 0$ state and becomes the true finite-size ground state. We show the difference in ground state energies as a function of interaction strength and bond dimension in Fig. B.6. We find that the crossing takes places around $U \sim 8.75t$, where the correlation length of the $k_y = \pi$ state is still very large, as discussed in the main text.
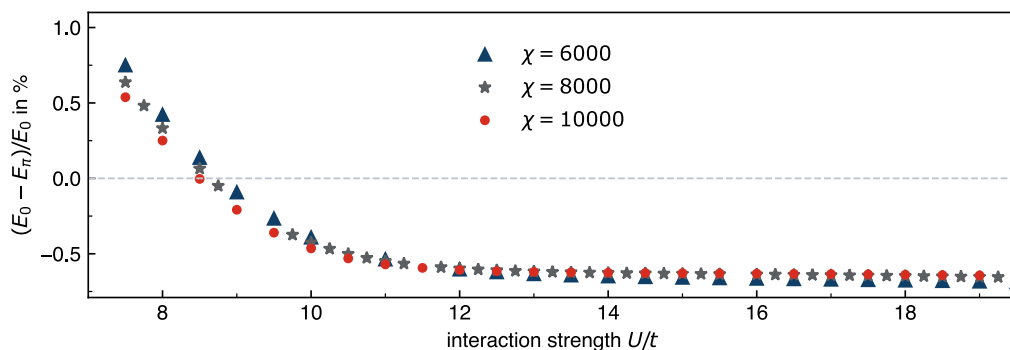
Figure B.6: **Energy difference of the lowest lying** $k_y = 0$ **and** $k_y = \pi$ **states for** $\Phi = \pi/3$. We find that for $U \simeq 8.5t$ the ground-state energies of the two momentum sectors cross. This point moves to weaker interactions as the bond dimension increases. This level crossing occurs in the vicinity of the enhanced correlation length observed in the main text. We expect that in the CSL phase both eigenstates are degenerate in the thermodynamic limit.

B.5 Characterizing the phases for $\Phi = \pi/3$

While the precise value of the flux is important in the Hofstadter regime, as it determines the filling of the Chern bands, in the Mott insulating limit it simply controls the strength of the chiral spin term J_χ. Therefore, we generically expect chiral spin liquids to appear in the Mott insulator, as long as $J_\chi \sim \sin(\Phi)$ is large enough. Here we discuss the fate of the

Mott insulator for $\Phi = \pi/3$, which corresponds to a filling of $\nu_T = 3$. Following the

Figure B.7: Entanglement spectrum and charge pumping for $\Phi = \pi/3$ and $U = 15t$. Left panel: Entanglement spectrum for $\chi = 10000$. The symmetry resolved spectrum and its degeneracies agree with the $SU(2)_1$ WZW edge theory of the CSL. Right panel: The system pumps an integer pseudo spin under flux insertion, confirming the topological nature of the spinon bands.
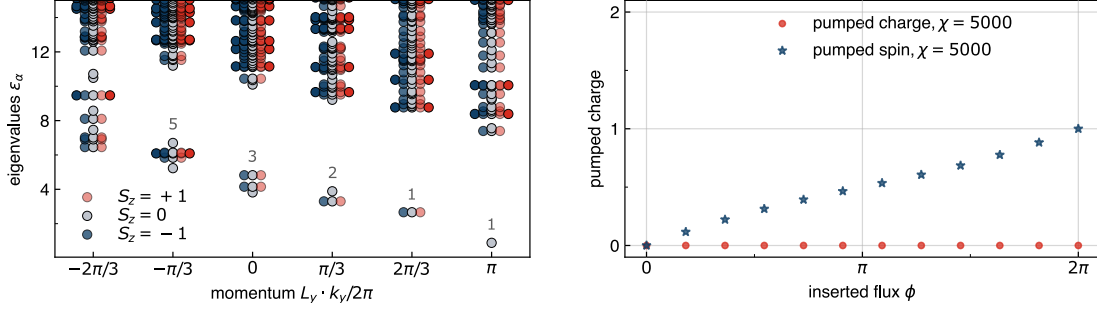
analysis done for $\Phi = \pi/2$ in the main text, we compute the entanglement spectrum and analyze the pumped charges under flux insertion. Our results in the Mott limit are shown in Fig. B.7 for $U = 15t$. The entanglement spectrum agrees with the spectrum of the $SU(2)_1$ WZW model describing the spin-density-wave excitations on the edge (left panel). The absence of gapless density-wave excitations, in addition to the vanishing pumped charge under the insertion of real magnetic flux (right panel) indicates that charges are frozen and hence that the state is insulating. Under the insertion of opposite fluxes in the two layers, i.e., when coupling to charge-neutral, spin excitations, we find a fractional spin Hall effect, as discussed in the main text [176, 41]. As expected, no charge is pumped under the insertion of opposite fluxes, and no spin is pumped under symmetric flux insertion (not shown). Hence, the state describes a CSL. These results demonstrate that the CSL is a generic feature of the Hofstadter-Hubbard model at strong coupling independent of the specific values of the magnetic field.

The fate of the Hofstadter states in the presence of weak interactions is a priori not obvious. For $\Phi = \pi/3$, we find that the system no longer exhibits quantized charge or spin pumping in the charge-liquid regime. To study the propensity of the state to develop long range order, we analyze spin, density and superconducting correlation functions, which are shown in Fig. B.8. The formation of excitonic insulators and other layer-spin ordered states is ruled out, as we find exponentially decaying spin correlations, see Fig. B.8 a). Similarly, density correlations show an initial exponential decay before saturating at a weak residual value of
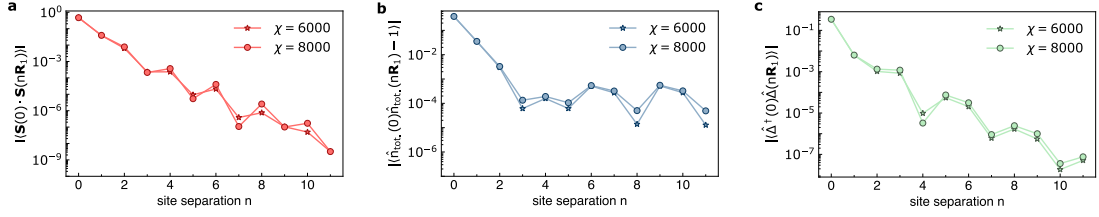
Figure B.8: Correlations in the weakly interacting phase for $\Phi = \pi/3$. Correlation functions are plotted for $U/t = 3$ as a function of distance along the x-direction. **a)** Spin-correlations are exponentially decaying, showing the absence of long-range spin order. **b)** Density correlations show an initial exponential decay and a weak residual tendency to form charge order. **c)** Superconducting correlations are small and decay exponentially. This indicates that the state may be a featureless Hall state.

$\approx 10^{-4}$, which indicates weak charge order, shown in Fig. B.8 b). Since this value is very small and the circumference of the cylinder is finite, we attribute this to finite size effects.

In the absence of magnetic fields, superconductivity has been discussed as a possible phase in the triangular Hubbard model [219]. The tendency to become superconducting is captured by pairing terms of the form: $\hat{\Delta}(x,y) = (c^\dagger_{T,x,y+1} c^\dagger_{B,x,y} - c^\dagger_{B,x,y+1} c^\dagger_{T,x,y})/\sqrt{2}$ and the corresponding correlation functions are depicted in Fig. B.8 c). This shows that correlations decay exponentially and we do not find signatures of superconducting order. Our analysis therefore suggests that the $\Phi = \pi/3$ state in the half-filled triangular lattice is consistent with a featureless Hall state.

B.6   Probing the other sectors of the CSL

In the fermionic system, the two topological ground states of the CSL carry momentum $k_y = 0$ and $k_y = \pi$. Due to finite size effects these states are not perfectly degenerate [178, 41]. We prepare these states in our iDMRG simulations by initializing them with product states carrying π momentum in the y-direction. We show the entanglement spectra of the resulting ground states in Fig. B.9. As for the trivial sector, we observe a clear separation between bulk and edge modes and the number of dominant eigenvalues in each spin sector continues to follow the $(1,1,2,3,...)$ counting rule. The lowest lying states of the $SU(2)_1$ algebra are now doubly degenerate and are part of a spin $1/2$ representation rather than a
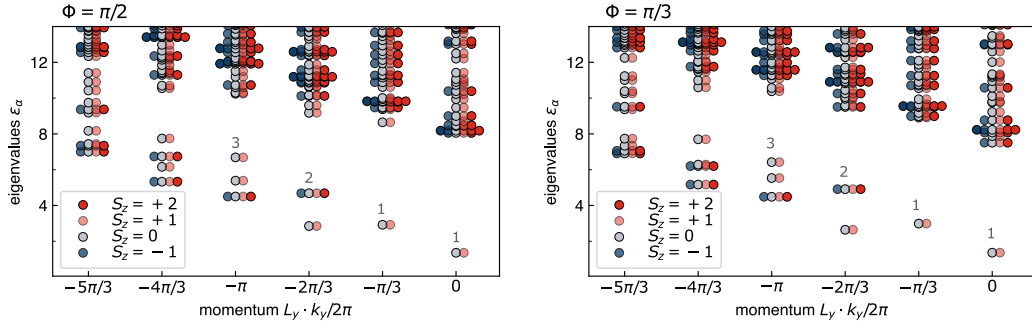
Figure B.9: Entanglement spectra in the semion sector. Entanglement spectra in the CSL phase for $U = 15t$ and $\chi = 10000$. For both $\Phi = \pi/2$ (left panel) and $\Phi = \pi/3$ (right panel) the entanglement spectra obey the (1,1,2,3,5,...) counting rule for the edge theory of the CSL. In contrast to the trivial sector, the lowest lying state is now part of a spin $1/2$ representation.

singlet, see Fig. B.9. We remark that instead of preparing finite momentum states via the initial conditions, the two sectors can also be interchanged by threading magnetic flux through the cylinder.

6

Conclusion

We conclude by briefly reviewing the results of the research presented in this thesis and presenting potential future directions.

We began by developing novel optical probes to revisit the long-standing problem of electronic crystallization transitions. To this end we provide a theory for Bragg scattering of optically induced impurities off the electronic lattice. The resulting optical response of the system is directly tied to the electronic charge order. In subsequent collaborations with experiments, we utilized this effect to unveil the formation of Wigner crystals in monolayers of atomically thin semiconductors. We have also demonstrated theoretically and experimentally that collective excitations of quantum Hall states can be probed, which herald the formation of charge order and signal strong correlations. In the future it will be interesting to apply this tool-box to study correlations in fractional quantum Hall states as well as exotic intermediate phases which shield the direct liquid-to-solid phase transition. Remarkably, at the time of writing this thesis, there are already reported advancements in the exploration of

the latter direction [122].

Inspired by the apparent similarity between ultra-cold atomic gases and two dimensional materials, we developed a theory of perfectly two dimensional Feshbach resonances. This mechanism allows us to control interactions among quasi-particles in the solid state simply by changing external electric fields. These predictions were subsequently observed experimentally, where it was possible to strongly couple a dilute concentration of excitons to a Fermi sea of holes. We modelled the experiments by using non-equilibrium field theory to account for recombination of the excitons. In principle our theory can be applied just as well to long-lived bosonic quasi-particles, allowing for the formation of true equilibrium states with tunable interactions [165, 220]. An exciting direction will be to modify electronic transport and engineer pairing instabilities in degenerate Bose-Fermi mixtures. Furthermore, some aspects of the developed scattering theory may apply also to completely distinct systems, which are just starting to be explored [221, 222].

Finally we showed how exotic topological order can appear in the triangular lattice Hubbard model, assuming strong external magnetic fields. In this limit, strong correlations among electrons give rise to a particularly robust chiral spin liquid phase appears. While this regime of the Hubbard model is out of reach for conventional solids, a natural platform in two dimensional materials is discussed. Crucially this allows for new optical and more direct probes of topological order as well as its phase transitions. We also propose theories for the phase transitions, which suggest physically transparent ways in which topological order is formed and destroyed. Looking forward, it will be interesting to study these critical theories in more detail to see if their signatures, such as the emergence of spin-roton modes, can be observed experimentally. Furthermore, a generalization of our setup to non-abelian spin liquids is conceivable.

References

[1] L D Landau. 29 - on the theory of phase transitions. In D. TER HAAR, editor, *Collected Papers of L.D. Landau*, pages 193–216. Pergamon, 1965.

[2] P. C. Hohenberg and B. I. Halperin. Theory of dynamic critical phenomena. *Rev. Mod. Phys.*, 49:435–479, Jul 1977.

[3] Subir Sachdev. *Quantum Phase Transitions*. Cambridge University Press, 2 edition, 2011.

[4] D. C. Tsui, H. L. Stormer, and A. C. Gossard. Two-dimensional magnetotransport in the extreme quantum limit. *Phys. Rev. Lett.*, 48:1559–1562, May 1982.

[5] Nathan Seiberg, T. Senthil, Chong Wang, and Edward Witten. A duality web in 2+1 dimensions and condensed matter physics. *Annals of Physics*, 374:395–433, 2016.

[6] X. G. Wen and Q. Niu. Ground-state degeneracy of the fractional quantum hall states in the presence of a random potential and on high-genus riemann surfaces. *Phys. Rev. B*, 41:9377–9396, May 1990.

[7] Xie Chen, Zheng-Cheng Gu, and Xiao-Gang Wen. Local unitary transformation, long-range quantum entanglement, wave function renormalization, and topological order. *Phys. Rev. B*, 82:155138, Oct 2010.

[8] Michael Levin and Xiao-Gang Wen. Detecting topological order in a ground state wave function. *Phys. Rev. Lett.*, 96:110405, Mar 2006.

[9] Alexei Kitaev and John Preskill. Topological entanglement entropy. *Phys. Rev. Lett.*, 96:110404, Mar 2006.

[10] A.Yu. Kitaev. Fault-tolerant quantum computation by anyons. *Annals of Physics*, 303(1):2–30, 2003.

[11] Lucile Savary and Leon Balents. Quantum spin liquids: a review. *Reports on Progress in Physics*, 80(1):016502, nov 2016.

[12] J. Knolle and R. Moessner. A field guide to spin liquids. *Annual Review of Condensed Matter Physics*, 10(1):451–472, 2019.

[13] B. Spivak, S. V. Kravchenko, S. A. Kivelson, and X. P. A. Gao. Colloquium: Transport in strongly correlated two dimensional electron fluids. *Rev. Mod. Phys.*, 82:1743–1766, May 2010.

[14] Masatoshi Imada, Atsushi Fujimori, and Yoshinori Tokura. Metal-insulator transitions. *Rev. Mod. Phys.*, 70:1039–1263, Oct 1998.

[15] B. Keimer, S. A. Kivelson, M. R. Norman, S. Uchida, and J. Zaanen. From quantum matter to high-temperature superconductivity in copper oxides. *Nature*, 518(7538):179–186, 2015.

[16] Christian Gross and Immanuel Bloch. Quantum simulations with ultracold atoms in optical lattices. *Science*, 357(6355):995–1001, 2017.

[17] Manuel Endres, Hannes Bernien, Alexander Keesling, Harry Levine, Eric R. Anschuetz, Alexandre Krajenbrink, Crystal Senko, Vladan Vuletic, Markus Greiner, and Mikhail D. Lukin. Atom-by-atom assembly of defect-free one-dimensional cold atom arrays. *Science*, 354(6315):1024–1027, 2016.

[18] Morten Kjaergaard, Mollie E. Schwartz, Jochen Braumüller, Philip Krantz, Joel I.-J. Wang, Simon Gustavsson, and William D. Oliver. Superconducting qubits: Current state of play. *Annual Review of Condensed Matter Physics*, 11(1):369–395, 2020.

[19] Colin D. Bruzewicz, John Chiaverini, Robert McConnell, and Jeremy M. Sage. Trapped-ion quantum computing: Progress and challenges. *Applied Physics Reviews*, 6(2):021314, 05 2019.

[20] A. K. Geim and I. V. Grigorieva. Van der waals heterostructures. *Nature*, 499(7459):419–425, 2013.

[21] Yuan Cao, Valla Fatemi, Shiang Fang, Kenji Watanabe, Takashi Taniguchi, Efthimios Kaxiras, and Pablo Jarillo-Herrero. Unconventional superconductivity in magic-angle graphene superlattices. *Nature*, 556(7699):43–50, 2018.

[22] Yanhao Tang, Lizhong Li, Tingxin Li, Yang Xu, Song Liu, Katayun Barmak, Kenji Watanabe, Takashi Taniguchi, Allan H. MacDonald, Jie Shan, and Kin Fai Mak. Simulation of Hubbard model physics in WSe2/WS2 moiré superlattices. *Nature*, 579(7799):353–358, 2020.

[23] G. Semeghini, H. Levine, A. Keesling, S. Ebadi, T. T. Wang, D. Bluvstein, R. Verresen, H. Pichler, M. Kalinowski, R. Samajdar, A. Omran, S. Sachdev, A. Vishwanath, M. Greiner, V. Vuletić, and M. D. Lukin. Probing topological spin liquids on a programmable quantum simulator. *Science*, 374(6572):1242–1247, 2021.

[24] K. J. Satzinger, Y.-J Liu, A. Smith, C. Knapp, M. Newman, C. Jones, Z. Chen, C. Quintana, X. Mi, A. Dunsworth, C. Gidney, I. Aleiner, F. Arute, K. Arya, J. Atalaya, R. Babbush, J. C. Bardin, R. Barends, J. Basso, A. Bengtsson, A. Bilmes, M. Broughton, B. B. Buckley, D. A. Buell, B. Burkett, N. Bushnell, B. Chiaro, R. Collins, W. Courtney, S. Demura, A. R. Derk, D. Eppens, C. Erickson, L. Faoro, E. Farhi, A. G. Fowler, B. Foxen, M. Giustina, A. Greene, J. A. Gross, M. P. Harrigan, S. D. Harrington, J. Hilton, S. Hong, T. Huang, W. J. Huggins, L. B. Ioffe, S. V. Isakov, E. Jeffrey, Z. Jiang, D. Kafri, K. Kechedzhi, T. Khattar, S. Kim, P. V. Klimov, A. N. Korotkov, F. Kostritsa, D. Landhuis, P. Laptev, A. Locharla, E. Lucero, O. Martin, J. R. McClean, M. McEwen, K. C. Miao, M. Mohseni, S. Montazeri, W. Mruczkiewicz, J. Mutus, O. Naaman, M. Neeley, C. Neill, M. Y. Niu, T. E. O'Brien, A. Opremcak, B. Pató, A. Petukhov, N. C. Rubin, D. Sank, V. Shvarts, D. Strain, M. Szalay, B. Villalonga, T. C. White, Z. Yao, P. Yeh, J. Yoo, A. Zalcman, H. Neven, S. Boixo, A. Megrant, Y. Chen, J. Kelly, V. Smelyanskiy, A. Kitaev, M. Knap, F. Pollmann, and P. Roushan. Realizing topologically ordered states on a quantum processor. *Science*, 374(6572):1237–1241, 2021.

[25] Subir Sachdev. *Quantum Phases of Matter*. Cambridge University Press, 2023.

[26] E. Wigner. On the Interaction of Electrons in Metals. *Physical Review*, 46(11):1002–1011, dec 1934.

[27] N. D. Drummond and R. J. Needs. Phase diagram of the low-density two-dimensional homogeneous electron gas. *Phys. Rev. Lett.*, 102:126402, Mar 2009.

[28] W. L. McMillan. Landau theory of charge-density waves in transition-metal dichalcogenides. *Phys. Rev. B*, 12:1187–1196, Aug 1975.

[29] S. Alexander and J. McTague. Should all crystals be bcc? landau theory of solidification and crystal nucleation. *Phys. Rev. Lett.*, 41:702–705, Sep 1978.

[30] Boris Spivak and Steven A. Kivelson. Phases intermediate between a two-dimensional electron liquid and wigner crystal. *Phys. Rev. B*, 70:155114, Oct 2004.

[31] Reza Jamei, Steven Kivelson, and Boris Spivak. Universal aspects of coulomb-frustrated phase separation. *Phys. Rev. Lett.*, 94:056805, Feb 2005.

[32] M. Roger. Multiple exchange in ^{3}He and in the wigner solid. *Phys. Rev. B*, 30:6432–6457, Dec 1984.

[33] G. Misguich, B. Bernu, C. Lhuillier, and C. Waldtmann. Spin liquid in the multiple-spin exchange model on the triangular lattice: ^{3}He on graphite. *Phys. Rev. Lett.*, 81:1098–1101, Aug 1998.

[34] J. Knörzer, M. J. A. Schuetz, G. Giedke, D. S. Wild, K. De Greve, R. Schmidt, M. D. Lukin, and J. I. Cirac. Wigner crystals in two-dimensional transition-metal dichalcogenides: Spin physics and readout. *Physical Review B*, 101(12):125101, mar 2020.

[35] John Hubbard. Electron correlations in narrow energy bands. *Proceedings of the Royal Society of London. Series A. Mathematical and Physical Sciences*, 276:238–257, 1963.

[36] A. H. MacDonald, S. M. Girvin, and D. Yoshioka. $\frac{t}{U}$ expansion for the hubbard model. *Phys. Rev. B*, 37:9753–9756, Jun 1988.

[37] T. Senthil. Theory of a continuous mott transition in two dimensions. *Phys. Rev. B*, 78:045109, Jul 2008.

[38] J. G. Bednorz and K. A. Müller. Possible hightc superconductivity in the ba−la−cu−o system. *Zeitschrift für Physik B Condensed Matter*, 64(2):189–193, 1986.

[39] P. W. Anderson. The resonating valence bond state in la$_2$cuo$_4$ and superconductivity. *Science*, 235(4793):1196–1198, 1987.

[40] Patrick A. Lee, Naoto Nagaosa, and Xiao-Gang Wen. Doping a mott insulator: Physics of high-temperature superconductivity. *Rev. Mod. Phys.*, 78:17–85, Jan 2006.

[41] Aaron Szasz, Johannes Motruk, Michael P. Zaletel, and Joel E. Moore. Chiral spin liquid phase of the triangular lattice hubbard model: A density matrix renormalization group study. *Phys. Rev. X*, 10:021042, May 2020.

[42] Mingpu Qin, Chia-Min Chung, Hao Shi, Ettore Vitali, Claudius Hubig, Ulrich Schollwöck, Steven R. White, and Shiwei Zhang. Absence of superconductivity in the pure two-dimensional hubbard model. *Phys. Rev. X*, 10:031016, Jul 2020.

[43] Immanuel Bloch, Jean Dalibard, and Wilhelm Zwerger. Many-body physics with ultracold gases. *Rev. Mod. Phys.*, 80:885–964, Jul 2008.

[44] Fengcheng Wu, Timothy Lovorn, Emanuel Tutuc, and A. H. MacDonald. Hubbard model physics in transition metal dichalcogenide moiré bands. *Phys. Rev. Lett.*, 121:026402, Jul 2018.

[45] Christie S. Chiu, Geoffrey Ji, Annabelle Bohrdt, Muqing Xu, Michael Knap, Eugene Demler, Fabian Grusdt, Markus Greiner, and Daniel Greif. String patterns in the doped hubbard model. *Science*, 365(6450):251–256, 2019.

[46] Tingxin Li, Shengwei Jiang, Lizhong Li, Yang Zhang, Kaifei Kang, Jiacheng Zhu, Kenji Watanabe, Takashi Taniguchi, Debanjan Chowdhury, Liang Fu, Jie Shan, and Kin Fai Mak. Continuous mott transition in semiconductor moirésuperlattices. *Nature*, 597(7876):350–354, 2021.

[47] Yuya Shimazaki, Ido Schwartz, Kenji Watanabe, Takashi Taniguchi, Martin Kroner, and Ataç Imamoğlu. Strongly correlated electrons and hybrid excitons in a moiré heterostructure. *Nature*, 580(7804):472–477, 2020.

[48] Emma C. Regan, Danqing Wang, Chenhao Jin, M. Iqbal Bakti Utama, Beini Gao, Xin Wei, Sihan Zhao, Wenyu Zhao, Zuocheng Zhang, Kentaro Yumigeta, Mark Blei, Johan D. Carlström, Kenji Watanabe, Takashi Taniguchi, Sefaattin Tongay, Michael Crommie, Alex Zettl, and Feng Wang. Mott and generalized Wigner crystal states in WSe2/WS2 moiré superlattices. *Nature*, 579(7799):359–363, 2020.

[49] Gui-Bin Liu, Di Xiao, Yugui Yao, Xiaodong Xu, and Wang Yao. Electronic structures and theoretical modelling of two-dimensional group-vib transition metal dichalcogenides. *Chem. Soc. Rev.*, 44:2643–2663, 2015.

[50] Andor Kormányos, Guido Burkard, Martin Gmitra, Jaroslav Fabian, Viktor Zólyomi, Neil D Drummond, and Vladimir Fal'ko. k·p theory for two-dimensional transition metal dichalcogenide semiconductors. *2D Materials*, 2(2):022001, apr 2015.

[51] Christian Fey, Peter Schmelcher, Atac Imamoglu, and Richard Schmidt. Theory of exciton-electron scattering in atomically thin semiconductors. *Phys. Rev. B*, 101:195417, May 2020.

[52] P. W. Anderson. Infrared catastrophe in fermi gases with local scattering potentials. *Phys. Rev. Lett.*, 18:1049–1051, Jun 1967.

[53] P. NOZIÈRES and C. T. DE DOMINICIS. Singularities in the x-ray absorption and emission of metals. iii. one-body theory exact solution. *Phys. Rev.*, 178:1097–1107, Feb 1969.

[54] Joannis Koepsell, Dominik Bourgund, Pimonpan Sompet, Sarah Hirthe, Annabelle Bohrdt, Yao Wang, Fabian Grusdt, Eugene Demler, Guillaume Salomon, Christian Gross, and Immanuel Bloch. Microscopic evolution of doped mott insulators from polaronic metal to fermi liquid. *Science*, 374(6563):82–86, 2021.

[55] N. Darkwah Oppong, L. Riegger, O. Bettermann, M. Höfer, J. Levinsen, M. M. Parish, I. Bloch, and S. Fölling. Observation of coherent multiorbital polarons in a two-dimensional fermi gas. *Phys. Rev. Lett.*, 122:193604, May 2019.

[56] Zoe Z. Yan, Yiqi Ni, Carsten Robens, and Martin W. Zwierlein. Bose polarons near quantum criticality. *Science*, 368(6487):190–194, 2020.

[57] Meinrad Sidler, Patrick Back, Ovidiu Cotlet, Ajit Srivastava, Thomas Fink, Martin Kroner, Eugene Demler, and Atac Imamoglu. Fermi polaron-polaritons in charge-tunable atomically thin semiconductors. *Nature Physics*, 13(3):255–261, 2017.

[58] Lukas Homeier, Pit Bermes, and Fabian Grusdt. Scattering theory of mesons in doped antiferromagnetic mott insulators: Multichannel perspective and feshbach resonance, 2023.

[59] Ido Schwartz, Yuya Shimazaki, Clemens Kuhlenkamp, Kenji Watanabe, Takashi Taniguchi, Martin Kroner, and Ataç Imamoğlu. Electrically tunable feshbach resonances in twisted bilayer semiconductors. *Science*, 374(6565):336–340, 2021.

[60] F. Chevy. Universal phase diagram of a strongly interacting fermi gas with unbalanced spin populations. *Phys. Rev. A*, 74:063628, Dec 2006.

[61] Hoi Chun Po, Liujun Zou, T. Senthil, and Ashvin Vishwanath. Faithful tight-binding models and fragile topology of magic-angle bilayer graphene. *Phys. Rev. B*, 99:195455, May 2019.

[62] Nicolás Morales-Durán, Nai Chao Hu, Pawel Potasz, and Allan H. MacDonald. Nonlocal interactions in moiré hubbard systems. *Phys. Rev. Lett.*, 128:217202, May 2022.

[63] Tingxin Li, Shengwei Jiang, Lizhong Li, Yang Zhang, Kaifei Kang, Jiacheng Zhu, Kenji Watanabe, Takashi Taniguchi, Debanjan Chowdhury, Liang Fu, Jie Shan, and Kin Fai Mak. Continuous mott transition in semiconductor moirésuperlattices. *Nature*, 597(7876):350–354, 2021.

[64] Ya-Hui Zhang, D. N. Sheng, and Ashvin Vishwanath. Su(4) chiral spin liquid, exciton supersolid, and electric detection in moiré bilayers. *Phys. Rev. Lett.*, 127:247701, Dec 2021.

[65] Yiqing Zhou, D. N. Sheng, and Eun-Ah Kim. Quantum phases of transition metal dichalcogenide moiré systems. *Phys. Rev. Lett.*, 128:157602, Apr 2022.

[66] L. Ciorciaro, T. Smoleński, I. Morera, N. Kiper, S. Hiestand, M. Kroner, Y. Zhang, K. Watanabe, T. Taniguchi, E. Demler, and A. İmamoğlu. Kinetic magnetism in triangular moirématerials. *Nature*, 623(7987):509–513, 2023.

[67] Yu. E. Lozovik and V. I. Yudson. Crystallization of a two-dimensional electron gas in a magnetic field. *ZhETF Lett.*, 22:26, July 1975.

[68] C. C. Grimes and G. Adams. Evidence for a liquid-to-crystal phase transition in a classical, two-dimensional sheet of electrons. *Phys. Rev. Lett.*, 42:795–798, 1979.

[69] E. Y. Andrei, G. Deville, D. C. Glattli, F. I. B. Williams, E. Paris, and B. Etienne. Observation of a magnetically induced wigner solid. *Phys. Rev. Lett.*, 60:2765–2768, Jun 1988.

[70] V. J. Goldman, M Santos, M Shayegan, and J. E. Cunningham. Evidence for two-dimentional quantum wigner crystal. *Phys. Rev. Lett.*, 65:2189–2192, Oct 1990.

[71] F. I. B. Williams, P. A. Wright, R. G. Clark, E. Y. Andrei, G. Deville, D. C. Glattli, O. Probst, B. Etienne, C. Dorin, C. T. Foxon, and J. J. Harris. Conduction threshold and pinning frequency of magnetically induced wigner solid. *Phys. Rev. Lett.*, 66:3285–3288, 1991.

[72] H. Buhmann, W. Joss, K. von Klitzing, I. V. Kukushkin, A. S. Plaut, G. Martinez, K. Ploog, and V. B. Timofeev. Novel magneto-optical behavior in the wigner-solid regime. *Phys. Rev. Lett.*, 66:926–929, Feb 1991.

[73] E. M. Goldys, S. A. Brown, R. B. Dunford, A. G. Davies, R. Newbury, R. G. Clark, P. E. Simmonds, J. J. Harris, and C. T. Foxon. Magneto-optical probe of two-dimensional electron liquid and solid phases. *Phys. Rev. B*, 46:7957–7960, Sep 1992.

[74] C.-C. Li, L. W. Engel, D. Shahar, D. C. Tsui, and M. Shayegan. Microwave conductivity resonance of two-dimensional hole system. *Phys. Rev. Lett.*, 79:1353, 1997.

[75] P. D. Ye, L. W. Engel, D. C. Tsui, R. M. Lewis, L. N. Pfeiffer, and K. West. Correlation lengths of the wigner-crystal order in a two-dimensional electron system at high magnetic fields. *Phys. Rev. Lett.*, 89:176802, Oct 2002.

[76] Yong Chen, R. M. Lewis, L. W. Engel, D. C. Tsui, P. D. Ye, L. N. Pfeiffer, and K. W. West. Microwave resonance of the 2d wigner crystal around integer landau fillings. *Phys. Rev. Lett.*, 91:016801, Jul 2003.

[77] Yong P. Chen, G. Sambandamurthy, Z. H. Wang, R. M. Lewis, L. W. Engel, D. C. Tsui, P. D. Ye, L. N. Pfeiffer, and K. W. West. Melting of a 2d quantum electron solid in high magnetic field. *Nat. Phys.*, 2:452, 2006.

[78] L. Tiemann, T. D. Rhone, N. Shibata, and K. Muraki. Nmr profiling of quantum electron solids in high magnetic fields. *Nat. Phys.*, 10:648–652, 2014.

[79] H. Deng, Y. Liu, I. Jo, L. N. Pfeiffer, K. W. West, K. W. Baldwin, and M. Shayegan. Commensurability oscillations of composite fermions induced by the periodic potential of a wigner crystal. *Phys. Rev. Lett.*, 117:096601, Aug 2016.

[80] Matthew Yankowitz, Shaowen Chen, Hryhoriy Polshyn, Yuxuan Zhang, K Watanabe, T Taniguchi, David Graf, Andrea F Young, and Cory R Dean. Tuning superconductivity in twisted bilayer graphene. *Science*, 363(6431):1059–1064, mar 2019.

[81] Yang Xu, Song Liu, Daniel A Rhodes, Kenji Watanabe, Takashi Taniguchi, James Hone, Veit Elser, Kin Fai Mak, and Jie Shan. Abundance of correlated insulating states at fractional fillings of WSe_2/WS_2 moiré superlattices. jul 2020.

[82] Xiaodong Xu, Wang Yao, Di Xiao, and Tony F Heinz. Spin and pseudospins in layered transition metal dichalcogenides. *Nature Physics*, 10(5):343–350, 2014.

[83] Gang Wang, Alexey Chernikov, Mikhail M. Glazov, Tony F. Heinz, Xavier Marie, Thierry Amand, and Bernhard Urbaszek. Colloquium : Excitons in atomically thin transition metal dichalcogenides. *Reviews of Modern Physics*, 90(2):021001, apr 2018.

[84] Hongyi Yu, Gui-Bin Liu, Pu Gong, Xiaodong Xu, and Wang Yao. *Nat. Commun.*, 5(1):3876, May 2014.

[85] M. M. Glazov, T. Amand, X. Marie, D. Lagarde, L. Bouet, and B. Urbaszek. Exciton fine structure and spin decoherence in monolayers of transition metal dichalcogenides. *Phys. Rev. B*, 89:201302, 2014.

[86] Diana Y. Qiu, Ting Cao, and Steven G. Louie. Nonanalyticity, valley quantum phases, and lightlike exciton dispersion in monolayer transition metal dichalcogenides: Theory and first-principles calculations. *Phys. Rev. Lett.*, 115:176801, Oct 2015.

[87] Stefano Larentis, Hema C. P. Movva, Babak Fallahazad, Kyounghwan Kim, Armand Behroozi, Takashi Taniguchi, Kenji Watanabe, Sanjay K. Banerjee, and Emanuel Tutuc. Large effective mass and interaction-enhanced Zeeman splitting of K - valley electrons in MoSe2. *Phys. Rev. B*, 97(20):201407, may 2018.

[88] Yi Zhang, Tay-Rong Chang, Bo Zhou, Yong-tao Cui, Hao Yan, Zhongkai Liu, Felix Schmitt, James Lee, Rob Moore, Yulin Chen, Hsin Lin, Horng-Tay Jeng, Sung-Kwan Mo, Zahid Hussain, Arun Bansil, and Zhi-Xun Shen. Direct observation of the transition from indirect to direct bandgap in atomically thin epitaxial MoSe2. *Nat. Nanotech.*, 9(2):111–115, 2014.

[89] M Goryca, J Li, A V Stier, T Taniguchi, K Watanabe, E Courtade, S Shree, C Robert, B Urbaszek, X Marie, and S A Crooker. Revealing exciton masses and dielectric properties of monolayer semiconductors with high magnetic fields. *Nature Communications*, 10(1):4172, 2019.

[90] Yilei Li, Jonathan Ludwig, Tony Low, Alexey Chernikov, Xu Cui, Ghidewon Arefe, Young Duck Kim, Arend M. van der Zande, Albert Rigosi, Heather M. Hill, Suk Hyun Kim, James Hone, Zhiqiang Li, Dmitry Smirnov, and Tony F. Heinz. Valley Splitting and Polarization by the Zeeman Effect in Monolayer MoSe$_2$. *Physical Review Letters*, 113(26):266804, dec 2014.

[91] Ajit Srivastava, Meinrad Sidler, Adrien V. Allain, Dominik S. Lembke, Andras Kis, and Atac Imamoglu. Valley Zeeman effect in elementary optical excitations of monolayer WSe$_2$. *Nature Physics*, 11(2):141–147, jan 2015.

[92] G Aivazian, Zhirui Gong, Aaron M Jones, Rui-Lin L Chu, J Yan, D G Mandrus, Chuanwei Zhang, David Cobden, Wang Yao, and X. D Xu. Magnetic control of valley pseudospin in monolayer WSe_2. *Nature Physics*, 11(2):148–152, jan 2015.

[93] David MacNeill, Colin Heikes, Kin Fai Mak, Zachary Anderson, Andor Kormányos, Viktor Zólyomi, Jiwoong Park, and Daniel C. Ralph. Breaking of Valley Degeneracy by Magnetic Field in Monolayer $MoSe_2$. *Physical Review Letters*, 114(3):037401, jan 2015.

[94] Kyle L Seyler, Pasqual Rivera, Hongyi Yu, Nathan P Wilson, Essance L Ray, David G Mandrus, Jiaqiang Yan, Wang Yao, and Xiaodong Xu. Signatures of moiré-trapped valley excitons in $MoSe_2$/WSe_2 heterobilayers. *Nature*, 567(7746):66–70, mar 2019.

[95] Kha Tran, Galan Moody, Fengcheng Wu, Xiaobo Lu, Junho Choi, Kyounghwan Kim, Amritesh Rai, Daniel A Sanchez, Jiamin Quan, Akshay Singh, Jacob Embley, André Zepeda, Marshall Campbell, Travis Autry, Takashi Taniguchi, Kenji Watanabe, Nanshu Lu, Sanjay K Banerjee, Kevin L Silverman, Suenne Kim, Emanuel Tutuc, Li Yang, Allan H MacDonald, and Xiaoqin Li. Evidence for moiré excitons in van der Waals heterostructures. *Nature*, 567(7746):71–75, mar 2019.

[96] Chenhao Jin, Emma C Regan, Aiming Yan, M. Iqbal Bakti Utama, Danqing Wang, Sihan Zhao, Ying Qin, Sijie Yang, Zhiren Zheng, Shenyang Shi, Kenji Watanabe, Takashi Taniguchi, Sefaattin Tongay, Alex Zettl, and Feng Wang. Observation of moiré excitons in WSe_2/WS_2 heterostructure superlattices. *Nature*, 567(7746):76–80, mar 2019.

[97] Evgeny M Alexeev, David A Ruiz-Tijerina, Mark Danovich, Matthew J Hamer, Daniel J Terry, Pramoda K Nayak, Seongjoon Ahn, Sangyeon Pak, Juwon Lee, Jung Inn Sohn, Maciej R Molas, Maciej Koperski, Kenji Watanabe, Takashi Taniguchi, Kostya S Novoselov, Roman V Gorbachev, Hyeon Suk Shin, Vladimir I Fal'ko, and Alexander I Tartakovskii. Resonantly hybridized excitons in moiré superlattices in van der Waals heterostructures. *Nature*, 567(7746):81–86, mar 2019.

[98] Trond I. Andersen, Giovanni Scuri, Andrey Sushko, Kristiaan De Greve, Jiho Sung, You Zhou, Dominik S. Wild, Ryan J. Gelly, Hoseok Heo, Kenji Watanabe, Takashi Taniguchi, Philip Kim, Hongkun Park, and Mikhail D. Lukin. Moiré Excitons

Correlated with Superlattice Structure in Twisted WSe_2/WSe_2 Homobilayers. *arXiv:1912.06955*, dec 2019.

[99] Hongyi Yu, Gui-Bin Liu, Jianju Tang, Xiaodong Xu, and Wang Yao. Moiré excitons: From programmable quantum emitter arrays to spin-orbit–coupled artificial lattices. *Science Advances*, 3(11):e1701696, nov 2017.

[100] Fengcheng Wu, Timothy Lovorn, and A H MacDonald. Theory of optical absorption by interlayer excitons in transition metal dichalcogenide heterobilayers. *Physical Review B*, 97(3):035306, jan 2018.

[101] David A Ruiz-Tijerina and Vladimir I Fal'ko. Interlayer hybridization and moiré superlattice minibands for electrons and excitons in heterobilayers of transition-metal dichalcogenides. *Physical Review B*, 99(12):125424, mar 2019.

[102] Daijiro Yoshioka and Hidetoshi Fukuyama. Charge Density Wave State of Two-Dimensional Electrons in Strong Magnetic Fields. *Journal of the Physical Society of Japan*, 47(2):394–402, aug 1979.

[103] Keliang He, Charles Poole, Kin Fai Mak, and Jie Shan. Experimental Demonstration of Continuous Electronic Structure Tuning via Strain in Atomically Thin MoS_2. *Nano Letters*, 13(6):2931–2936, jun 2013.

[104] Hiram J. Conley, Bin Wang, Jed I. Ziegler, Richard F. Haglund, Sokrates T. Pantelides, and Kirill I. Bolotin. Bandgap Engineering of Strained Monolayer and Bilayer MoS_2. *Nano Letters*, 13(8):3626–3630, aug 2013.

[105] C. R. Zhu, G. Wang, B. L. Liu, X. Marie, X. F. Qiao, X. Zhang, X. X. Wu, H. Fan, P. H. Tan, T. Amand, and B. Urbaszek. Strain tuning of optical emission energy and polarization in monolayer and bilayer MoS_2. *Physical Review B*, 88(12):121301(R), sep 2013.

[106] Dmitry K. Efimkin and Allan H. MacDonald. Many-body theory of trion absorption features in two-dimensional semiconductors. *Phys. Rev. B*, 95:035417, Jan 2017.

[107] Yuya Shimazaki, Clemens Kuhlenkamp, Ido Schwartz, Tomasz Smoleński, Kenji Watanabe, Takashi Taniguchi, Martin Kroner, Richard Schmidt, Michael Knap, and

Ataç Imamoğlu. Optical signatures of periodic charge distribution in a mott-like correlated insulator state. *Phys. Rev. X*, 11:021027, May 2021.

[108] N. R. Cooper. Theory of exciton recombination from the magnetically induced Wigner crystal. *Physical Review B*, 53(16):10804–10812, apr 1996.

[109] Jongsoo Yoon, C. C. Li, D. Shahar, D. C. Tsui, and M. Shayegan. Wigner crystallization and metal-insulator transition of two-dimensional holes in gaas at $B = 0$. *Phys. Rev. Lett.*, 82:1744–1747, Feb 1999.

[110] I. Shapir, A. Hamo, S. Pecker, C. P. Moca, Ö. Legeza, G. Zarand, and S. Ilani. Imaging the electronic wigner crystal in one dimension. *Science*, 364(6443):870–875, 2019.

[111] M. S. Hossain, M. K. Ma, K. A. Villegas Rosales, Y. J. Chung, L. N. Pfeiffer, K. W. West, K. W. Baldwin, and M. Shayegan. Observation of spontaneous ferromagnetism in a two-dimensional electron system. *Proc. Natl. Acad. Sci.*, 2020.

[112] M. Zarenia, D. Neilson, B. Partoens, and F. M. Peeters. Wigner crystallization in transition metal dichalcogenides: A new approach to correlation energy. *Phys. Rev. B*, 95:115438, Mar 2017.

[113] Tomasz Smoleński, Pavel E. Dolgirev, Clemens Kuhlenkamp, Alexander Popert, Yuya Shimazaki, Patrick Back, Xiaobo Lu, Martin Kroner, Kenji Watanabe, Takashi Taniguchi, and et al. Signatures of wigner crystal of electrons in a monolayer semiconductor. *Nature*, 595(7865):53–57, Jun 2021.

[114] You Zhou, Jiho Sung, Elise Brutschea, Ilya Esterlis, Yao Wang, Giovanni Scuri, Ryan J. Gelly, Hoseok Heo, Takashi Taniguchi, Kenji Watanabe, Gergely Zaránd, Mikhail D. Lukin, Philip Kim, Eugene Demler, and Hongkun Park. Bilayer wigner crystals in a transition metal dichalcogenide heterostructure. *Nature*, 595(7865):48–52, 2021.

[115] Walter Kohn. Cyclotron resonance and de haas-van alphen oscillations of an interacting electron gas. *Phys. Rev.*, 123:1242–1244, Aug 1961.

[116] C. Kallin and B. I. Halperin. Excitations from a filled landau level in the two-dimensional electron gas. *Phys. Rev. B*, 30:5655–5668, Nov 1984.

[117] L. Landau. Theory of the superfluidity of helium ii. *Phys. Rev.*, 60:356–358, Aug 1941.

[118] S. M. Girvin, A. H. MacDonald, and P. M. Platzman. Magneto-roton theory of collective excitations in the fractional quantum hall effect. *Phys. Rev. B*, 33:2481–2494, Feb 1986.

[119] Steven Weinberg. *The Quantum Theory of Fields*, volume 1. Cambridge University Press, 1995.

[120] M. M. Fogler. Stripe and bubble phases in quantum hall systems. In *High Magnetic Fields*, volume 595, pages 98–138. Springer, Berlin, Heidelberg, 2002.

[121] A. A. Koulakov, M. M. Fogler, and B. I. Shklovskii. Charge density wave in two-dimensional electron liquid in weak magnetic field. *Phys. Rev. Lett.*, 76(3):499, 1996.

[122] Jiho Sung, Jue Wang, Ilya Esterlis, Pavel A. Volkov, Giovanni Scuri, You Zhou, Elise Brutschea, Takashi Taniguchi, Kenji Watanabe, Yubo Yang, Miguel A. Morales, Shiwei Zhang, Andrew J. Millis, Mikhail D. Lukin, Philip Kim, Eugene Demler, and Hongkun Park. Observation of an electronic microemulsion phase emerging from a quantum crystal-to-liquid transition, 2023.

[123] B. Bernu, L. Cândido, and D. M. Ceperley. Exchange frequencies in the 2d wigner crystal. *Phys. Rev. Lett.*, 86(5):870, 2001.

[124] Alex Gómez Salvador, Clemens Kuhlenkamp, Livio Ciorciaro, Michael Knap, and Ataç Imamoğlu. Optical signatures of periodic magnetization: The moiré zeeman effect. *Phys. Rev. Lett.*, 128:237401, Jun 2022.

[125] W. Zwerger. Strongly interacting fermi gases. *Proceedings of the International School of Physics "Enrico Fermi" - Course 191 "Quantum Matter at Ultralow Temperatures" edited by M. Inguscio, W. Ketterle, S. Stringari and G. Roati (IOS Press, Amsterdam; SIF Bologna)*, pages 64–152, 2016.

[126] Herman Feshbach. A unified theory of nuclear reactions. ii. *Annals of Physics*, 19(2):287–313, 1962.

[127] Cheng Chin, Rudolf Grimm, Paul Julienne, and Eite Tiesinga. Feshbach resonances in ultracold gases. *Rev. Mod. Phys.*, 82:1225–1286, Apr 2010.

[128] Wolfgang Ketterle and Martin W. Zwierlein. Making, probing and understanding ultracold fermi gases. *Nuovo Cimento Rivista Serie*, 31(5):247–422, 2008.

[129] R.A. Duine and H.T.C. Stoof. Atom–molecule coherence in bose gases. *Physics Reports*, 396(3):115–195, 2004.

[130] I. Ferrier-Barbut, M. Delehaye, S. Laurent, A. T. Grier, M. Pierce, B. S. Rem, F. Chevy, and C. Salomon. A mixture of bose and fermi superfluids. *Science*, 345(6200):1035–1038, 2014.

[131] B. J. DeSalvo, Krutik Patel, Geyue Cai, and Cheng Chin. Observation of fermion-mediated interactions between bosonic atoms. *Nature*, 568(7750):61–64, 2019.

[132] Isabella Fritsche, Cosetta Baroni, Erich Dobler, Emil Kirilov, Bo Huang, Rudolf Grimm, Georg M Bruun, and Pietro Massignan. Stability and breakdown of fermi polarons in a strongly interacting fermi-bose mixture. *arXiv preprint arXiv:2103.03625*, 2021.

[133] Robert Jördens, Niels Strohmaier, Kenneth Günter, Henning Moritz, and Tilman Esslinger. A mott insulator of fermionic atoms in an optical lattice. *Nature*, 455(7210):204–207, 2008.

[134] Michael Schreiber, Sean S. Hodgman, Pranjal Bordia, Henrik P. Lüschen, Mark H. Fischer, Ronen Vosk, Ehud Altman, Ulrich Schneider, and Immanuel Bloch. Observation of many-body localization of interacting fermions in a quasirandom optical lattice. *Science*, 349(6250):842–845, 2015.

[135] Eva Y. Andrei, Dmitri K. Efetov, Pablo Jarillo-Herrero, Allan H. MacDonald, Kin Fai Mak, T. Senthil, Emanuel Tutuc, Ali Yazdani, and Andrea F. Young. The marvels of moiré materials. *Nature Reviews Materials*, 6(3):201–206, 2021.

[136] Xiaomeng Liu, J. I. A. Li, Kenji Watanabe, Takashi Taniguchi, James Hone, Bertrand I. Halperin, Philip Kim, and Cory R. Dean. Crossover between strongly-coupled and weakly-coupled exciton superfluids, 2020.

[137] Rafi Bistritzer and Allan H. MacDonald. Moiré bands in twisted double-layer graphene. *Proceedings of the National Academy of Sciences*, 108(30):12233–12237, 2011.

[138] Gang Wang, Alexey Chernikov, Mikhail M. Glazov, Tony F. Heinz, Xavier Marie, Thierry Amand, and Bernhard Urbaszek. Colloquium: Excitons in atomically thin transition metal dichalcogenides. *Rev. Mod. Phys.*, 90:021001, Apr 2018.

[139] E. V. Calman, L. H. Fowler-Gerace, D. J. Choksy, L. V. Butov, D. E. Nikonov, I. A. Young, S. Hu, A. Mishchenko, and A. K. Geim. Indirect Excitons and Trions in MoSe2/WSe2 van der Waals Heterostructures. *Nano Letters*, 20(3):1869–1875, 03 2020.

[140] J. J. Sakurai and Jim Napolitano. *Modern Quantum Mechanics*. Cambridge University Press, 2 edition, 2017.

[141] Sadhan K. Adhikari. Quantum scattering in two dimensions. *American Journal of Physics*, 54(4):362–367, 1986.

[142] Meera M. Parish and Jesper Levinsen. Highly polarized fermi gases in two dimensions. *Physical Review A*, 87(3):033616, mar 2013.

[143] K. Kanjilal and D. Blume. Coupled-channel pseudopotential description of the feshbach resonance in two dimensions. *Phys. Rev. A*, 73:060701, Jun 2006.

[144] H. H. Fang, B. Han, C. Robert, M. A. Semina, D. Lagarde, E. Courtade, T. Taniguchi, K. Watanabe, T. Amand, B. Urbaszek, M. M. Glazov, and X. Marie. Control of the exciton radiative lifetime in van der waals heterostructures. *Phys. Rev. Lett.*, 123:067401, Aug 2019.

[145] Jason S. Ross, Sanfeng Wu, Hongyi Yu, Nirmal J. Ghimire, Aaron M. Jones, Grant Aivazian, Jiaqiang Yan, David G. Mandrus, Di Xiao, Wang Yao, and Xiaodong Xu. Electrical control of neutral and charged excitons in a monolayer semiconductor. *Nature Communications*, 4(1):1474, 2013.

[146] R. A. Suris. Correlation between trion and hole in fermi distribution in process of trion photo-excitation in doped qws. In Wolfgang J. Ossau and Robert Suris,

editors, *Optical Properties of 2D Systems with Interacting Electrons*, pages 111–124, Dordrecht, 2003. Springer Netherlands.

[147] M. M. Glazov. Optical properties of charged excitons in two-dimensional semiconductors. *The Journal of Chemical Physics*, 153(3):034703, 2020.

[148] F.G. Fumi. Cxvi. vacancies in monovalent metals. *The London, Edinburgh, and Dublin Philosophical Magazine and Journal of Science*, 46(380):1007–1020, 1955.

[149] Richard Schmidt, Michael Knap, Dmitri A. Ivanov, Jhih-Shih You, Marko Cetina, and Eugene Demler. Universal many-body response of heavy impurities coupled to a fermi sea: a review of recent progress. *Rep. Prog. Phys.*, 81:024401, January 2018.

[150] R. Combescot, A. Recati, C. Lobo, and F. Chevy. Normal state of highly polarized fermi gases: Simple many-body approaches. *Phys. Rev. Lett.*, 98:180402, May 2007.

[151] Richard Schmidt, Tilman Enss, Ville Pietilä, and Eugene Demler. Fermi polarons in two dimensions. *Phys. Rev. A*, 85:021602, Feb 2012.

[152] Jonas Vlietinck, Jan Ryckebusch, and Kris Van Houcke. Diagrammatic monte carlo study of the fermi polaron in two dimensions. *Phys. Rev. B*, 89:085119, Feb 2014.

[153] Peter Kroiss and Lode Pollet. Diagrammatic monte carlo study of quasi-two-dimensional fermi polarons. *Phys. Rev. B*, 90:104510, Sep 2014.

[154] Marko Cetina, Michael Jag, Rianne S. Lous, Isabella Fritsche, Jook T. M. Walraven, Rudolf Grimm, Jesper Levinsen, Meera M. Parish, Richard Schmidt, Michael Knap, and Eugene Demler. Ultrafast many-body interferometry of impurities coupled to a fermi sea. *Science*, 354(6308):96–99, 2016.

[155] Meera M. Parish. Polaron-molecule transitions in a two-dimensional fermi gas. *Physical Review A*, 83(5):051603, may 2011.

[156] Sascha Zöllner, G. M. Bruun, and C. J. Pethick. Polarons and molecules in a two-dimensional fermi gas. *Physical Review A*, 83(2):021603, feb 2011.

[157] Mehrtash Babadi. *Non-equilibrium dynamics of artificial quantum matter*. Harvard University, 2013.

[158] L M Sieberer, M Buchhold, and S Diehl. Keldysh field theory for driven open quantum systems. *Reports on Progress in Physics*, 79(9):096001, Aug 2016.

[159] Tomasz Wasak, Richard Schmidt, and Francesco Piazza. Quantum-zeno fermi polaron in the strong dissipation limit. *Phys. Rev. Research*, 3:013086, Jan 2021.

[160] C. Kohstall, M. Zaccanti, M. Jag, A. Trenkwalder, P. Massignan, G. M. Bruun, F. Schreck, and R. Grimm. Metastability and coherence of repulsive polarons in a strongly interacting fermi mixture. *Nature*, 485(7400):615–618, 2012.

[161] P. Massignan. Polarons and dressed molecules near narrow feshbach resonances. *EPL (Europhysics Letters)*, 98(1):10012, apr 2012.

[162] N. Takemura, S. Trebaol, M. Wouters, M. T. Portella-Oberli, and B. Deveaud. Polaritonic feshbach resonance. *Nature Physics*, 10(7):500–504, 2014.

[163] Fabrice P. Laussy, Alexey V. Kavokin, and Ivan A. Shelykh. Exciton-polariton mediated superconductivity. *Phys. Rev. Lett.*, 104:106402, Mar 2010.

[164] Ovidiu Cotleţ, Sina Zeytinoğlu, Manfred Sigrist, Eugene Demler, and Ataç Imamoğlu. Superconductivity and other collective phenomena in a hybrid bose-fermi mixture formed by a polariton condensate and an electron system in two dimensions. *Phys. Rev. B*, 93:054510, Feb 2016.

[165] Zefang Wang, Daniel A. Rhodes, Kenji Watanabe, Takashi Taniguchi, James C. Hone, Jie Shan, and Kin Fai Mak. Evidence of high-temperature exciton condensation in two-dimensional atomic double layers. *Nature*, 574(7776):76–80, 2019.

[166] Long Zhang, Zhe Zhang, Fengcheng Wu, Danqing Wang, Rahul Gogna, Shaocong Hou, Kenji Watanabe, Takashi Taniguchi, Krishnamurthy Kulkarni, Thomas Kuo, Stephen R. Forrest, and Hui Deng. Twist-angle dependence of moiré excitons in WS2/MoSe2 heterobilayers. *Nature Communications*, 11(1):5888, 2020.

[167] V. Efimov. Energy levels arising from resonant two-body forces in a three-body system. *Physics Letters B*, 33(8):563–564, 1970.

[168] V N Efimov. Weakly bound states of three resonantly interacting particles. *Yadern. Fiz. 12: 1080-91(Nov 1970).*, 1 1970.

[169] Kevin Slagle and Liang Fu. Charge transfer excitations, pair density waves, and super-conductivity in moiré materials. *Phys. Rev. B*, 102:235423, Dec 2020.

[170] C. Castelnovo, R. Moessner, and S. L. Sondhi. Magnetic monopoles in spin ice. *Nature*, 451(7174):42–45, 2008.

[171] Xiao-Gang Wen. *Quantum Field Theory of Many-Body Systems: From the Origin of Sound to an Origin of Light and Electrons*. Oxford Graduate Texts. Oxford University Press, Oxford, 2007.

[172] P.W. Anderson. Resonating valence bonds: A new kind of insulator? *Materials Research Bulletin*, 8(2):153–160, 1973.

[173] X. G. Wen, Frank Wilczek, and A. Zee. Chiral spin states and superconductivity. *Phys. Rev. B*, 39:11413–11423, Jun 1989.

[174] Jeffrey G. Rau, Eric Kin-Ho Lee, and Hae-Young Kee. Spin-orbit physics giving rise to novel phases in correlated systems: Iridates and related materials. *Annual Review of Condensed Matter Physics*, 7(1):195–221, 2016.

[175] Douglas R. Hofstadter. Energy levels and wave functions of bloch electrons in rational and irrational magnetic fields. *Phys. Rev. B*, 14:2239–2249, Sep 1976.

[176] V. Kalmeyer and R. B. Laughlin. Equivalence of the resonating-valence-bond and fractional quantum hall states. *Phys. Rev. Lett.*, 59:2095–2098, Nov 1987.

[177] Olexei I. Motrunich. Orbital magnetic field effects in spin liquid with spinon fermi sea: Possible application to $\kappa-(\text{ET})_2\text{cu}_2(\text{CN})_3$. *Phys. Rev. B*, 73:155115, Apr 2006.

[178] Shou-Shu Gong, W. Zhu, J.-X. Zhu, D. N. Sheng, and Kun Yang. Global phase diagram and quantum spin liquids in a spin-$\frac{1}{2}$ triangular antiferromagnet. *Phys. Rev. B*, 96:075116, Aug 2017.

[179] J. P. Eisenstein, G. S. Boebinger, L. N. Pfeiffer, K. W. West, and Song He. New fractional quantum hall state in double-layer two-dimensional electron systems. *Phys. Rev. Lett.*, 68:1383–1386, Mar 1992.

[180] Xiaomeng Liu, Kenji Watanabe, Takashi Taniguchi, Bertrand I. Halperin, and Philip Kim. Quantum hall drag of exciton condensate in graphene. *Nature Physics*, 13(8):746–750, 2017.

[181] L. A. Ponomarenko, R. V. Gorbachev, G. L. Yu, D. C. Elias, R. Jalil, A. A. Patel, A. Mishchenko, A. S. Mayorov, C. R. Woods, J. R. Wallbank, M. Mucha-Kruczynski, B. A. Piot, M. Potemski, I. V. Grigorieva, K. S. Novoselov, F. Guinea, V. I. Fal'ko, and A. K. Geim. Cloning of dirac fermions in graphene superlattices. *Nature*, 497(7451):594–597, 2013.

[182] Pei Zhao, Chengxin Xiao, and Wang Yao. Universal superlattice potential for 2d materials from twisted interface inside h-bn substrate. *npj 2D Materials and Applications*, 5(1):38, 2021.

[183] Yang Xu, Kaifei Kang, Kenji Watanabe, Takashi Taniguchi, Kin Fai Mak, and Jie Shan. Tunable bilayer hubbard model physics in twisted wse2. *arXiv preprint arXiv:2202.02055*, 2022.

[184] C. R. Woods, P. Ares, H. Nevison-Andrews, M. J. Holwill, R. Fabregas, F. Guinea, A. K. Geim, K. S. Novoselov, N. R. Walet, and L. Fumagalli. Charge-polarized interfacial superlattices in marginally twisted hexagonal boron nitride. *Nature Communications*, 12(1):347, 2021.

[185] Robin Huber, Max-Niklas Steffen, Martin Drienovsky, Andreas Sandner, Kenji Watanabe, Takashi Taniguchi, Daniela Pfannkuche, Dieter Weiss, and Jonathan Eroms. Band conductivity oscillations in a gate-tunable graphene superlattice. *Nature Communications*, 13(1):2856, 2022.

[186] Nai Chao Hu and Allan H. MacDonald. Competing magnetic states in transition metal dichalcogenide moiré materials. *Phys. Rev. B*, 104:214403, Dec 2021.

[187] X. G. WEN. Topological orders in rigid states. *International Journal of Modern Physics B*, 04(02):239–271, 1990.

[188] Michael Levin and Xiao-Gang Wen. Detecting topological order in a ground state wave function. *Phys. Rev. Lett.*, 96:110405, Mar 2006.

[189] Hongyuan Li, Shaowei Li, Emma C. Regan, Danqing Wang, Wenyu Zhao, Salman Kahn, Kentaro Yumigeta, Mark Blei, Takashi Taniguchi, Kenji Watanabe, Sefaattin Tongay, Alex Zettl, Michael F. Crommie, and Feng Wang. Imaging two-dimensional generalized wigner crystals. *Nature*, 597(7878):650–654, 2021.

[190] Seiji Miyashita. A variational study of the ground state of frustrated quantum spin models. *Journal of the Physical Society of Japan*, 53(1):44–47, 1984.

[191] David A. Huse and Veit Elser. Simple variational wave functions for two-dimensional heisenberg spin-½ antiferromagnets. *Phys. Rev. Lett.*, 60:2531–2534, Jun 1988.

[192] Michael P. Zaletel, Roger S. K. Mong, Frank Pollmann, and Edward H. Rezayi. Infinite density matrix renormalization group for multicomponent quantum hall systems. *Phys. Rev. B*, 91:045115, Jan 2015.

[193] Adolfo G. Grushin, Johannes Motruk, Michael P. Zaletel, and Frank Pollmann. Characterization and stability of a fermionic $\nu = 1/3$ fractional chern insulator. *Phys. Rev. B*, 91:035136, Jan 2015.

[194] Prashant Kumar and F. D. M. Haldane. Neutral excitations of quantum hall states: A density matrix renormalization group study. *Phys. Rev. B*, 106:075116, Aug 2022.

[195] Johannes Hauschild and Frank Pollmann. Efficient numerical simulations with Tensor Networks: Tensor Network Python (TeNPy). *SciPost Phys. Lect. Notes*, page 5, 2018. Code available from https://github.com/tenpy/tenpy.

[196] Johannes Motruk, Michael P. Zaletel, Roger S. K. Mong, and Frank Pollmann. Density matrix renormalization group on a cylinder in mixed real and momentum space. *Physical Review B*, 93(15):155139, 2016.

[197] G. Ehlers, S. R. White, and R. M. Noack. Hybrid-space density matrix renormalization group study of the doped two-dimensional Hubbard model. *Physical Review B*, 95(12):125125, 2017.

[198] X. G. Wen. Gapless boundary excitations in the quantum Hall states and in the chiral spin states. *Phys. Rev. B*, 43:11025–11036, May 1991.

[199] J. E. Moore and F. D. M. Haldane. Edge excitations of the $\nu=$ spin-singlet quantum Hall state. *Phys. Rev. B*, 55:7818–7823, Mar 1997.

[200] R. B. Laughlin. Quantized hall conductivity in two dimensions. *Phys. Rev. B*, 23:5632–5633, May 1981.

[201] Michael P. Zaletel, Roger S. K. Mong, and Frank Pollmann. Topological characterization of fractional quantum hall ground states from microscopic hamiltonians. *Phys. Rev. Lett.*, 110:236801, Jun 2013.

[202] J.P. Eisenstein. Exciton condensation in bilayer quantum hall systems. *Annual Review of Condensed Matter Physics*, 5(1):159–181, 2014.

[203] K. A. Villegas Rosales, S. K. Singh, Meng K. Ma, Md. Shafayat Hossain, Y. J. Chung, L. N. Pfeiffer, K. W. West, K. W. Baldwin, and M. Shayegan. Competition between fractional quantum hall liquid and wigner solid at small fillings: Role of layer thickness and landau level mixing. *Phys. Rev. Research*, 3:013181, Feb 2021.

[204] X. G. Wen. Chiral luttinger liquid and the edge excitations in the fractional quantum hall states. *Phys. Rev. B*, 41:12838–12844, Jun 1990.

[205] T. Smoleński, O. Cotlet, A. Popert, P. Back, Y. Shimazaki, P. Knüppel, N. Dietler, T. Taniguchi, K. Watanabe, M. Kroner, and A. Imamoglu. Interaction-induced shubnikov–de haas oscillations in optical conductivity of monolayer mose$_2$. *Phys. Rev. Lett.*, 123:097403, Aug 2019.

[206] Hyang-Tag Lim, Emre Togan, Martin Kroner, Javier Miguel-Sanchez, and Ataç Imamoğlu. Electrically tunable artificial gauge potential for polaritons. *Nature Communications*, 8(1):14540, 2017.

[207] Dawei Zhai, Cong Chen, Cong Xiao, and Wang Yao. Layer-contrasted hall effect in twisted bilayers with time reversal symmetry, 2022.

[208] Alon Inbar, John Birkbeck, Jiewen Xiao, Takashi Taniguchi, Kenji Watanabe, Binghai Yan, Yuval Oreg, Ady Stern, Erez Berg, and Shahal Ilani. The quantum twisting microscope, 2022.

[209] Wilhelm Kadow, Laurens Vanderstraeten, and Michael Knap. Hole spectral function of a chiral spin liquid in the triangular lattice hubbard model. *Phys. Rev. B*, 106:094417, Sep 2022.

[210] Alex Gómez Salvador, Ataç Imamoğlu, and Eugene Demler. Private Communication, 2022.

[211] Ashvin Vishwanath. Private Communication, 2023.

[212] A.M. Polyakov. Quark confinement and topology of gauge theories. *Nuclear Physics B*, 120(3):429–458, 1977.

[213] SHOU CHENG ZHANG. The chern–simons–landau–ginzburg theory of the fractional quantum hall effect. *International Journal of Modern Physics B*, 06(01):25–58, 1992.

[214] Valerio Peri, Shahal Ilani, Patrick A. Lee, and Gil Refael. Probing quantum spin liquids with a quantum twisting microscope, 2023.

[215] Clemens Kuhlenkamp, Michael Knap, Marcel Wagner, Richard Schmidt, and Ataç Imamoğlu. Tunable feshbach resonances and their spectral signatures in bilayer semiconductors. *Phys. Rev. Lett.*, 129:037401, Jul 2022.

[216] Nicola Marzari, Arash A. Mostofi, Jonathan R. Yates, Ivo Souza, and David Vanderbilt. Maximally localized wannier functions: Theory and applications. *Rev. Mod. Phys.*, 84:1419–1475, Oct 2012.

[217] Ya-Hui Zhang and T. Senthil. Bridging hubbard model physics and quantum hall physics in trilayer graphene/$h-$BN moiré superlattice. *Phys. Rev. B*, 99:205150, May 2019.

[218] Alexander Wietek and Andreas M. Läuchli. Chiral spin liquid and quantum criticality in extended $s=\frac{1}{2}$ heisenberg models on the triangular lattice. *Phys. Rev. B*, 95:035141, Jan 2017.

[219] Yuval Gannot, Yi-Fan Jiang, and Steven A. Kivelson. Hubbard ladders at small u revisited. *Phys. Rev. B*, 102:115136, Sep 2020.

[220] Caterina Zerba, Clemens Kuhlenkamp, Ataç Imamoğlu, and Michael Knap. Realizing topological superconductivity in tunable bose-fermi mixtures with transition metal dichalcogenide heterostructures, 2023.

[221] Hui Yang, Hanbit Oh, and Ya-Hui Zhang. Strong pairing from small fermi surface beyond weak coupling: Application to $la_3ni_2o_7$, 2023.

[222] Hannah Lange, Lukas Homeier, Eugene Demler, Ulrich Schollwöck, Fabian Grusdt, and Annabelle Bohrdt. Feshbach resonance in a strongly repulsive bilayer model: a possible scenario for bilayer nickelate superconductors, 2023.